NUMERICAL SIMULATION OF FLOATING OFFSHORE WIND TURBINE DYNAMIC RESPONSES WITH EXPERIMENTAL COMPARISON

A Dissertation

by

HYUNSEONG MIN

Submitted to the Office of Graduate and Professional Studies of
Texas A&M University
in partial fulfillment of the requirements for the degree of

DOCTOR OF PHILOSOPHY

Chair of Committee,	Jun Zhang
Co-Chair of Committee,	Hamn-Ching Chen
Committee Members,	Moo-Hyun Kim
	David Arthur Brooks
Head of Department,	Sharath Girimaji

May 2018

Major Subject: Ocean Engineering

ABSTRACT

Hywind, the world's first operational Floating Offshore Wind Turbine (FOWT), is constrained by a delta mooring system to improve the yaw station-keeping capacity. In this study, a mooring line-simulation code in COUPLE-FAST was extended to simulate the dynamics of a delta mooring system using a Finite Element Method. The old mooring-simulation code in COUPLE-FAST was replaced with the extended code, and the new program is named as COUPLE-D-FAST. In this program, FAST calculates the aerodynamic, control and electrical system, and structural dynamic forces. COUPLE-D computes mooring and hydrodynamic forces, and then it calculates the global motions of FOWT using the wind forces computed using FAST.

COUPLE-D-FAST was then employed for the simulation of Hywind constrained by a taut delta mooring system. The simulated global motions and mooring lines' tensions of Hywind were compared with the related measurements in a wave basin and the corresponding simulations obtained using a commercial code, FAST-OrcaFlex.

Several cases were simulated and compared with the measurements, which include free-decay tests, wind loads-only tests, wave loads-only tests, and wind combined with wave loads tests. Without empirical tunings on the yaw stiffness and damping of the Hywind's mooring system, the simulated yaw free-decay responses showed excellent agreement with those of the model test. In general, the simulated motions and mooring lines' tensions of Hywind showed satisfactory agreement with the experimental results in the cases of various wind and wave conditions. For the cases of wind combined with

irregular wave loads, however, the simulated pitch of the FOWT near its resonant frequency was significantly smaller than the related measurements. This may result from the scaling issue between the prototype and its model that the aerodynamic damping follows the Reynolds number while the scale in the model test was based on the Froude number.

In this dissertation, it was found that COUPLE-D-FAST can reliably and accurately simulate the delta mooring system of Hywind. The accurate predictions of the delta mooring dynamics may make important contribution to the future design of FOWT.

ACKNOWLEDGEMENTS

I would like to express my gratitude to Dr. Jun Zhang, my advisor and my committee chair, for his profound comments and suggestions throughout this research. I also would like to thank my committee co-chair, Dr. Hamn-Ching Chen, and my committee members, Dr. Moo-Hyun Kim and Dr. David Brooks, for their guidance and support throughout the course of this research.

I want to thank Dr. Cheng Peng for providing the source code of COUPLE-FAST and sharing his knowledge of the numerical challenges of coupling problems. Thanks also go to my friends and colleagues and the department faculty and staff for making my time at Texas A&M University a great experience.

Finally, special thanks to my mother, father and brother for their encouragement and unfailing support. I want to express my deepest love and thanks to my wife, Soonwoo Kim, for her patience, love, and taking care of our son. I am thankful to my son Henry for giving me happiness.

CONTRIBUTORS AND FUNDING SOURCES

Contributors

This work was supervised by a dissertation committee consisting of Professors Jun Zhang and Hamn-Ching Chen of the Department of Civil Engineering, Professor Moo-Hyun Kim of the Department of Ocean Engineering, and Professor David Arthur Brooks of the Department of Oceanography.

The model test data for Chapters 4 to 6 were provided by State Key Laboratory of Ocean Engineering in Shanghai Jiao Tong University.

All other work conducted for the dissertation was completed by the student independently.

Funding Sources

Graduate study was supported by scholarships from the Department of Ocean Engineering at Texas A&M University and Barrett and Margaret Hindes Foundation, and a dissertation fellowship from Office of Graduate and Professional Studies at Texas A&M University.

NOMENCLATURE

CG	Center of Gravity
DOE	U.S. Department of Energy
DOF	Degrees of Freedom
FEM	Finite Element Method
FFT	Fast Fourier Transform
FOWT	Floating Offshore Wind Turbines
HWM	Hybrid Wave Model
IFFT	Inverse Fast Fourier Transform
JONSWAP	Joint North Sea Wave Project
KC	Keulegan-Capenter
LC	Load Case
LF	Low Frequency
MARIN	Maritime Research Institute Netherland
NREL	National Renewable Energy Laboratory
OC3	Offshore Code Comparison Collaboration
TLP	Tension Leg Platform
WF	Wave Frequency

TABLE OF CONTENTS

Page

LIST OF FIGURES

Page

LIST OF TABLES

Page

1. INTRODUCTION

1.1. Background and Literature Review

For the last two decades, the world's level of renewable energy use has grown to meet our current and future energy needs. Among the various types of renewable energy, wind is one of the most widely available and cost-effective sources. In the past, most wind turbines were primarily constructed on land or in nearshore water. However, such turbines have shortcomings such as visual and noise impacts on residents, and intermittent electricity generation due to fluctuating wind speeds. Offshore wind turbines, especially those located in relatively deep water, can alleviate these problems. Especially since offshore wind tends to get stronger and steadier as the distance from land increases, such locations are likely to increase the production of electricity.

In 2008, the US Department of Energy (DOE) published a report stating that wind energy could provide as much as 20% of the US's electricity by 2030. This would have a positive effect on the environment by reducing air pollutants and carbon dioxide emissions. A shift to wind energy would also help to conserve water and reduce the demand for fossil fuels. As shown in Figure 1, offshore wind technology could gradually increase to generate as much as 18% (54GW) of the total wind power capacity by 2030 (U.S.DOE, 2008).

In the United States, wind power capacity increased by 8.2GW in 2016. Wind capacity increased to the total constructed wind capacity of 82.1GW. In the same year, global wind additions were estimated at 54.6GW, for a cumulative total of 486.7GW. The

US's wind energy market took second place behind China, based on the cumulative capacity. The first offshore wind farm in the United States was commissioned in Rhode Island in December of 2016. The projected capacity is 30 MW, and it is expected to supply electricity to 17,000 Rhode Island households (U.S.DOE, 2017a, b).

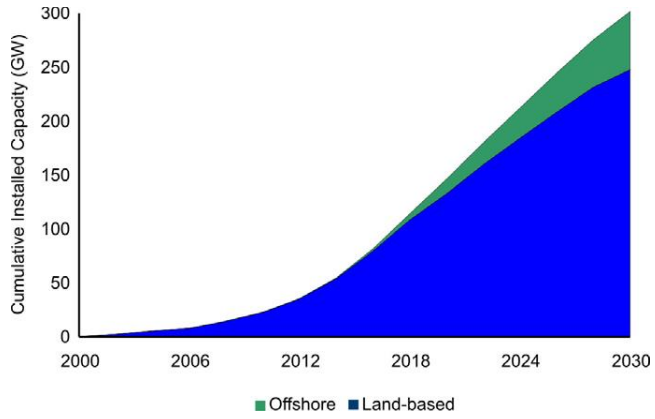

Figure 1 Cumulative Installed Wind Power Capacity Required to Produce 20% of Projected Electricity by 2030; Reprinted from U.S.DOE (2008)

Designing and constructing offshore wind farms is quite difficult compared to on-land production. Construction costs are high because offshore structures must endure harsh conditions such as hurricanes and typhoon. In addition, offshore wind turbines demand relatively high maintenance costs compared to those on land. Despite these disadvantages, offshore wind sources generate more energy because the offshore winds quality is better than those on land. According to the National Renewable Energy Laboratory (NREL), US offshore wind sources could generate as much as four times the nation's electric capacity (Musial and Ram, 2010).

Currently, several countries have plans to construct or been constructing floating wind farms. Floating Offshore Wind Turbines (FOWT) have already been built in many locations. The world's first operational FOWT was called Hywind; it was constructed by Statoil of Norway. The floating platform is a spar-buoy type with 100 m draft and installed in 200 m water depth. The diameter of the platform is 8.3 m at the main section and 6 m at the water's surface. The platform is connected to the seabed through a three-point mooring system. The wind turbine has a capacity of 2.3 MW and produced 32.5 GWh since 2010. Recently, Statoil constructed the world's first wind farm, named Hywind Scotland Pilot Park located in Scotland. The wind turbines were installed at a water depth of 95 to 129 m. They have a capacity of 30 MW in total, which could provide around 22,000 homes with electricity beginning in late 2017.

The second FOWT built was called WindFloat. The FOWT is a semi-submersible designed by Principle Power, and it was constructed in the offshore of Portugal in 2011. This structure's design was intended to improve motion performance by including heaving plates at each column. Thus, the structure is able to set aside stability by establishing a sufficiently low pitch motion. Chain and polyester mooring lines are deployed in the pursuit of cost effectiveness and simplicity. The wind turbine has a 2 MW capability; it generated 3 GWh of power the year after its construction (www.principlepowerinc.com).

Another FOWT has been in operation since 2013 on offshore Nagasaki, Japan (Utsunomiya et al., 2015). Its type of platform is a hybrid-spar buoy, and it supports 2 MW of downwind-type turbines. The platform consists of a steel and precast pre-stressed concrete. The diameter of the platform is 7.8 m at the main section and 4.8 m at the water's

surface. The hub height is 56 m above the water's surface, and the draft is 76 m. The platform is attached to the seabed by three anchored chains. Fukushima Shinpuu FOWT was deployed in Fukushima, Japan in 2015. The platform is a V-shaped semi-submersible with eight mooring lines; the wind turbine's capacity is 7 MW, making it the world's largest floating wind turbine (www.fukushima-forward.jp).

Since structures of FOWTs in deep water are floaters, they must be constrained by a mooring or tendon system. Because the mooring system plays an important role in the floating structure's movement, an accurate prediction of the mooring system's behavior is crucial. Several simulation tools have been developed to predict FOWT behavior, such as HAWC2 and FAST. HAWC2 was developed by DTU Wind Energy of Denmark to simulate FOWT responses. FAST was created by the National Renewable Energy Laboratory (NREL), and it is one of the most well-known simulation tools. Through Offshore Code Comparison Collaboration (OC3), the performance of FAST was successfully verified against other numerical codes such as HAWC2 and Simo (Jonkman and Musial, 2010).

Along with the development of FOWT simulation tools, several model tests were conducted to understand FOWT motion characteristics, as well as to validate the related numerical simulation tools. Hydro Oil & Energy tested a spar-type platform with a 5 MW wind turbine at the Ocean Basin Laboratory of Marintek in Norway (Nielsen et al., 2006). At the basin of the Maritime Research Institute Netherland (MARIN), model tests of a 1:50 scale were implemented for three different types of platforms: spar-buoy, semi-submersible, and TLP-type coupled with the NREL 5MW baseline wind turbine (Goupee

et al., 2014). They provided the FOWT configurations, setup details, and measurement sensors and devices. The different concepts of FOWTs were then compared under various sea states and wind conditions (Koo et al., 2012). Recently, Hywind experiments were conducted at the Deepwater Offshore Basin in Shanghai Jiao Tong University (SJTU) of a 1:50 scale (Duan et al., 2015).

Despite the many numerical codes developed and model tests conducted, there have been few published studies comparing the results of model tests and numerical simulations. Regarding the 5MW wind turbine supported by the Hywind platform, Nielsen et al. (2006) presented a comparison of predicted and measured surge motions at the nacelle under various wind and wave conditions. Two different numerical codes (HywindSim and Simo-Riflex) were used for the simulation, and they rendered similar predictions. While the comparisons showed that the predicted surge motions in the wave frequency range were close to the measurements, predictions in the range of resonant pitch and surge frequencies were found to be significantly different (by 100% to 200%) from the related measurements. More recently, Browning et al. (2012) conducted numerical simulations using FAST and compared them to measurements of a 1:50 scaled model (Hywind) made in the MARIN's wave basin (Martin et al., 2012). After comparing the *x*-axis direction acceleration at the top of the wind tower and heave of the spar, they showed that the wave frequency predictions and measurements were close, but there were large discrepancies in the resonant pitch and surge frequencies, consistent with observations made in a previous study by Nielsen et al. (2006). It should be noted that no comparisons of predicted and measured mean motions were presented in these two studies.

In OC3 project, the Hywind FOWT was chosen as the subject for the numerical simulation (Jonkman and Musial, 2010). Its supporting platform is a spar constrained by a delta mooring system, also known as a crowfoot, which increases the yaw station-keeping capacity of the FOWT. As shown in Figure 2, each mooring line of a delta mooring system is typically composed of three segments. The two short segments are attached at two separated fairleads at the same horizontal level to the spar. They extend out to meet and connect to a long major segment that attaches an anchor to the seafloor.

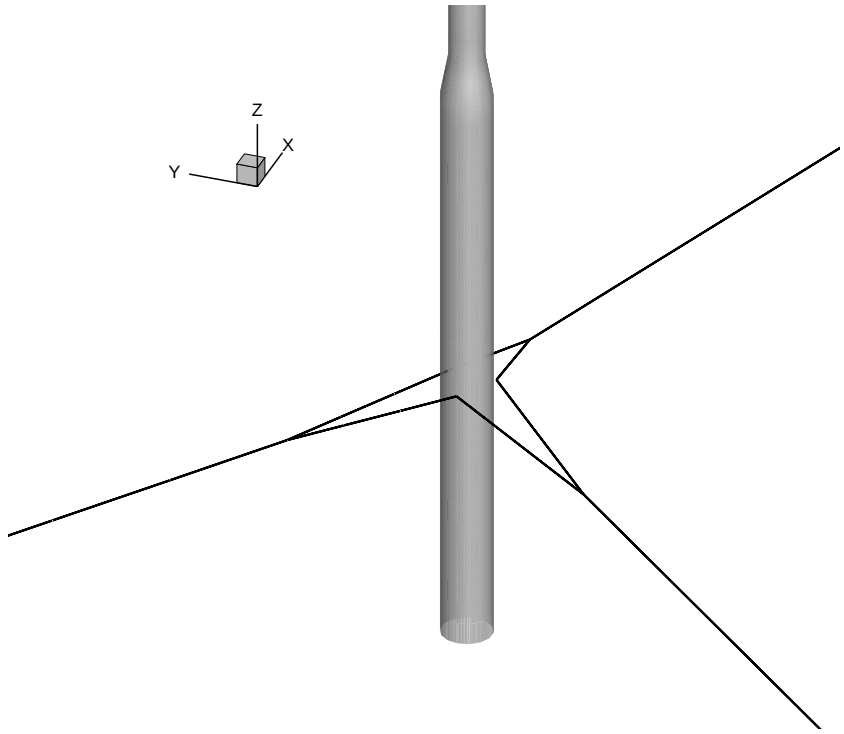

Figure 2 Delta Mooring System

Version 7 of FAST is unable to calculate behaviors related to the dynamic mooring loads because it uses a quasi-static approach. Later, FAST was combined with other conventional offshore design codes, such as OrcaFlex, COUPLE, and CHARM3D, to

utilize their ability to calculate dynamic mooring loads. Although FAST was coupled with various offshore design codes, it still relied on empirical tunings on the yaw stiffness and damping to simulate the delta mooring system. Several previous studies (Bae et al., 2011; Browning et al., 2012; Min et al., 2016) used empirically calibrated increases in the yaw stiffness and damping for the delta mooring system. Then the three segments of mooring line were simplified to an equivalent conventional one-segment mooring line in the simulations.

Efforts have been made to validate empirically calibrated increases in the yaw stiffness and damping of a delta mooring system. Kallesøe and Hansen (2011) developed a dynamic mooring line model, which was coupled with HAWC2. In their study, the delta mooring system was analyzed using a multi-body formulation in HAWC2. The results obtained using their program were compared to those obtained using a quasi-static approach. They concluded that the bending equivalent loads at the bottom of the wind tower computed by the direct modeling approach were less than those calculated by the quasi-static approach. Quallen et al. (2013) introduced a quasi-static mooring model for the delta mooring. Their codes were coupled with a CFD-based hydrodynamic simulation code. They verified their code against the related results of OC3 (Jonkman and Musial, 2010) in free-decay and regular wave-only tests. Hall and Goupee (2015) developed a lumped-mass mooring line model and verified it by comparing it to experimental results from the DeepCWind, a semi-submersible FOWT. Their code could be used to simulate a delta mooring system, and was utilized later by Andersen et al. (2016).

Various mooring analysis tools have been released in version 8 of FAST, including Map++, MoorDyn, and FEAMooring. Map++ uses a quasi-static approach to model a mooring system. MoorDyn employs a lumped-mass method, and FEAMooring applies a Finite Element Method (FEM). The last two approaches (the lumped-mass method and FEM) have also been used in commercial offshore design codes. Despite the many numerical codes have been released for the mooring system analysis, very few are specialized for the dynamic simulations of a delta mooring system. Wendt et al. (2016) verified the applicability of the MoorDyn, FEAMooring, and Map++ mooring modules in version 8 of FAST in the simulation comparing with DeepCWind test results. However, they did not examine the delta mooring system. Andersen et al. (2016) focused on validating the ability of version 8 of FAST to model the Hywind's delta mooring system. They used Map++ and MoorDyn to compare simulations obtained using FAST-OrcaFlex. In their study, FEAMooring was not employed because it was unable to model a delta mooring system directly. The simulation data for free-decay and wave-only tests were compared with the OrcaFlex simulation and related measurements obtained from the MARIN's basin test. The results calculated by the dynamic mooring solver, MoorDyn, showed a satisfactory level of agreement with those of OrcaFlex. They also found that the direct modeling of a mooring system can provide far more accurate results regarding mooring line tensions than the simplified mooring line approach with an empirically-calibrated increase in yaw stiffness and damping.

1.2. Overview of the Research Work

In this research, COUPLE-D-FAST was developed allowing for the simulation of a delta mooring system. It was then applied to the simulations of the Hywind FOWT. The mooring module in COUPLE-D-FAST was developed using FEM, as in the case with FEAMooring (Version 8 of FAST), but our software can simulate a delta mooring system. The developed module was combined with existing code entitled COUPLE-FAST and named COUPLE-D-FAST.

The main advantages of using COUPLE include the accurate prediction of hydrodynamic and mooring loads. First, the Hybrid Wave Model (HWM) (Zhang et al., 1996) was chosen to compute the wave kinematics, which led to accurate predictions of nonlinear wave interactions. The ratio of the diameter of the Hywind platform to the wave length at the spectral peak was small enough to allow for the slender-body approximation. Thus, the wave loads (both potential and drag forces) were calculated by the Morison equation, and the wave kinematics were predicted using the HWM. Since HWM was able to predict the wave kinematics at a second order wave steepness up to the free surface, there was no need to use an empirical stretch or approximation such as linear extrapolation or wheeler stretching. Regarding the mooring dynamics in COUPLE-D, the delta mooring system could then be explicitly modeled for a dynamic simulation. Hence, the yaw stiffness and damping of a delta mooring system could be accurately calculated without relying on empirical tunings.

This dissertation provides a description of how to model a delta mooring system; using the case of Hywind FOWT with a taut delta mooring system. COUPLE-D-FAST

was employed to simulate the FOWT's motion and tension in its mooring system. The dynamic behaviors of the delta mooring system obtained using COUPLE-D-FAST were then compared with the results of other existing codes such as COUPLE-FAST and FAST-OrcaFlex, as well as the measurements of SJTU (Duan et al., 2015).

2. DYNAMICS OF A DELTA MOORING SYSTEM

For simulations of a delta mooring system, the CABLE3D module (Ma and Webster, 1994), the mooring module in COUPLE, is modified. The mooring module is based on FEM. It follows Garrett (1982)'s principle for an inextensible cable and Lindahl and Sjoberg (1983)'s study for an extensible cable. The detailed derivation of the governing equations for an extensible mooring line can be found in Chen (2002). In this section, the governing equations and the numerical formulation especially for the delta mooring system are described.

2.1. Dynamic Equations for an Extensible Mooring Line

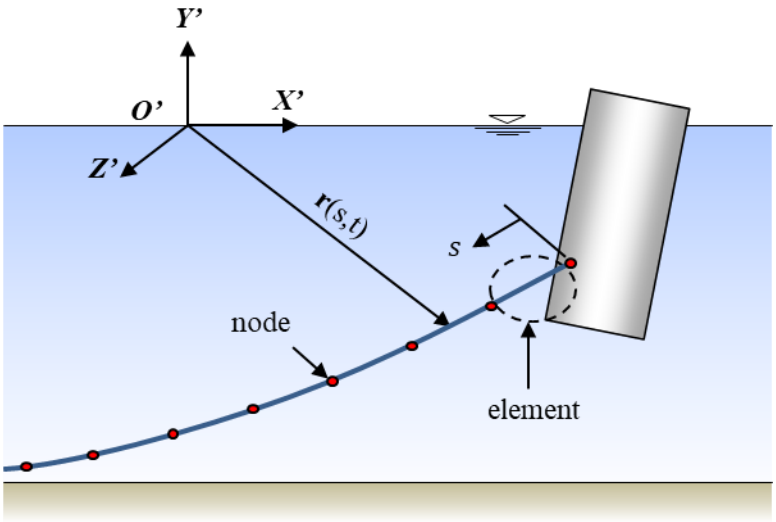

Figure 3 Discretization of a Cable

In using FEM to compute mooring dynamics, an extensible mooring line can be considered as the long slender cable, and the bending moments and shear forces are

neglected. As shown in Figure 3, the FEM discretizes the long slender cable into many elements that each element has two nodes at both ends. Mooring line tension *T* is the only internal force.

The configuration of a cable can be represented by a vector, **r**(*s*,*t*), where *s* and *t* represent the arc length along the cable, and time, respectively. Based on the conservation of linear momentum the governing equation can be expressed as follows together with a stretching constraint condition:

$$\mathbf{M}\ddot{\mathbf{r}} - (\tilde{\lambda}\mathbf{r}')' = \mathbf{q} \tag{2.1}$$

$$\mathbf{r}' \cdot \mathbf{r}' (1 - \frac{\tilde{\lambda}}{EA})^2 = 1 \tag{2.2}$$

where, **M** is the mass matrix, $\tilde{\lambda}$ is the Lagrange multiplier which can be expressed using the normal strain ε and the tension in a cable, $\tilde{\lambda} = T/(1+\varepsilon)$. **q** is the external forces distributed on the cable; it includes hydrostatic, hydrodynamic and gravity forces. *EA* is the axial stiffness of the cable. A superposed dot denotes the derivatives with respect to time, and a prime the derivatives with respect to space.

2.2. Numerical Implementation: Finite Element Method

To solve the motion equation and the constraint equation for the unknowns, **r** and $\tilde{\lambda}$, the Galerkin method is employed to discretize the partial differential equation (2.1)

and the constraint equation (2.2). The configuration of the cable (**r**) is approximated by Hermite cubic interpolation $a_i(s)$, the Lagrange multiplier ($\tilde{\lambda}$), external forces (**q**), and mass matrix of the cable (**M**) are estimated by quadratics, $p_m(s)$. With selections of the shape functions, the unknowns and the other variables can be expressed with the tensor notation:

$$\begin{aligned}
\mathbf{r}(s,t) &= u_{in}(t)a_i(s)\mathbf{e}_n \\
\tilde{\lambda}(s,t) &= \tilde{\lambda}_m(t)\,p_m(s) \\
\mathbf{q}(s,t) &= q_{mn}(t)\,p_m(s)\mathbf{e}_n \\
\mathbf{M}(s,t) &= \mathbf{M}_m(t)\,p_m(s)
\end{aligned} \tag{2.3}$$

The shape functions for Hermite cubic and quadratics are respectively:

$$\begin{aligned}
a_1(\xi) &= 1-3\xi^2+2\xi^3 \\
a_2(\xi) &= \xi-2\xi^2+\xi^3 \\
a_3(\xi) &= 3\xi^2-2\xi^3 \\
a_4(\xi) &= -\xi^2+\xi^3
\end{aligned} \tag{2.4}$$

$$\begin{aligned}
p_1(\xi) &= 1-3\xi+2\xi^2 \\
p_2(\xi) &= 4\xi(1-\xi) \\
p_3(\xi) &= \xi(2\xi-1)
\end{aligned} \tag{2.5}$$

where, $\mathbf{e}_n$ is a unit vector for translational directions, and ξ is a non-dimensional and normalized coordinate defined by $\xi=s/L$, and L is the un-stretched length of an element. The ranges of subscripts are n = 1 - 3 for translational directions, i = 1 - 4 for the index of

Hermite cubics, and m = 1 - 3 for the index of quadratics. The coefficients of shape functions are given by:

$$\begin{aligned} u_{1n}(t) &= \mathbf{r}_n(0,t) \\ u_{2n}(t) &= L\mathbf{r}'_n(0,t) \\ u_{3n}(t) &= \mathbf{r}_n(L,t) \\ u_{4n}(t) &= L\mathbf{r}'_n(L,t) \end{aligned} \tag{2.6}$$

$$\begin{aligned} \tilde{\lambda}_1(t) &= \tilde{\lambda}(0,t) \\ \tilde{\lambda}_2(t) &= \tilde{\lambda}(L/2,t) \\ \tilde{\lambda}_3(t) &= \tilde{\lambda}(L,t) \end{aligned} \tag{2.7}$$

By applying Galerkin method to the partial differential equation (2.1), we can reduce it to a set of ordinary differential equations. The partial differential equation (2.1) is multiplied by the Hermite cubics, $a_i(s)$, and then integrated with respect to the length of an element, L:

$$\int_0^L \left\{ \mathbf{M}\ddot{\mathbf{r}} - (\tilde{\lambda}\mathbf{r}')' - \mathbf{q} \right\} a_i(s)\, ds = 0 \tag{2.8}$$

After integrating Equation (2.8) by parts, the equation can be written as:

$$\int_0^L \left\{ \mathbf{M}\ddot{\mathbf{r}} a_i(s) + \tilde{\lambda}\mathbf{r}' a_i'(s) - \mathbf{q}\, a_i(s) \right\} ds = \tilde{\lambda}\mathbf{r}'\, a_i(s)\Big|_0^L \tag{2.9}$$

The right-hand side of the above equation represents the forces applied at the two ends of an element which are named as generalized forces, $\mathbf{f}_i$.

$$\begin{aligned}
&\mathbf{f}_i = \tilde{\lambda}\mathbf{r}'\, a_i \big|_0^L \\
&\mathbf{f}_1 = -\tilde{\lambda}\mathbf{r}'(0) = -\mathbf{F}(0) \\
&\mathbf{f}_2 = 0 \\
&\mathbf{f}_3 = \tilde{\lambda}\mathbf{r}'(L) = \mathbf{F}(L) \\
&\mathbf{f}_4 = 0
\end{aligned} \tag{2.10}$$

We also obtain the constraint equation as follows:

$$\int_0^L \frac{1}{2} p_m(s) \left\{ \mathbf{r}' \cdot \mathbf{r}' (1 - \frac{\tilde{\lambda}}{EA})^2 - 1 \right\} ds = 0 \tag{2.11}$$

Letting $\tilde{\varepsilon}$ be $\tilde{\lambda} / EA$ and plugging the expressions (2.3) into (2.9) and (2.11), we can obtain the discretized forms of the ordinary differential equations (2.12) and the constraint equations (2.13), respectively.

$$\gamma_{ikm} M_{njm} \ddot{u}_{kj} + \beta_{ikm} \tilde{\lambda}_m u_{kn} = \mu_{im} q_{mn} + f_{in} \tag{2.12}$$

$$\frac{1}{2} \beta_{ikm} u_{in} u_{kn} + \frac{1}{2} \tilde{\eta}_{iklm} (-2\tilde{\varepsilon}_l + \tilde{\varepsilon}_l^2) u_{in} u_{kn} - \frac{1}{2} \tau_m = 0 \tag{2.13}$$

where, i, k = 1 – 4, and j, l, m = 1 – 3. It should be noted that f_{in} is a tensor form of the generalized forces. The coefficients in the equations are defined by:

$$
\begin{aligned}
\beta_{ikm} &= \frac{1}{L}\int_0^1 a_i'(\xi)a_k'(\xi)p_m(\xi)d\xi \\
\gamma_{ikm} &= L\int_0^1 a_i(\xi)a_k(\xi)p_m(\xi)d\xi \\
\mu_{im} &= L\int_0^1 a_i(\xi)p_m(\xi)d\xi \\
\tau_m &= L\int_0^1 p_m(\xi)d\xi \\
\tilde{\eta}_{iklm} &= \frac{1}{L}\int_0^1 a_i'(\xi)a_k'(\xi)p_l(\xi)p_m(\xi)d\xi
\end{aligned}
\tag{2.14}
$$

Equation (2.12) involves twelve second-order ordinary differential equations, and Equation (2.13) results in three algebraic equations. Let ${}^{(K)}u_{in}(t)$ and ${}^{(K)}\tilde{\lambda}_m(t)$ be values at time step (*K*), then the updated values of u_{in} and $\tilde{\lambda}_m$ at the next time step (*K*+1) are as follows:

$$
\begin{aligned}
{}^{(K+1)}u_{in} &= {}^{(K)}u_{in} + \Delta u_{in} \\
{}^{(K+1)}\tilde{\lambda}_m &= {}^{(K)}\tilde{\lambda}_m + \Delta\tilde{\lambda}_m
\end{aligned}
\tag{2.15}
$$

Substituting (2.15) into (2.12) and (2.13), and discarding the higher order terms, the 15 equations for an element of the cable can be written in a matrix form, [**A**][Δ**X**]=[**B**]. The unknown vector, Δ**X**, is defined as follows:

$$
\begin{aligned}
\left[\Delta\mathbf{X}\right] = (&\Delta u_{11},\ \Delta u_{12},\ \Delta u_{13},\ \Delta u_{21},\ \Delta u_{22},\ \Delta u_{23},\Delta\tilde{\lambda}_1,\Delta\tilde{\lambda}_2, \\
&\Delta u_{31},\ \Delta u_{32},\ \Delta u_{33},\ \Delta u_{41},\ \Delta u_{42},\ \Delta u_{43},\Delta\tilde{\lambda}_3)^T
\end{aligned}
\tag{2.16}
$$

2.3. Boundary Conditions

In modeling a delta mooring system by FEM, four kinds of boundary conditions are defined at four different locations namely, the fairleads, the smoothly connected points, the joint of the three mooring segments, and the bottom as shown in Figure 4. At the fairleads of mooring segments 1 and 2, hinged boundary conditions are applied. It should be noted that the boundary conditions other than the hinge can be straightforwardly extended. The support of the seabed is modeled as an elastic system.

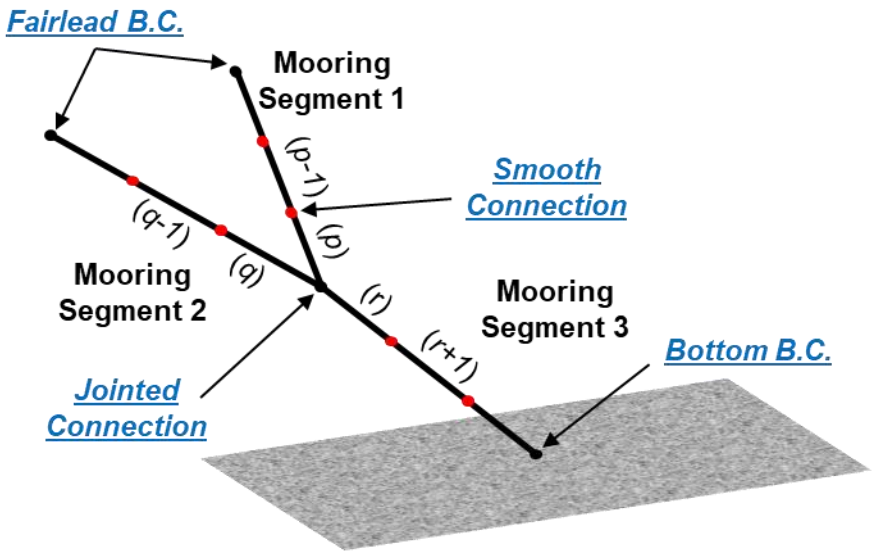

Figure 4 Boundary Conditions of Delta Mooring System

2.3.1. Boundary Conditions at the Smooth Connections

Elements within each mooring segment in Figure 4 are smoothly connected at the internal nodes if no concentrated external forces are applied. That is, the displacements and gradients of the adjacent elements should be the same, while the internal tensions are

of the same value (but opposite directions). Therefore, the boundary conditions can be expressed as:

$$\begin{aligned} {}^{(p-1)}u_{3n} &= {}^{(p)}u_{1n} \\ {}^{(p-1)}u_{4n} \,/\, {}^{(p-1)}L &= {}^{(p)}u_{2n} \,/\, {}^{(p)}L \\ {}^{(p-1)}\tilde{\lambda}_3 &= {}^{(p)}\tilde{\lambda}_1 \end{aligned} \tag{2.17}$$

where, (*p-1*) and (*p*) are indices of the neighboring elements, and ${}^{(p-1)}L$ and ${}^{(p)}L$ are the length of (*p-1*) and (*p*) elements respectively. If there are no external forces and moments, the generalized internal force should be balanced:

$${}^{(p-1)}f_{3n} + {}^{(p)}f_{1n} = 0 \tag{2.18}$$

2.3.2. Boundary Conditions at the Jointed Connections

Similar to the boundary conditions at the smooth connection, the force at the joint of the three segments should be balanced in the absence of concentrated external forces, and the displacements at the jointed nodes of three neighboring elements have to be the same. However, the gradients and the internal tensions of the elements at the jointed point will not be the same. As shown in Figure 4, if elements (*p*), (*q*) and (*r*) are jointed, the boundary conditions are:

$${}^{(p)}u_{3n} = {}^{(q)}u_{3n} = {}^{(r)}u_{1n} \tag{2.19}$$

$$ {}^{(p)}f_{3n} + {}^{(q)}f_{3n} + {}^{(r)}f_{1n} = 0 \qquad (2.20) $$

2.4. Formulation

The 15 unknowns of each element shown in equation (2.16) are governed by 15 equations. Since neighboring elements share 7 unknowns based on the boundary conditions (2.17), the total unknowns for a cable can be reduced to 15+8(N-1) if a cable has N elements without a delta joint. When the algebraic equations are summed up by assembling procedure as shown in Figure 5, the summed generalized forces between adjacent elements at the right-hand-side of equation, denoted by [***B'***], are cancelled out owing to the force balancing condition (2.18). The prime denotes an assembled form of [***B***]. Bandwidth of the coefficient matrix [***A'***] is 29.

For the case of a delta mooring line, the assembled matrix of each mooring segment can be further manipulated using the boundary conditions (2.19). As a result, the total unknowns for a delta mooring line can be reduced to 15+8(N_1+N_2+N_3), where N_1, N_2 and N_3 are the numbers of elements for the three segments, respectively. Similar to the force balancing condition for the case of smoothly connected elements, the boundary conditions (2.20) are also satisfied in the right-hand side matrix [***B'***] of the assembled equations.

Figure 6 attempts to visualize how to assemble the matrix [***A'***] for the case of a delta mooring line. For example, in this figure, the two hull-side (short) mooring segments (A1 and A2) are divided into two elements (N_1=N_2=2), respectively. To assemble the matrix of the three mooring segments, the coefficient matrix of the jointed elements among

mooring segments A1 and A2 should be rearranged in order to apply the boundary condition (2.19). The unknown vectors for these last elements can be expressed as:

$$\begin{aligned}\left[\Delta\mathbf{X}\right] = (&\Delta u_{11},\ \Delta u_{12},\ \Delta u_{13},\ \Delta u_{21},\ \Delta u_{22},\ \Delta u_{23}, \Delta\tilde{\lambda}_1, \Delta\tilde{\lambda}_2, \\ &\Delta u_{41},\ \Delta u_{42},\ \Delta u_{43}, \Delta\tilde{\lambda}_3,\ \Delta u_{31},\ \Delta u_{32},\ \Delta u_{33})^T\end{aligned} \tag{2.21}$$

In comparison with equation (2.16), the coefficients related to the displacements of the joint node occupy the last three rows and the last three columns in the coefficient matrix of the elements N_1 and N_2. Firstly, the mooring segments A2 and B form the assembled matrix by sharing the displacements of the jointed node. Next, the last 3×3 diagonal part in the matrix of the element N_1 are later added to the overlapped parts (3×3) of the previously assembled matrix, i.e., the purple box in Figure 6. The rest of the coefficients in the last three rows and columns of the element N_1's matrix, i.e., the blue boxes in Figure 6, is rearranged by aligning with the overlapped part. The bandwidth depends on the number of elements for the hull-side mooring segments (N_2), and its values are $16N_2$+37. Since the bandwidth of the systems of equations for a delta mooring line is larger than the one for the single mooring line, it requires relatively high computational costs.

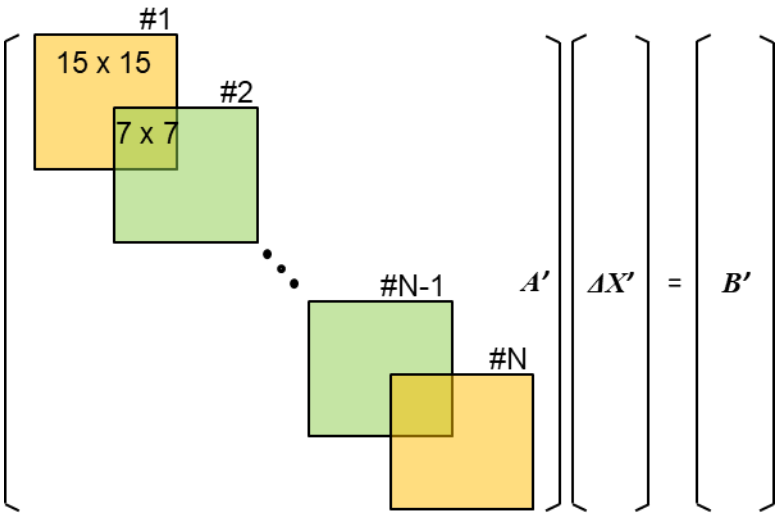

Figure 5 Assembled Matrix for a Cable with *N* Elements

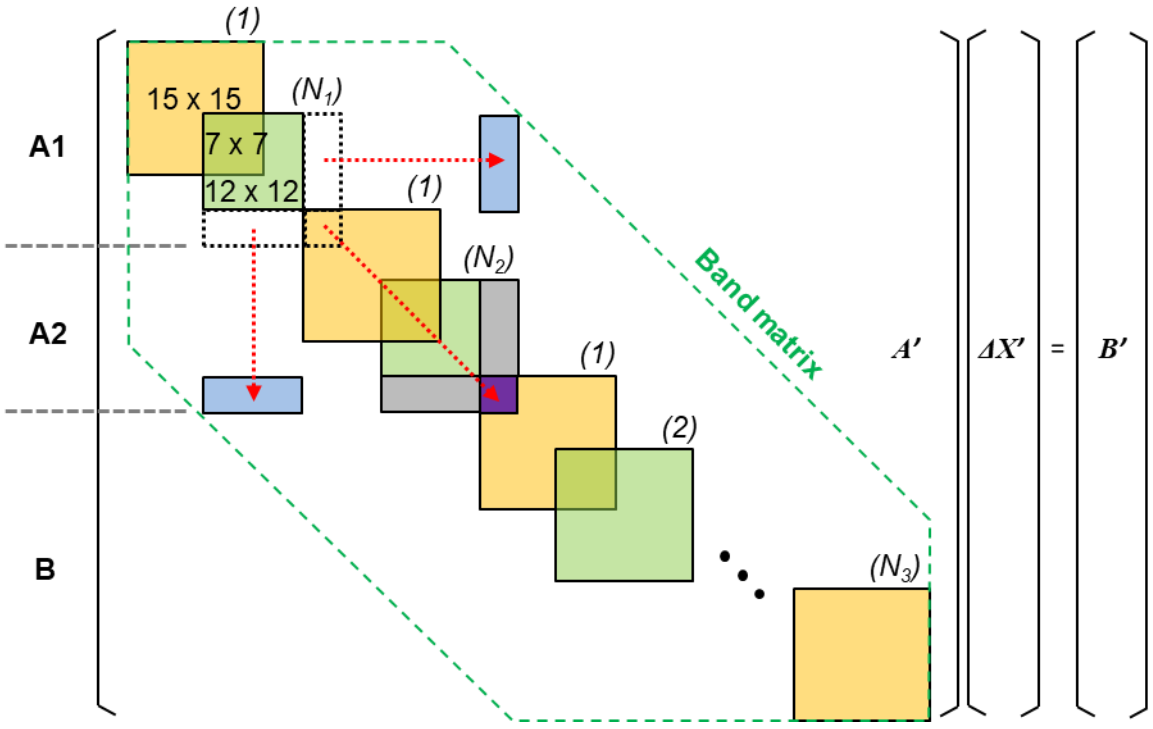

Figure 6 Assembled Matrix for a Delta Mooring System

3. PRINCIPLES OF COUPLE-D-FAST

In this research, a numerical code called COUPLE-D-FAST is used to investigate the FOWT dynamic responses. The code consists of two major modules, known as COUPLE-D and FAST. Briefly, COUPLE-D calculates hydro-related forces, responses of a delta mooring system, and 6 degrees of freedom (DOF) motions of a FOWT while FAST computes wind-related forces and elastic forces of the tower and blades. The overview of this code and some of the principles of modeling are described in following subsections.

3.1. Modeling of FOWT in COUPLE-D

COUPLE (or COUPLE-D) was developed to analyze interactions between a platform and its mooring lines or risers in time domain simulation which was and is being developed by Prof. Jun Zhang and his former and current graduate students at Texas A&M University and is written in FORTRAN (Cao and Zhang, 1997; Chen, 2002; Peng et al., 2014; Min et al., 2016; Min and Zhang, 2017).

The Hywind FOWT system consists of a wind turbine, a floating platform moored by a delta mooring system. When Hywind is modeled by COUPLE-D, the wind turbine components are considered as rigid structures, i.e. the flexibility of the tower and blades is not considered in COUPLE-D.

The 6 DOF nonlinear motion equations of a platform are coupled with the wind external forces on the wind turbine governed by the aero-servo-elastic dynamic equations

and the dynamic equations of mooring lines through hinge boundary conditions. To solve the motion equations in COUPLE-D, the Newmark-β method scheme is selected and combined with iteration procedures to advance in time domain. The 6 DOF motion equations can be summarized as (Paulling and Webster, 1986):

$$\left[\mathbf{M}_{\mathrm{s}}+\mathbf{M}_{\mathrm{a}}\right]\ddot{x}(t)+\mathbf{B}\,\dot{x}(t)+\mathbf{C}\,x(t)=\mathbf{F} \tag{3.1}$$

where, $\mathbf{M}_{\mathrm{s}}$ is the mass matrix of the FOWT system, $\mathbf{M}_{\mathrm{a}}$ is the added matrix, **B** the damping matrix and **C** the restoring stiffness matrix. **F** denotes the summation of external forces which include current forces, wave forces, mooring forces, aero-servo-elastic forces, etc.

One of the dominant external forces acting on the floating structures is wave forces. COUPLE-D-FAST has two options for calculating wave forces on the floating structure, the second-order diffraction/radiation theory and the Morison equation using HWM.

A wave diffraction and radiation potential theory is the well-known method to calculate wave forces, and one of the well-known numerical codes is WAMIT. In the potential theory, the wave potential is solved numerically using a Boundary Element Method in a frequency domain. Forces of this method consist of wave exciting forces, added mass forces, and radiation damping forces. Wave drift damping forces could be calculated by a heuristic formula (Aranha, 1994; Clark et al., 1993) without solving a second-order low-forward speed diffraction and radiation problem. Then, all forces in

frequency domain are converted to forces in a time domain by the Inverse Fast Fourier Transform (IFFT) or the convolution integral.

In this study, wave forces are calculated by the Morison equation instead of the potential wave theory, since most FOWT platforms, like spar buoy, semi-submersible, and tension leg platform, can be modelled as the combination of slender members.

For cylindrical structures, the Morison equation can be used to approximate wave forces when the ratio of the typical wave length to the diameter is greater than 5 ($\lambda > 5D$). Accurate calculations of wave loads start with the accurate predictions of wave kinematics because the calculation of the Morison equation requires wave kinematics of the ambient fluid and the wave evolution. Wave kinematics could be calculated in many different methods, like the second-order wave theory, the linear extrapolation, the Wheeler stretching and the HWM. In this study, wave kinematics and wave elevations are calculated using the HWM. Because HWM predicts nonlinear wave kinematics up to free surface, the empirical stretching or approximations are not needed.

In using the HWM, an irregular wave spectrum is divided by three ranges: a very low frequency range (pre-long wave band), a powerful range, and a very high frequency region (restrictive band). The nonlinear effects wave components of a very low frequency region are negligible because the amplitudes in the region are relatively small. The wave components in the very high frequency region (restrictive band) are considered as the bond-wave components instead of free-wave components.

The spectrum in the powerful range are further divided into three bands, a long wave band and two of short wave bands as shown in Figure 7. The wave-wave interactions

within the same wave band are computed using the conventional perturbation approach. The interactions between different wave bands are calculated using the phase modulation approach. By applying the two different approaches, the solutions of wave kinematics quickly converge for a wave field of a broad-banded spectrum.

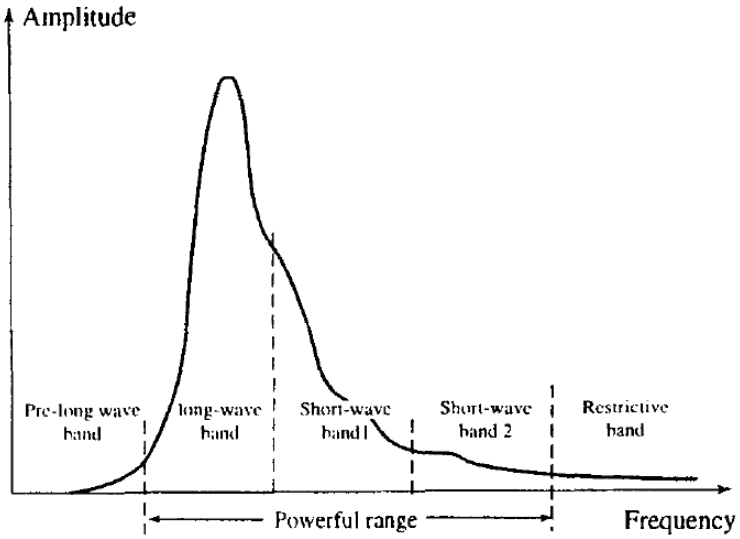

Figure 7 Wave Frequency Band Division; Reprinted from Zhang et al. (1996)

3.2. Modeling of FOWT in FAST

In COUPLE-D-FAST, the aerodynamic forces are simulated by the AeroDyn package in the FAST code. The FAST code is a nonlinear time domain simulator that uses a combined modal- and multibody-dynamics formulation. FAST is able to simulate most common wind turbine configurations and control scenarios (Jonkman, 2007). FAST combines aerodynamics models (aero), hydrodynamic model for offshore wind turbine (hydro), control and electrical system (servo), and structural dynamic models (elastic) to simulate coupled nonlinear aero-hydro-servo-elastic computation in a time domain.

In FAST, the flexibility of the blades and tower is calculated using a linear modal analysis. The nacelle and hub are considered as rigid bodies modelled by relevant lumped mass and inertia terms. All DOFs can be controlled by switches which allows one to increase or decrease the accuracy of the numerical model. The detailed explanation of the theoretical background of FAST can be found in Jonkman (2007) and Moriarty and Hansen (2005).

3.2.1. Wake and Airfoil Modeling

The effects of aerodynamics for aero-elastic simulations of horizontal axis wind turbine configurations are calculated using AeroDyn. It computes the aerodynamic lift, drag, and pitching moment of airfoil sections along the wind turbine blades, which are determined by dividing each blade into segments along the blade span. AeroDyn simultaneously collects the geometry of turbine, operating condition, blade-element velocity and location, and wind inflow. Those are employed to calculate the various forces for each segment, and then the forces are used for calculating the distributed forces on the blades. The aerodynamic forces have effect on turbine deflections and vice versa. AeroDyn takes advantage of relations based on two dimensional localized flows, and the properties of the airfoils along the blade are characterized by lift, drag, and pitching moment coefficients from results of wind tunnel experiment. (Moriarty and Hansen, 2005)

3.2.2. Blade and Tower Flexibility

The flexibility of the blades and tower is considered using a linear modal analysis with small deflections assumption for each member. The characteristics of the flexibility for each member are decided by the distribution of mass and stiffness properties along the

span of the members, and by specifying their shapes as polynomials. In this research, the functions of mode shapes are determined using BMODES which is a finite element code to provide dynamically coupled modes for a beam and provided by NREL. In FAST, blades behave in the directions of two flap-wise modes and an edgewise mode, and a tower behave in the directions of two fore-after and two side-to-side modes. When generating blade modes, the rotor speed will affect significantly the frequency of vibration while it slightly affects the mode shapes (Jonkman, 2007).

3.2.3. Control System

For the NREL 5 MW baseline wind turbine, two control systems are employed for a stability of a generator of the wind turbine: a generator-torque controller and a blade-pitch controller. The two control systems are modeled to operate individually in the below-rated and above-rated wind speed range, respectively. The generator-torque control system is intended for maximizing the power capture below the rated operation condition. The blade-pitch control system is intended for regulating the generator speed above the rated operation condition. (Jonkman et al., 2009)

3.3. Coupling Overview of COUPLE-FAST

In COUPLE-D-FAST, FAST is used to calculate the wind forces, the servo dynamic forces of a wind turbine, and the effects of flexible materials. On the other hand, COUPLE-D computes the mooring forces of a delta mooring system and the

hydrodynamic forces on the FOWT platform using HWM; as a result, COUPLE-D calculates the global motions of the FOWT platform using the forces estimated by FAST.

In terms of the components of a structure, the major difference among COUPLE-D and FAST is the flexibilities of a tower and blades of a wind turbine. Both programs consider the bodies of a platform as rigid structures, but FAST considers the tower and blades as flexible parts, which differs from that COUPLE-D assumes the whole parts of FOWT are rigid. Therefore, the appropriate correction for the differences is required for coupling the independent programs. FAST computes the forces at the bottom of the turbine tower which include wind forces and servo dynamic forces as well as inertial forces with flexibility. Meanwhile, COUPLE-D calculates the inertial forces above the bottom of the tower using the rigid-body assumption. The differences of the forces between FAST and COUPLE-D are calculated, and then directly used for the analysis of global motions of FOWT in COUPLE-D. The coupling procedure is described in Figure 8, and more details of the coupling procedure will be presented in following subsections.

The time step of the COUPLE-D module can be determined relating to that of FAST. The time step of COUPLE-D can be the same as that of FAST or larger than that because the motions of the tower (FAST) have large natural frequency compared to the motions of the supporting platform (COUPLE-D), and the forces acting on the floating platform (COUPLE-D) varies relatively slowly with respect to the forces on rotor/nacelle/tower (FAST). By applying a relatively large time step in COUPLE-D, the CPU time can decrease substantially (Peng, 2015). In this study, the time steps are 0.01 sec in the FAST module and 0.05 sec in the COUPLE-D module.

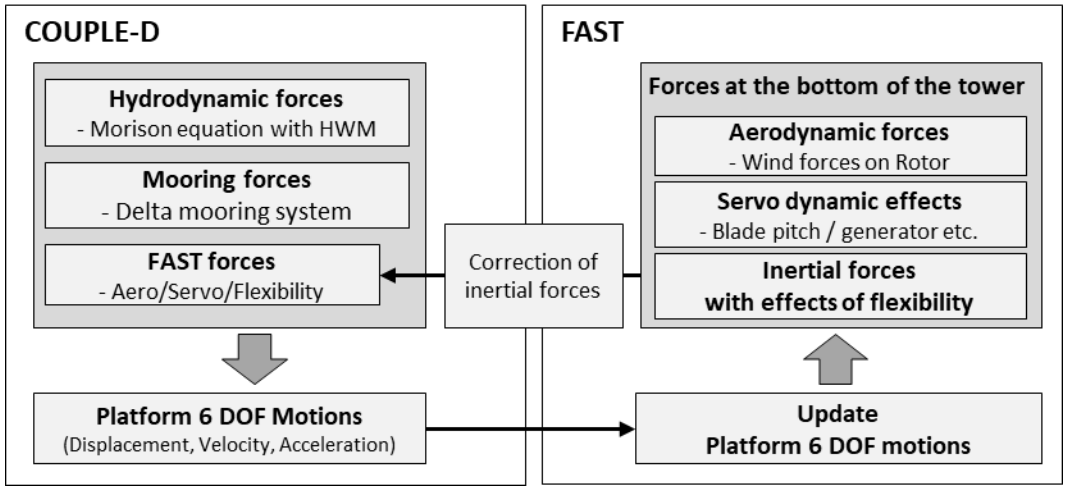

Figure 8 Flowchart of Coupling Procedure of COUPLE-D-FAST

3.3.1. Coordinate Systems

In COUPLE-FAST, several coordinate systems are employed to represent the motions of the FOWT. Major coordinate systems in the program represent the space-fixed coordinate system ($\hat{o}\hat{x}\hat{y}\hat{z}$), the global-reference coordinate system ($o_R x_R y_R z_R$), the tower-base coordinate system ($o_t x_t y_t z_t$), and the platform-body-fixed coordinate system (*oxyz*) as shown in Figure 9.

The space-fixed coordinate system ($\hat{o}\hat{x}\hat{y}\hat{z}$) depends on the wind direction set by the FAST module. The space-fixed coordinate system is fixed in space and it is employed in both the COUPLE-D module and the FAST module; this is called the inertial frame coordinate system in FAST. In this study, the origin of this coordinate system is located at the center of gravity of the FOWT. The positive $\hat{x}$-direction aligns with the nominal downwind direction, and $\hat{z}$-direction indicates the opposite direction of gravity. Another space-fixed coordinate system is the global-reference coordinate system ($o_R x_R y_R z_R$) and

is also fixed in space. The directions of winds, waves, currents, and mooring lines, can be defined by this coordinate system. As shown in Figure 10, its x_R and y_R axes are defined with respect to the angle of wind direction in the space-fixed coordinate system. The z-axis of this coordinate system coincides with that of the space-fixed coordinate system.

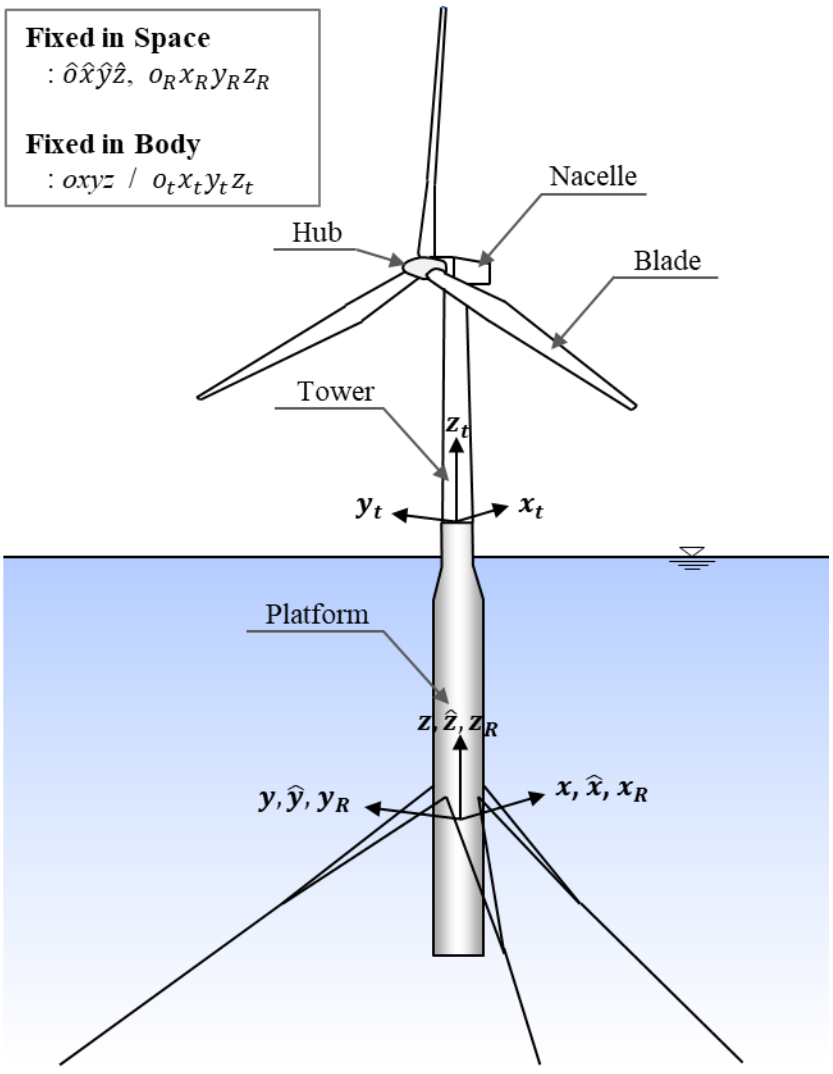

Figure 9 Coordinate Systems of Hywind in COUPLE-D-FAST

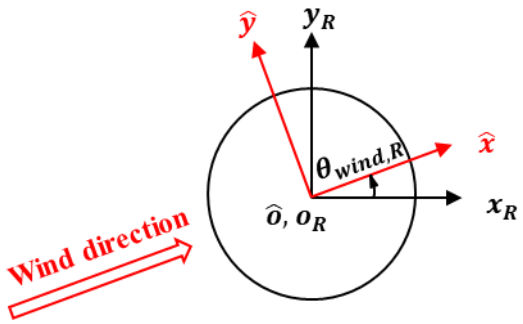

Figure 10 *xy*-Plane View of Space-fixed Coordinate System

The relation between the space-fixed coordinate system and the global-reference coordinate system can be determined by a transformation matrix **R** with the wind direction. Let the wind direction be $\theta_{wind,R}$ in the global reference coordinate system, then the relation between the coordinate systems follow as:

$$\mathbf{x_R} = \mathbf{R}\,\hat{\mathbf{x}} \tag{3.5}$$

where,

$$\mathbf{R} = \begin{bmatrix} \cos\theta_{wind,R} & -\sin\theta_{wind,R} & 0 \\ \sin\theta_{wind,R} & \cos\theta_{wind,R} & 0 \\ 0 & 0 & 1 \end{bmatrix} \tag{3.6}$$

There are two different body-fixed coordinate systems; the tower-base coordinate system ($o_t x_t y_t z_t$) and the platform-body-fixed coordinate system (*oxyz*). The tower-base coordinate system is fixed on the top of support platform in FAST. And its origin is located on the center of the tower base connected to the support platform. The platform-body-fixed coordinate system is used in the COUPLE-D module, and it is placed at any point of

the platform or the center of gravity. In this study, its origin point is located at the center of gravity of the FOWT. This coordinate system overlaps exactly with $\hat{o}\hat{x}\hat{y}\hat{z}$ when the platform is at its initial position. The two body-fixed coordinate systems move and rotate with the platform motion as shown in Figure 11.

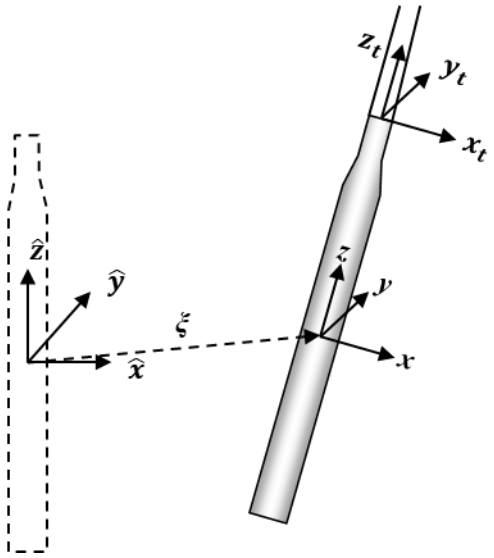

Figure 11 Body-fixed Coordinate Systems

The relation between the space-fixed coordinate system and the platform-body-fixed coordinate system is defined by a transformation matrix **T** with Euler angles. When the platform is moved with the translational motion, and is rotated with the Euler angles, the relation between **x** in *oxyz* and $\hat{\mathbf{x}}$ in $\hat{o}\hat{x}\hat{y}\hat{z}$ can be expressed as:

$$\hat{\mathbf{x}} = \boldsymbol{\xi} + \mathbf{T}^{t}\mathbf{x} \tag{3.7}$$

where,

$$\mathbf{T} = \begin{bmatrix} \cos\alpha_3\cos\alpha_2 & \sin\alpha_3\cos\alpha_1+\cos\alpha_3\sin\alpha_2\sin\alpha_1 & \sin\alpha_3\sin\alpha_1-\cos\alpha_3\sin\alpha_2\cos\alpha_1 \\ -\sin\alpha_3\cos\alpha_2 & \cos\alpha_3\cos\alpha_1-\sin\alpha_3\sin\alpha_2\sin\alpha_1 & \cos\alpha_3\sin\alpha_1+\sin\alpha_3\sin\alpha_2\cos\alpha_1 \\ \sin\alpha_2 & -\cos\alpha_2\sin\alpha_1 & \cos\alpha_2\cos\alpha_1 \end{bmatrix} \quad (3.8)$$

where, ξ is the translational motion, and α_1, α_2, and α_3 represent the angle of roll, pitch, and yaw in $\hat{o}\hat{x}\hat{y}\hat{z}$, respectively.

3.3.2. Mathematical Formulation of Coupling Problem

a. Static coupling problem

For the initial time step, COUPLE-D calculates the mean position by computing mean current and wave drifting forces acting on the platform and mooring lines' and hydrostatic restoring forces. This is initial position of the platform used in FAST. This static equation for the FOWT is expressed as:

$$\mathbf{C}\,x(t) = \mathbf{F}_{mean} + \mathbf{F}_{HSn} + \mathbf{F}_{M} \quad (3.9)$$

where, $\mathbf{F}_{mean}$ is mean forces applied on the platform of the FOWT, $\mathbf{F}_{HSn}$ is nonlinear restoring forces, and $\mathbf{F}_{M}$ is mooring system forces.

b. Dynamic coupling problem

The motion equations (3.1) can be modified as following expression under the Morison approach.

$$\left[\mathbf{M}_{\mathrm{s}}+\mathbf{M}_{\mathrm{a}}\right]\ddot{x}(t)+\mathbf{C}\,x(t)=\mathbf{F}_{mean}+\mathbf{F}_{current}+\mathbf{F}_{MR}+\mathbf{F}_{HSn}+\mathbf{F}_{M}+\mathbf{F}_{FAST} \tag{3.10}$$

where, $\mathbf{F}_{current}$ is the current forces, $\mathbf{F}_{MR}$ denotes the hydro dynamic forces computed using the Morison equation, and $\mathbf{F}_{FAST}$ represents the summation of the forces of winds, the servo-dynamic effects, and the effects of flexibility of tower and blades.

The inertial forces of the rotor, nacelle, and tower are calculated by the Newton's second law. The translational and rotational motion equations are expressed respectively as follows:

$$\hat{\mathbf{F}} = m\hat{\mathbf{a}}_g \tag{3.11}$$

$$\mathbf{M}_{\mathrm{o}} = \mathbf{M}_{\mathrm{g}} + \mathbf{r}\times\mathbf{T}\hat{\mathbf{F}} \tag{3.12}$$

where, ***m*** is the mass of each member, $\hat{\mathbf{a}}_g$ is the acceleration at the center of gravity for each member expressed in $\hat{o}\hat{x}\hat{y}\hat{z}$ (space-fixed), and $\hat{\mathbf{F}}$ is the inertial force for each member expressed in $\hat{o}\hat{x}\hat{y}\hat{z}$. $\mathbf{M}_o$ is the total moments expressed in *oxyz* (body-fixed). $\mathbf{M}_g$ is the moment at the center of gravity for each member with respect to the platform-body-fixed coordinate system. $\mathbf{r}$ is the vector of the center of gravity for each member in the platform-body-fixed coordinate system.

The acceleration of each member expressed in $\hat{o}\hat{x}\hat{y}\hat{z}$ can be written as:

$$\hat{\mathbf{a}}_g = \hat{\mathbf{a}}_o + \mathbf{T}^t\left(\frac{\partial\boldsymbol{\omega}}{\partial t}\times\mathbf{r}+\boldsymbol{\omega}\times(\boldsymbol{\omega}\times\mathbf{r})\right) \tag{3.13}$$

where, $\hat{\mathbf{a}}_o$ is the acceleration of the platform at the origin expressed in $\hat{o}\hat{x}\hat{y}\hat{z}$, and $\boldsymbol{\omega}$ is the angular velocity expressed in *oxyz*.

FAST returns the wind forces, the servo-dynamic effects, and the inertial forces above the bottom of the tower expressed in $o_t x_t y_t z_t$. The force vector $\mathbf{F}_{FAST}$ can be written as:

$$\mathbf{F}_{FAST} = \begin{Bmatrix} \mathbf{T}^t \mathbf{F}_t - (\hat{\mathbf{F}}_R + \hat{\mathbf{F}}_N + \hat{\mathbf{F}}_T) \\ \mathbf{M}_t + \mathbf{r}_{TB} \times \mathbf{F}_t - (\mathbf{M}_{g,R} + \mathbf{M}_{g,N} + \mathbf{M}_{g,T}) \end{Bmatrix} \tag{3.14}$$

where, $\mathbf{F}_t$ and $\mathbf{M}_t$ given by FAST are the forces and moments at the bottom of the tower expressed in $o_t x_t y_t z_t$, respectively. $\mathbf{r}_{TB}$ is the vector of the bottom of the tower expressed in *oxyz*. $\hat{\mathbf{F}}_R$, $\hat{\mathbf{F}}_N$ and $\hat{\mathbf{F}}_T$ represent the inertial forces of the rotor, nacelle, and tower which are calculated by COUPLE-D and expressed in $\hat{o}\hat{x}\hat{y}\hat{z}$, respectively. $\mathbf{M}_{g,R}$, $\mathbf{M}_{g,N}$ and $\mathbf{M}_{g,T}$ are the inertial moments of the rotor, nacelle, and tower which are calculated by COUPLE-D and expressed in *oxyz*, respectively.

3.3.3. Coupling Procedures of COUPLE-D-FAST

Since the time steps of the FAST and COUPLE-D modules are 0.01 sec and 0.05 sec, respectively in the program, COUPLE-D is only activated every five time steps of FAST. The coupling procedure is summarized as follows, and the flow chart is plotted in Figure 12.

1. Initial Position (t = 0 sec); Static Analysis
    1) COUPLE-D determines the mean position by the mean current and wave drifting forces on the platform, ant it transfers the position and forces into FAST.
    2) FAST sets the initial position of the FOWT using the position from COUPLE-D.
2. Time Marching Stage; Dynamic Analysis (t > 0 sec, and $t_{FAST} = t_{COUPLE}$)
    1) FAST collects all forces applied on the rotor/nacelle/tower with respect to the tower-base coordinate system, and it transports the forces to COUPLE-D.
    2) COUPLE-D calculates all forces acting on the platform, but excluding the aerodynamic portions. It also computes inertial forces of the rotor/nacelle/tower under the condition that COUPLE-D does not allow a deflection of each member. COUPLE-D subtracts the inertial forces from the forces given by FAST. As a result, the differences, equation (3.14), among the two kinds of forces represent the wind forces on the rotor, the servo-dynamic effects and the effects of flexibility of the tower and blades.
    3) Then, COUPLE-D predicts motions, velocities, and accelerations of the FOWT using all external forces including the differences from 2).
    4) Finally, COUPLE-D provides the predicted displacements, velocities, accelerations, and external forces for FAST.
3. Time marching stage (t > 0 sec, but $t_{FAST} \neq t_{COUPLE}$)

When the time of COUPLE-D is not the same as that of FAST, COUPLE-D does not calculate the updated forces corresponding with the time step in FAST, but it returns the forces of the previous time step.

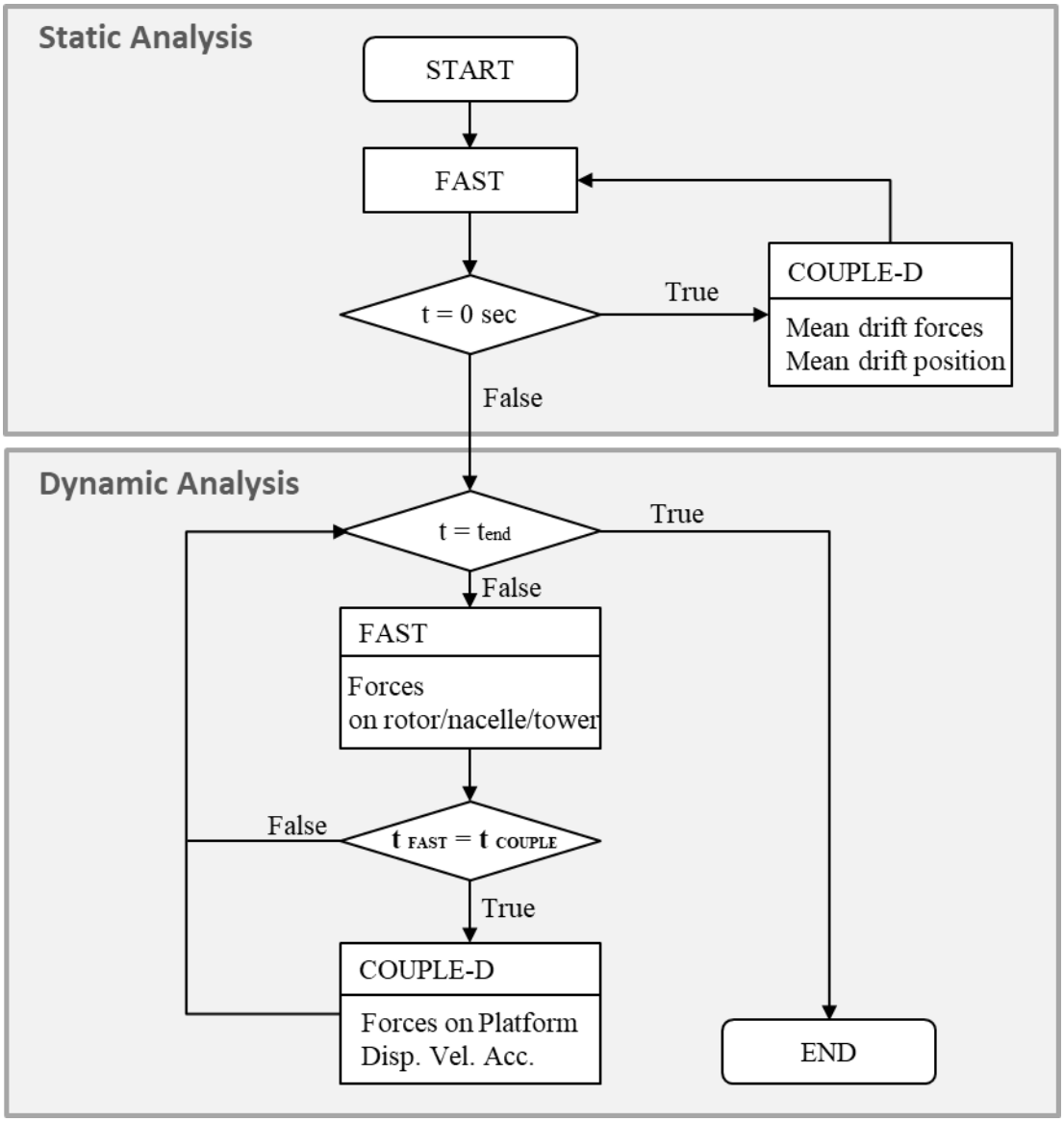

Figure 12 Flow Chart of Simulation Process in COUPLE-D-FAST

4. NUMERICAL MODEL SET-UP AND CALIBRATION

The 5 MW Hywind FOWT was employed for the model test and hence for the numerical simulations in this research. In the following subsections, the experimental facilities and set-up of the model are briefly described, and additionally, the calibration for certain parameters, such as the hydrodynamic coefficients and wind turbine tower stiffness used in the numerical simulations, is also described.

4.1. Model Experiments

4.1.1. Experimental Facilities

The behaviors of the Hywind FOWT under aerodynamic and wave loads were tested and measured in the Deepwater Offshore Basin in SJTU (Duan et al., 2015). The wave basin had the following dimensions 50 m (length) × 40 m (width) × 10 m (depth), and the waves and currents were achieved by a 222 multi-independence flap wave generator. The facility was able to produce quality wind fields using its generation system, which was designed and modified for the model tests. The wind generation system used nine axial fans to produce parallel wind fields. Its output dimensions were 3.76 m × 3.76 m and it had a capacity of up to 9.53 m/s. A honeycomb-shaped screen was placed in front of the wind fans to generate a steady wind-quality wind flow and to lower turbulence intensity.

4.1.2. Set-up of Model and Instruments

The prototype FOWT was geometrically scaled down following a 1:50 Froude similitude. The properties of the 5 MW NREL reference wind turbine (Jonkman et al., 2009) and floating system from the OC3 project (Jonkman, 2010) were used in the model test. The mooring system's properties and water depth followed the MARIN's experiment (Koo et al., 2012).

In the experiments, the properties of the wind turbine model were modified to be equipped with measuring instruments such as motion sensors and load cells. The mass properties of the SJTU's Hywind model were then compared with those of the prototype and the MARIN's model tests (see Table 1). It should be noted that the mass and length values listed refer to the prototype unless otherwise specified, and the center of mass represents the distance from the mean water level. The blades in the model test were made from woven carbon fiber epoxy composite materials due to limitations in mass scaling resulting from the Froude similitude. Thus, they could only be approximated as rigid, inflexible blades. The tilt angles of the shaft and blade pre-cone were 0 degrees, and blade pitch control was not allowed.

The spar-buoy platform of Hywind was also modified to match the mass and center of gravity of the total system by adjusting the metal ballast. The platform's main characteristics are listed in Table 2. The moment of inertia in yaw was not measured in the SJTU's model test. Thus, in this research the yaw moment of inertia was estimated by its counterpart in the MARIN's experiment (Koo et al., 2012). It was determined to be 100

$\times 10^6$ kg-m^2 based on the mass ratio of the SJTU's platform to the MARIN's platform. Figure 13 shows the installed FOWT model and the spar platform.

In the model tests, several measuring devices were installed, including an accelerometer, optical motion sensor, two load cells, and three tension sensors (as shown in Figure 14). One load cell was placed between the nacelle and tower, and the other was located at the rear part of the nacelle. The load cells were able to capture loads in three translational and three rotational directions. The accelerometer (3 DOF) was installed at the nacelle, and the optical motion sensor (6 DOF) was located at the bottom of the turbine tower. A taut delta mooring system with a 200 m water depth was employed in the SJTU's model test, which was accomplished by the MARIN's model test (Koo et al., 2012). Its layout and the locations of the tension sensors are depicted in Figure 14 (a). The properties of the delta mooring system are listed in Table 3.

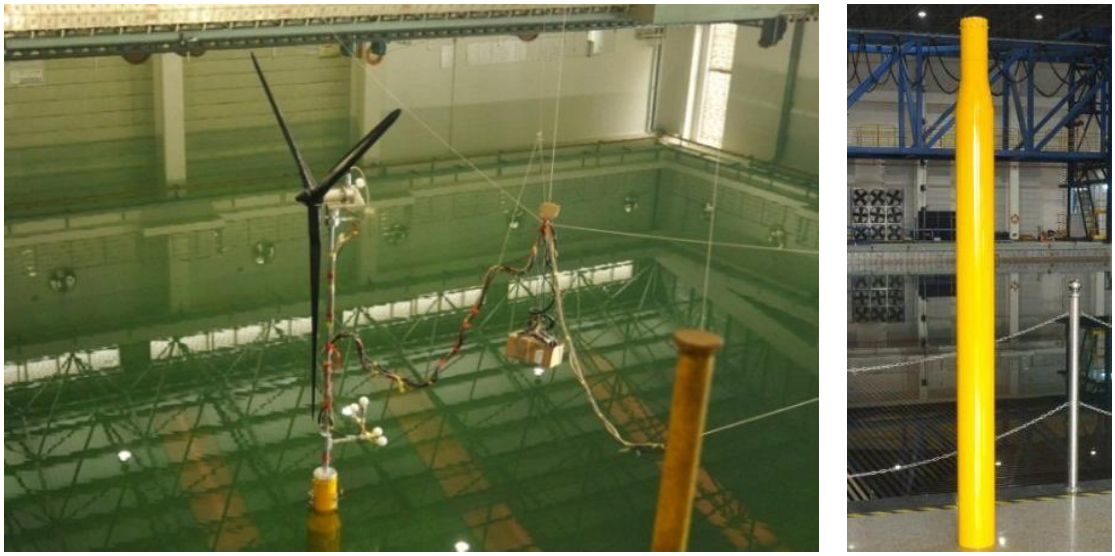

(a) (b)

Figure 13 Model Setting (a) and Floating Platform (b); Reprinted from Duan et al. (2015)

Table 1 Mass Properties of Hywind Model (Duan et al., 2015)

Property	Unit	NREL*	MARIN**	SJTU***
Blades	kg	53,220	48,750	52,659
Hub	kg	56,780	72,880	57,272
Nacelle	kg	240,000	274,900	239,082
Tower mass	kg	249,718	164,600	287,128
Instruments on tower	kg	-	137,640	113,391
Platform mass	kg	7,466,330	7,281,600	7,316,578
Total system mass	kg	8,066,048	7,980,370	8,066,110
Total system center	m	-78.00	-76.35	-78.95

* Jonkman and Musial (2010);** Koo et al. (2012);***Duan et al. (2015)

Table 2 Platform Properties of Hywind Model

Property	Unit	NREL*	MARIN**	SJTU***
Overall length	m	130	130	130
Draft	m	120	120	120
Platform center of mass	m	-89.92	-91.1	-94.15
Platform mass	kg	7,466,330	7,281,600	7,316,578
Platform Roll Inertia	kg·m²	4,229,230,000	3,966,000,000	4,656,382,813
Platform Pitch Inertia	kg·m²	4,229,230,000	3,966,000,000	4,656,382,813
Platform Yaw Inertia	kg·m²	164,230,000	98,600,000	Not measured

* Jonkman and Musial (2010);** Koo et al. (2012);***Duan et al. (2015)

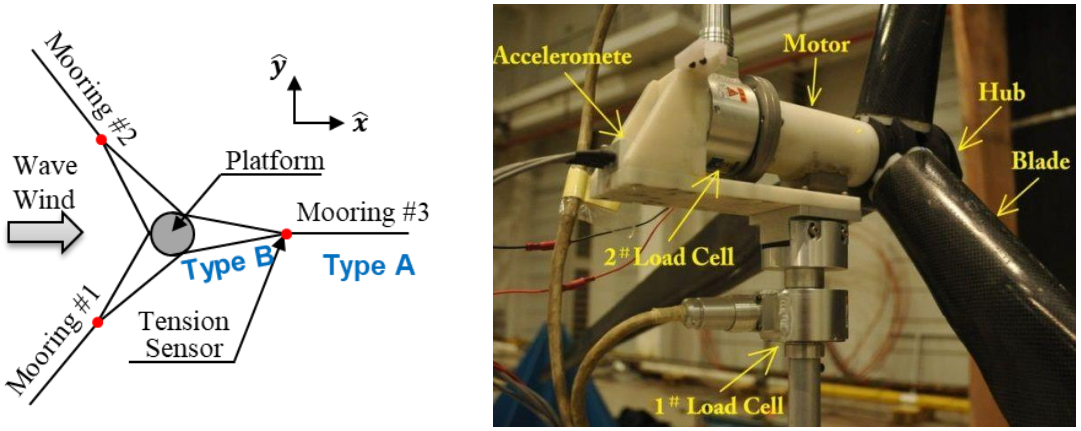

(a) (b)

Figure 14 Mooring Layout (a) and Assembled Devices (b); (b) is reprinted from Duan et al. (2015)

Table 3 Mooring System Properties; Reprinted from Duan et al. (2015)

Property		Unit	Value
Water depth		m	200
Anchor radius		m	445
Fairlead depth		m	70
Radius of fairlead		m	5.2
Number of mooring lines		EA	3 (Type A); 6 (Type B)
Angle between two mooring lines of type A		°	120
Pretension for type A		N	2,762,375
Un-stretched line length	Type A	m	424.35
	Type B	m	30
Diameter of mooring line	Type A	m	0.167
	Type B	m	0.125
Mass per unit length	Type A	kg/m	22.5
	Type B	kg/m	12.6
Axial stiffness (EA)	Type A	N	121,000,000
	Type B	N	68,000,000

4.2. Numerical Simulation Set-up and Calibration

4.2.1. Simulation Settings

In applying COUPLE-D-FAST, most conditions for the FOWT system were carefully maintained following the experimental conditions. The properties of the FOWT (the wind turbine and platform) and its mooring system followed the details listed in Table 1 to Table 3, respectively. The FOWT tower was considered to be a flexible body that allowed fore-after and side-to-side bending modes, while the blades were regarded as a rigid body. To calibrate COUPLE-D-FAST, several parameters were considered: mooring line stiffness, tower bending stiffness, platform added-mass and drag coefficients, platform yaw stiffness and damping, etc. Note that the calibration of the mooring stiffness will be presented in Section 5.1.

4.2.2. Hywind Platform Model

The platform shape of Hywind can be divided into three sections. The platform diameter above the taper of the platform was 6.5 m, and the diameter below the taper was 9.4 m. In this study, the platform was simplified as a combination of three cylinders with different diameters (as shown in Figure 15). In short, the taper section was simplified as a cylinder with a 7.95 m diameter, which is the diameter of the taper's midsection. The vertical forces acting on the taper section were estimated from the forces acting on a virtual plate located at the taper's midsection as shown in Figure 16. It should be noted that the vertical forces were applied only on the side of the plate faced up.

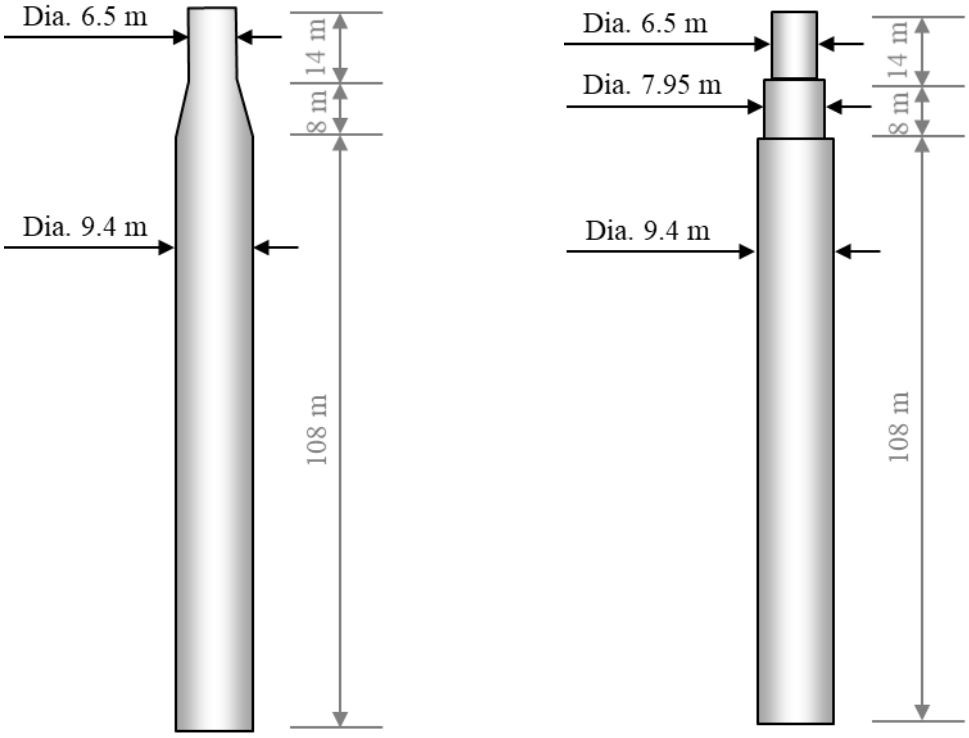

(a) Geometry in the model test (b) Geometry in the simulation

Figure 15 Geometry of Hywind Spar

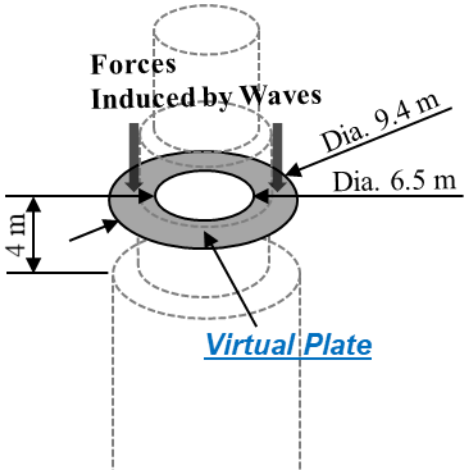

Figure 16 Taper Modeling in the Simulation

4.2.3. Hydrodynamic Coefficients for the Morison Equation

Since the shape of the Hywind platform was virtually cylindrical, its added mass coefficient was selected to be 0.97. In the time domain simulations, the nonlinear viscous drag forces were approximated using the Morison equation. Three cylindrical segments in the horizontal direction and two plates in the vertical direction were considered for the computation of the drag forces. Generally, the drag coefficient in the horizontal direction is chosen to be 0.6 for a cylindrical member. However, the Reynolds number could not be properly scaled down under the Froude similitude; for example, the maximum value of the Reynolds number was 12×10^6 in the prototype, but 34×10^3 in the model scale. Therefore, the drag coefficient was determined based on the model scale rather than the prototype. The drag coefficient in the horizontal direction was found to be 1.1, based on the Cd versus Re curve (Sarpkaya and Isaacson, 1981) and using corresponding Reynolds and Keulegan-Capenter (KC) numbers. The parameters for the drag coefficients are listed in Table 4. To match the damping effects in the heave direction, the vertical drag

coefficients of the taper section and bottom of the platform were chosen to be 0.35 and 3.0, respectively.

Table 4 Parameters for Estimation of Drag Coefficient

Wave Height (m)	Wave Period (sec)	Water Particle Velocity Amplitude (m/s)	Diameter at surface (m)	KC number	Reynolds number	
					Model	Prototype
2	8	0.79	6.5	0.97	14×10^3	5×10^6
4	10	1.26	6.5	1.93	23×10^3	8×10^6
7.1	12.1	1.84	6.5	3.43	34×10^3	12×10^6

4.2.4. Tower Stiffness Tests

The properties of the wind turbine tower used in the model test were different from those of the reference tower mentioned in the OC3 project, due to the measuring instruments installed in the tests. This led to different shapes and mass distributions compared to those of the OC3's reference tower. The tower used in the experiments was built from aluminum tubes with different diameters. The tower properties in the simulation needed to be calibrated to simulate the tower behavior. In the simulation, the tower was considered to be comprised of six cylindrical tubes with different diameters, and the tower's mass and center of gravity corresponded to the values used in the experiment.

The forces induced by the tower's flexibility were calculated via the linear modal analysis in the FAST module. The mode shapes for the fore-after and side-to-side were calculated using BMODES provided by NREL. The multiplier of the tower stiffness was considered to match the first fore-after mode frequencies for both the model test and

simulation. Then, the first mode frequencies were computed using a Fast Fourier Transform (FFT) of the accelerations of the nacelle; the values were 0.46 Hz in the model test and 0.47 Hz in the simulation.

4.3. Fixed Wind Turbine Test

Since the Hywind prototype was geometrically scaled down according to a Froude scale in the experiment, the viscous wind forces from winds could not be appropriately reproduced. If the wind speeds followed the Froude scale in the model test, the wind forces on the rotor of the wind turbine would be too small. Therefore, the discrepancy between the model and the prototype needed to be properly treated.

In the model tests, Duan et al. (2015) adjusted the wind speeds to obtain the targeted rotor thrust. The targeted rotor thrust was initially calculated by the FAST simulations under the conditions that the wind turbines were fixed to the ground as if they were the on-land wind turbines, and the blade pitch controller was operated with changes in wind speeds. It should be noted that the wind speeds in the FAST simulation were defined as “nominal,” which was different from the wind speeds in the model tests. The wind turbine in the model test was also mounted on a fixed base, and the wind speeds were adjusted to meet the targeted thrust forces. For cases of wind speeds exceeding 11.4 m/s (the rated wind speed), the testing wind speeds were lowered below the nominal wind speeds. This was because the blades were fixed on the hub in the model test, whereas the blades’ pitch angles in the FAST simulation were adjusted by the blade pitch controller. Table 5 shows a comparison of the results from the model tests with those of the FAST

simulations. The table shows that the measured mean thrust forces matched the thrust force predicted by FAST, but the related rotor speeds did not match.

Table 5 Fixed Wind Turbine Test Results; Reprinted from Duan et al. (2015)

Wind speed (m/s)		Thrust (kN)		Rotor speed (rpm)	
FAST	**Model**	**FAST**	**Model**	**FAST**	**Model**
5.0	9.4	276	276	7.5	7.9
11.4	12.8	770.4	770.4	12.1	14.4
18.0	11.1	451.1	451.1	12.1	10.9

5. INVESTIGATION OF HYWIND RESPONSES[1]

In this section, the capacities of COUPLE-D-FAST are examined through comparisons with the related results obtained, respectively, using COUPLE-FAST and FAST-OrcaFlex, and the measurements at the SJTU's wave basin. It should be noted that the reference point of the FOWT's global motion in the SJTU's tests was located at the mean water level before external forces were applied. To verify the mooring model in COUPLE-D-FAST, static offset tests were implemented to validate the mooring stiffness. The properties of Hywind, such as natural periods and damping effects, were then determined based on free-decay tests. Finally, the Hywind's global motion was investigated through wind-only load cases.

5.1. Mooring Stiffness Test

To verify the mooring model in COUPLE-D-FAST, the mooring forces from COUPLE-D-FAST were compared with those of COUPLE-FAST and FAST-OrcaFlex, and the SJTU's measurements. A simplified mooring system was used in COUPLE-FAST. However, the delta mooring system was employed for the other simulations. A multibody formulation was used to simulate the delta mooring system in FAST-OrcaFlex (i.e., each jointed node was altered by a massless buoy). Figure 17 shows the mooring layouts in the

[1] Part of this section is reprinted with permission from "Numerical Simulation of a Floating Offshore Wind Turbine Constrained by Delta Mooring System" by Min and Zhang (2017). Proceedings of the 27th (2017) International Offshore and Polar Engineering Conference, Copyright [2017] by the International Society of Offshore and Polar Engineers (ISOPE)

numerical simulations using the three different codes. Comparisons were made for the static offset tests and the shapes of the mooring lines.

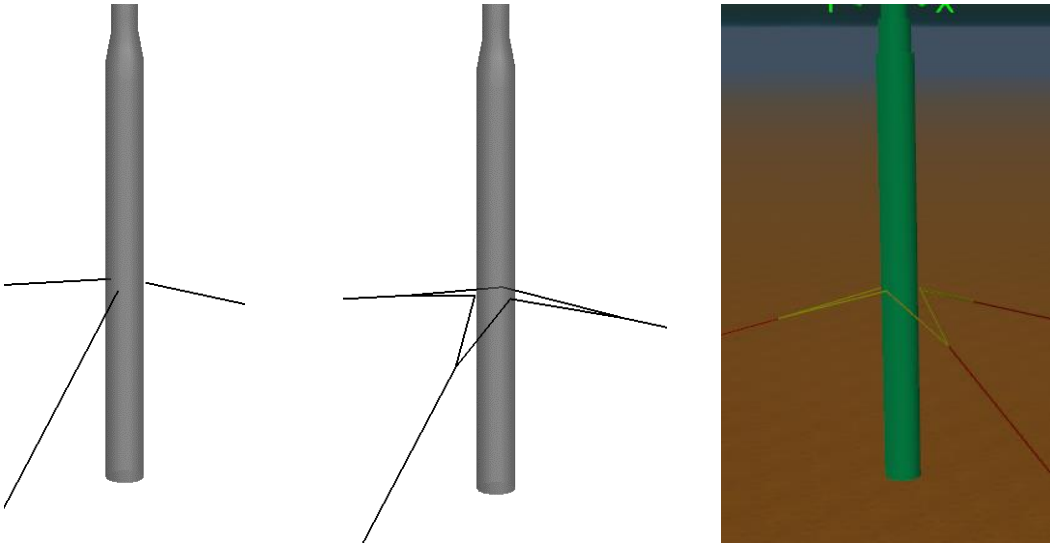

(a) COUPLE-FAST (b) COUPLE-D-FAST (c) FAST-OrcaFlex

Figure 17 Mooring Layouts in the Simulations

The horizontal offset tests were conducted within a surge or sway range of 0 to 6 m for the model tests, and within 0 to 10 m for the simulations. The results of the static offset tests from the model test and numerical simulations are plotted in Figure 18. Figure 18(a) and (b) show that the simulated stiffness curves for the surge and sway directions, respectively, agree well with the measurements. It should be noted that the available experimental results for the static offset test were limited only in the surge and sway directions. All simulated results for the heave direction were in good agreement, as shown in Figure 18(c). Because differences among the simulations were very small, they are indistinguishable in these figures. The yaw rotational offset test was implemented within a range of 0 to 10 degrees to examine the delta mooring model's yaw-stiffness capacity as

compared to the single mooring model. The yaw stiffness curve comparisons show very good agreement between the predictions by COUPLE-D-FAST and FAST-OrcaFlex (see Figure 18(d)). This clearly demonstrates that the developed mooring code in COUPLE-D-FAST properly captured the mooring forces of the delta mooring system. Moreover, it also shows that the delta mooring system significantly increased the yaw-restoring moments, as compared to the case of a simplified mooring system, although the effect of the delta mooring system was insignificant in the translational directions.

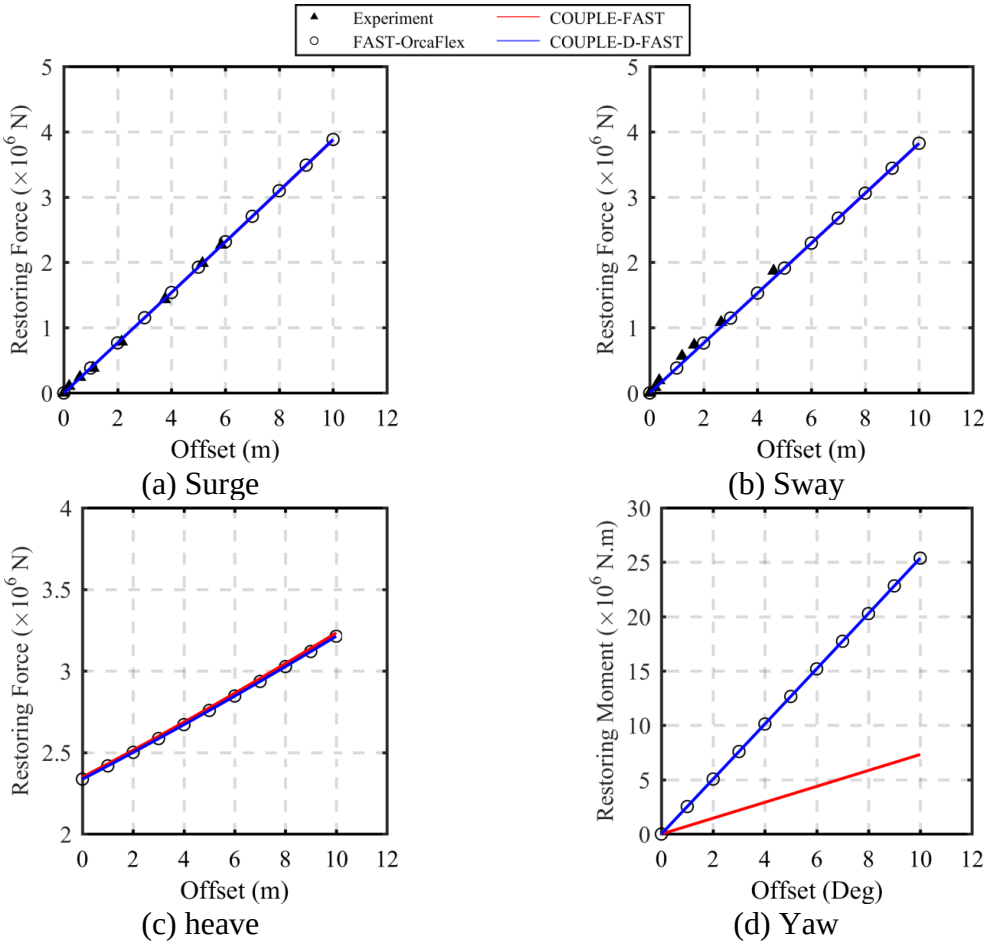

Figure 18 Static Offset Test Comparisons; (a) and (d) are reprinted with permission from Min and Zhang (2017)

Figure 19 depicts the mooring line configuration when the yaw angle was 10 degrees. The mooring lines' segments were almost identically shaped for both COUPLE-D-FAST and FAST-OrcaFlex, but COUPLE-FAST showed a different profile due to the simplification of the mooring system. This clearly indicates that the delta mooring system can substantially increase yaw stiffness, which is consistent with the comparison illustrated in Figure 18(d). This supports the superiority of the explicit simulation of delta mooring system, and also shows that it provides more realistic mooring behaviors.

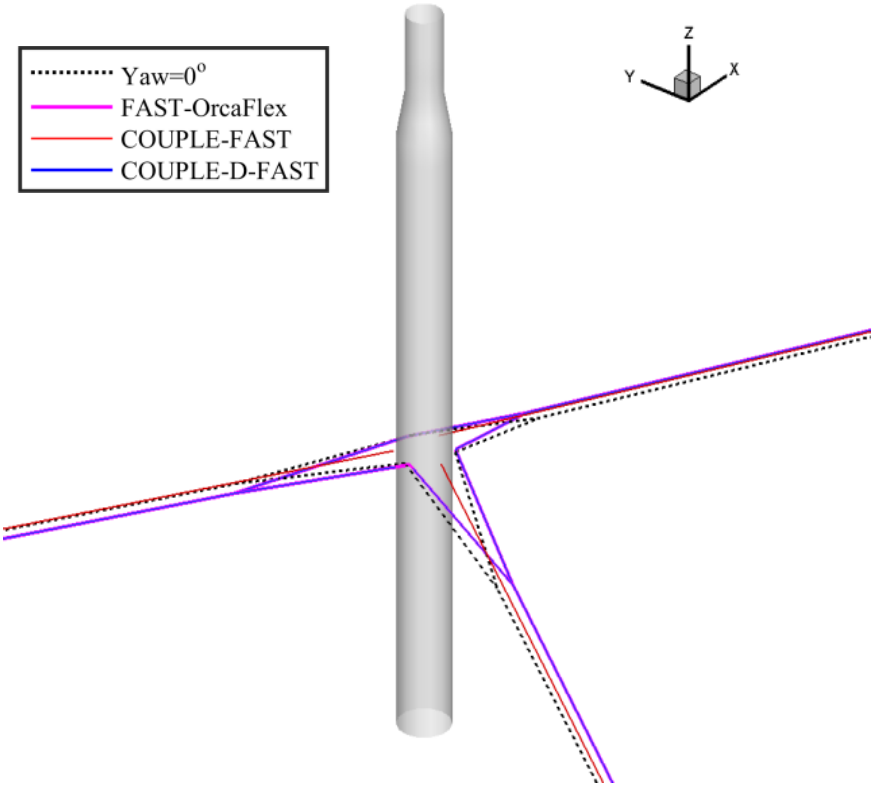

Figure 19 Configuration of Mooring Lines (Yaw=10°); Reprinted with permission from Min and Zhang (2017)

5.2. Free-decay Tests

5.2.1. Free-decay Tests without Tuned Parameters

Free-decay tests were carried out to determine the properties of Hywind such as natural periods and damping effects. The free-decay results are shown in Figure 20 and Figure 21 for the translational and rotational directions, respectively. It should be noted that additional tunings for better matching were not included in these Figures.

Overall, the simulated free-decay for surge, sway, and heave were in good agreement with the measurements, as shown in Figure 20. The surge motions of the floating structure were closely related to the restoring forces of its mooring system. Figure 20(a) indicates that the simulated results of all of the numerical models were in satisfactory agreement with the model test results, suggesting that the numerical codes were able to accurately simulate the restoring effects of the mooring system. In the heave free-decay tests, COUPLE-FAST and COUPLE-D-FAST rendered similar responses with the experiments, as shown in Figure 20(c), while FAST-OrcaFlex showed a slightly different natural period.

Figure 21 illustrates the free-decay results for rotational directions. In the roll and pitch decay tests plotted in Figure 21(a) and (b), respectively, the simulated natural periods rendered much smaller values than the measured ones. The reason for this phenomenon has not yet been identified. Additional tunings might be needed to match the decay results for the model test and simulations. The pitch decay test comparison indicated that Hywind was slightly under-damped compared to the model test after 50 sec. This may be because the installed cables in the model test (as shown in Figure 13) could have created a damping

effect on the FOWT system. In Figure 21(c), the yaw decay simulations considering the delta mooring system – COUPLE-D-FAST and FAST-OrcaFlex – were in excellent agreement with the experiment, but the simulated natural periods were slightly smaller than the measurement. This might be because the estimated yaw moment of inertia was slightly smaller than in the model test. It should be noted that he yaw moment of inertia was not measured in the model test. The yaw decay results from COUPLE-FAST clearly show that the natural period and damping effects could not be captured properly without explicit modeling. The following section describes the tunings of the platform properties that were made to obtain better agreement in the free-decay tests.

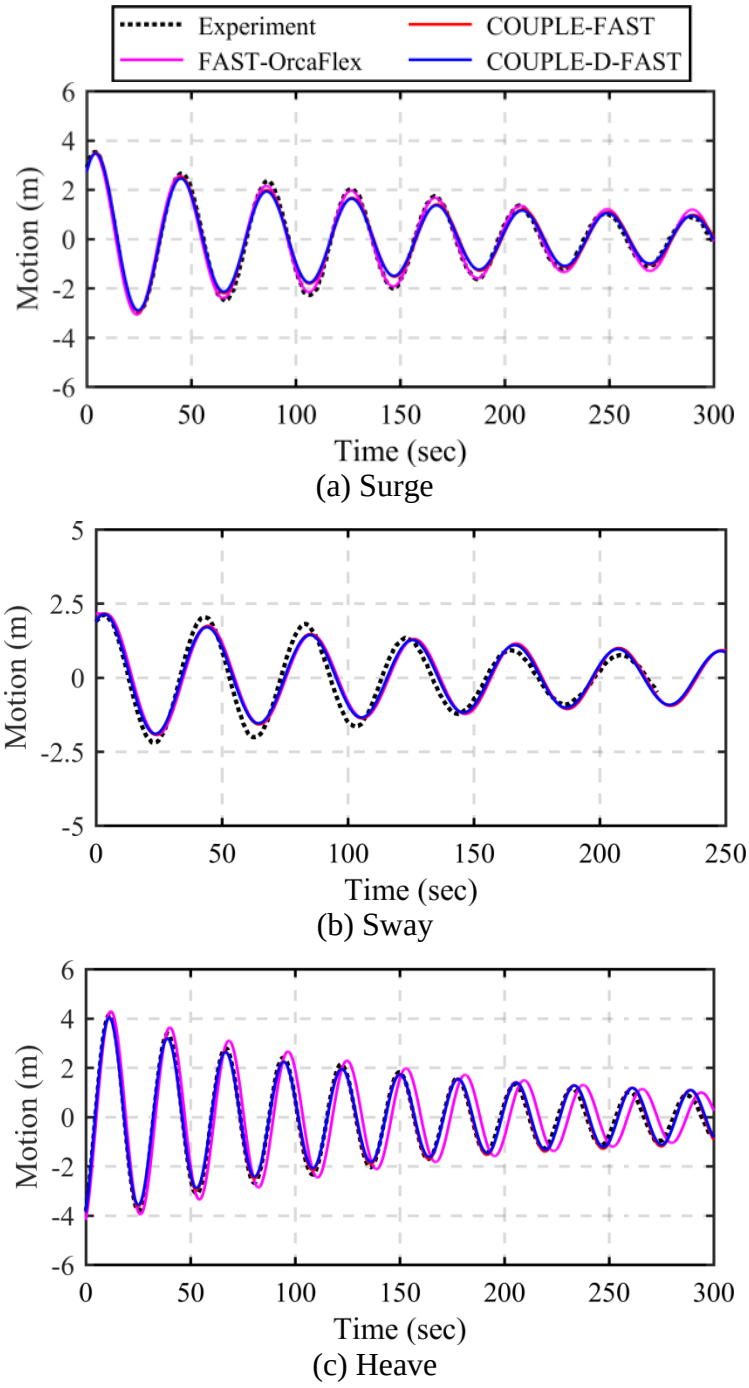

Figure 20 Free-decay Tests in Translational Directions (Un-tuned); (a) and (c) are reprinted with permission from Min and Zhang (2017)

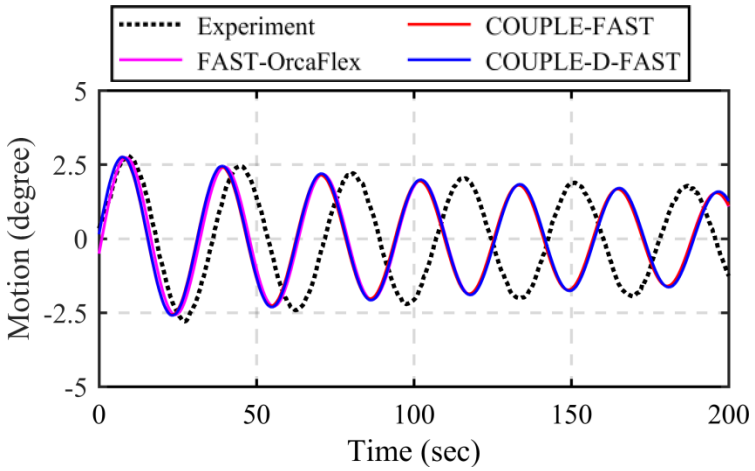

(a) Roll

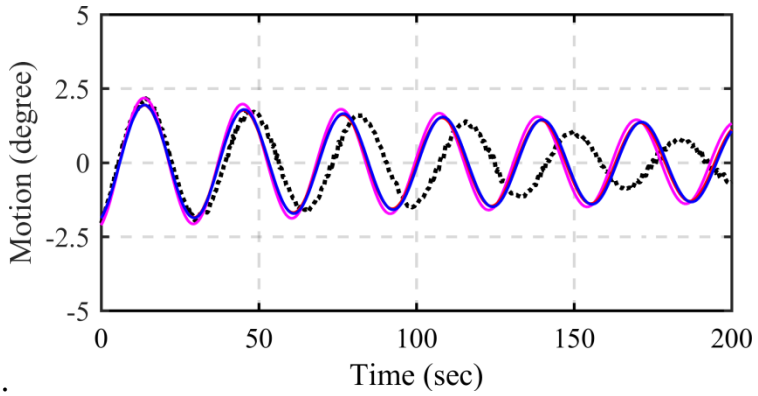

(b) Pitch

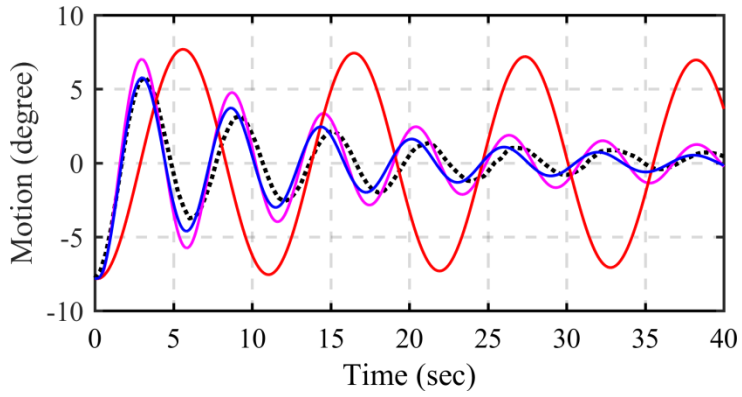

(c) Yaw

Figure 21 Free-decay Tests in Rotational Directions (Un-tuned); (c) is reprinted with permission from Min and Zhang (2017)

5.2.2. Free-decay Tests with Adjusted Parameters

The platform properties were adjusted based on a better agreement between the simulation results and the related rotational free-decay tests. The moments of inertia were adjusted by increasing 26% and 14% of the moments of inertia in the FOWT system's roll and pitch, respectively. For all simulations, the yaw moment of inertia for the Hywind platform was increased by 10%. The additional yaw damping and stiffness were set to 22 $\times 10^6$ N-m/(rad/s) and 108 $\times 10^6$ N-m/(rad), respectively, only for the COUPLE-FAST simulation. To include the cables' effects at the wind turbine tower, we considered a linear damper with a magnitude of 14 (kN/m/s), which was attached at the mid-section of the tower. The adjusted parameters are listed in Table 6.

Table 6 Adjusted Parameters of the FOWT System

Simulation model	Roll	Pitch	Yaw		
	Additional Moment of Inertia kg-m^2	Additional Moment of Inertia kg-m^2	Additional Moment of Inertia kg-m^2	Additional Damping N-m/(rad/s)	Additional Stiffness N-m/rad
FAST-OrcaFlex	91×10^8	49×10^8	10×10^6	-	-
COUPLE-FAST	91×10^8	49×10^8	10×10^6	22×10^6	108×10^6
COUPLE-D-FAST	91×10^8	49×10^8	10×10^6	-	-

Figure 22 shows the results of the free-decay tests for the rotational directions. Because the adjusted properties hardly affected the translational motion, the related figures

(surge, sway, and heave) were omitted for brevity. Using the adjusted parameters listed in Table 6, the simulated decays were in good agreement with the related measurement. In Figure 22(c), the measured and simulated yaw motions agreed well, but the FAST-OrcaFlex simulation showed relatively low damping effects while the COUPLE-D-FAST showed good agreement with the measurements. A comparison of the simulated and measured natural periods can be found in Table 7. Although the yaw natural period computed by COUPLE-FAST showed better agreement with the measurements than those obtained using the other codes, all predicted yaw natural periods were insignificantly different from the various models considered (within 0.2 sec).

Table 7 Natural Period of Hywind FOWT; Reprinted with permission from Min and Zhang (2017)

Case	Surge	Heave	Pitch	Yaw
Experiment	40.46	27.60	33.94	5.95
FAST-OrcaFlex	40.72	28.22	32.88	6.12
COUPLE-FAST	40.83	27.78	33.66	6.00
COUPLE-D-FAST	40.76	27.78	33.78	6.08

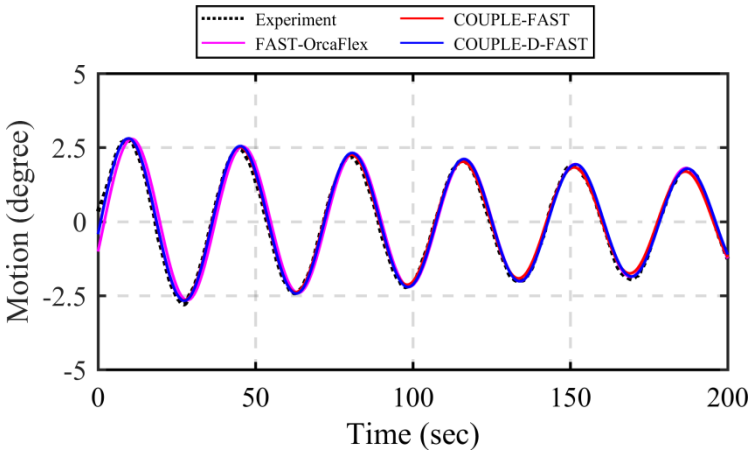

(a) Roll

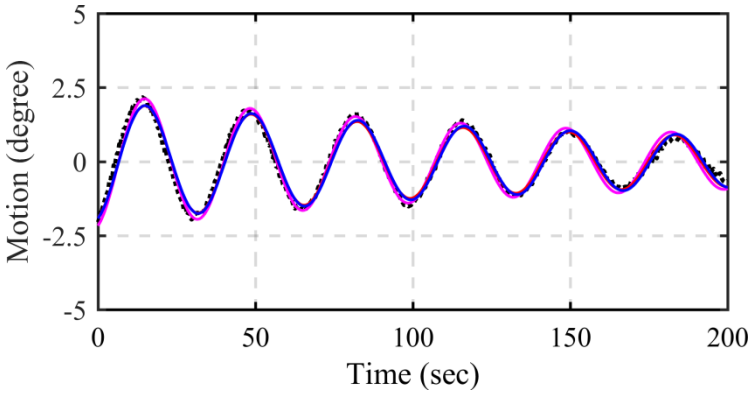

(b) Pitch

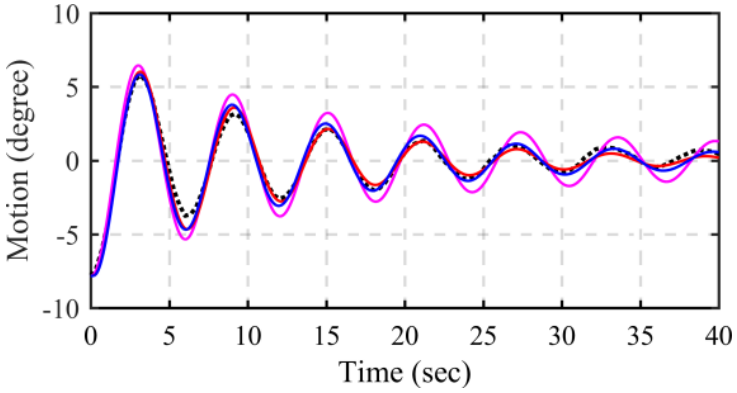

(c) Yaw

Figure 22 Free-decay Tests in Rotational Directions (Tuned); (c) is reprinted with permission from Min and Zhang (2017)

5.3. Corrections of Wind Speeds

Due to a misunderstanding of the coordinate system for the wind thrust between the experiment and the FAST simulation, the wind speeds in the model test based on the fixed wind turbine test in Table 5 were overestimated and need to be corrected accordingly. In the experimental setting, the rotor shaft axis was parallel to the horizontal direction of the global coordinate system (as shown in Figure 23(a)). Therefore, the measured thrust forces were caused solely by the wind thrust. However, as shown in Figure 23(b), the shaft in the FAST simulation was tilted by -5 degrees, which is the default setting of the NREL's 5MW reference wind turbine (Jonkman et al., 2009). This indicates that the simulated thrust forces included a portion of the rotor weight, in addition to the wind thrust. The rotor weight's portion of the thrust force was approximately 94 kN (= 9.81 × 109.9 × sin(5°)) in the simulation. For example, in the case of 5 m/s winds (see Table 5), the measured wind force was 51% larger than the simulated wind force.

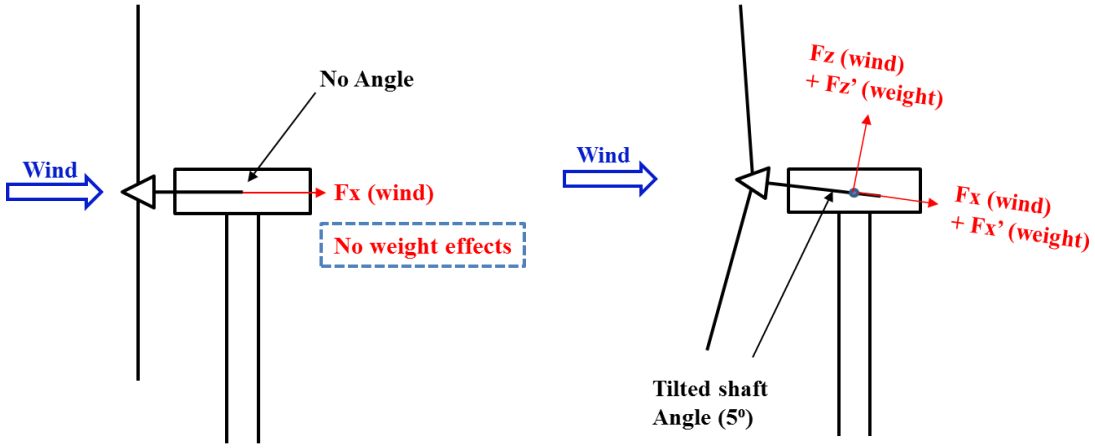

(a) Experiment (b) Simulation

Figure 23 Initial Settings of Rotor in SJTU's Study; Reprinted with permission from Min and Zhang (2017)

When the simulation used the nominal wind speed given by Duan et al. (2015), the overestimated wind conditions led to a significant discrepancy in the motion of the FOWT between the model test and the simulation, specifically in the mean surge and pitch motions (Min et al., 2016). Therefore, the nominal wind speeds needed to be corrected based upon the settings used in the experiment, instead of the default setting (as in the NREL case). Hence, the shaft tilt and pre-cone angles were explicitly set to be 0 degrees in running FAST, consistent with the settings for the model test. With the corrected settings, the nominal wind speeds were redefined to proper values through the FAST simulations. Since the blade pitch control was not included in the experiment, the control system was also not included in the FAST simulation. Without the pitch controller, the blade pitch angles in the simulation were chosen to be the angles corresponding with the selected wind speeds. Table 8 shows a comparison of the results from the model tests with those of the FAST simulations. The simulated thrust forces under the corrected wind speeds were well matched with the corresponding measurements. The first two wind conditions in Table 8 are named Operational conditions 1 and 2, and the final wind condition is called the Extreme condition in this research.

Table 8 Redefined Wind Speed; Reprinted with permission from Min and Zhang (2017)

	Wind speed (m/s)		**Rotor thrust (kN)**		**Rotor speed (rpm)**		**Blade pitch (°)**	
	FAST	**Model**	**FAST**	**Model**	**FAST**	**Model**	**FAST**	**Model**
I	6.55	9.4	275.3	276	8.24	7.9	0	0
II	14.30	11.1	451.0	451.1	12.10	10.9	9.28	0
III	11.41	12.8	770.0	770.4	12.57	14.4	0	0

I: Operational condition 1; II: Operational condition 2; III: Extreme condition

5.4. Motions of Hywind under Steady Wind Loads

To investigate the effects of wind loads on Hywind, three different nominal wind speeds of 6.55 (Operational 1), 14.30 (Operational 2) and 11.41 (Extreme) m/s at the hub height were used in the numerical simulations using COUPLE-FAST, COUPLE-D-FAST, and FAST-OrcaFlex for one-half hour. The average platform motion and mooring tension for the upstream (U) and downstream (D) sides were compared with the measurements in Table 9. Under steady winds, the dynamic motions and forces were very small, so their comparisons were omitted. It should be noted that the FOWT's average surge and heave motions were at the mean water level. The average motions and forces from the COUPLE-FAST and COUPLE-D-FAST simulations rendered very similar responses, indicating that the delta mooring system had less impact on the FOWT's motions, except with yaw motions. However, the direct modeling of the delta mooring system has an advantage in that additional tuning of the yaw stiffness and damping was not needed. Interestingly, the FAST-OrcaFlex simulation showed slightly larger discrepancies in the platform motions in comparison with the other two simulations. This discrepancy may have resulted from differences in the modeling approach.

Even though corrected wind speeds were used in the simulations, the predicted pitch motions were still smaller than the measured values, as indicated in Table 9. However, it should be noted that they were greatly improved compared to the results of our previous study (Min et al., 2016), as listed in Table 10. Figure 24 offers a visual comparison of the results obtained from the previous results of Min et al. (2016), the present results from COUPLE-D-FAST and FAST-OrcaFlex, and the model test.

Despite discrepancies in platform motions between the simulations and the model test, the predicted mooring loads showed excellent agreement with the measurements. This is because the fairleads of the mooring lines were located near the center of mass of the FOWT system, indicating that the displacements of the fairleads were less influenced by the platform's pitch motion, while the surge motions at the mean water level were strongly affected by the pitch motions.

Table 9 Average Behaviors of Hywind by Steady Wind Impact; Reprinted with permission from Min and Zhang (2017)

Wind condition	Parameter	C-F	C-D-F	F-O	EXP
Operational 1 (6.55 m/s)	Surge (m)	2.92	2.97	2.82	3.17
	Heave (m)	-0.06	-0.03	-0.02	-0.06
	Pitch (°)	1.85	1.87	1.74	2.21
	Mooring tension (U) (kN)	2853	2856	2855	2855
	Mooring tension (D) (kN)	2576	2578	2578	2597
Operational 2 (14.30 m/s)	Surge (m)	4.80	4.87	4.66	6.03
	Heave (m)	-0.11	-0.08	-0.07	0.04
	Pitch (°)	3.04	3.06	2.89	4.26
	Mooring tension (U) (kN)	2914	2916	2916	2956
	Mooring tension (D) (kN)	2460	2461	2462	2464
Extreme (11.41 m/s)	Surge (m)	8.04	8.16	7.89	8.69
	Heave (m)	-0.27	-0.24	-0.22	-0.30
	Pitch (°)	5.08	5.12	4.91	6.01
	Mooring tension (U) (kN)	3023	3026	3022	3027
	Mooring tension (D) (kN)	2257	2257	2261	2318

C-F: COUPLE-FAST; C-D-F: COUPLE-D-FAST; F-O: FAST-OrcaFlex; EXP: Experiment

Table 10 Average Behaviors of Hywind by Steady Wind Impact; Reprinted from Min et al. (2016)

Parameter	Wind condition		
	Operational 1 (5 m/s)	Operational 2 (18.0 m/s)	Extreme (11.4 m/s)
Surge (m)	1.88	3.78	7.47
Heave (m)	-0.01	-0.04	-0.20
Pitch (°)	1.19	2.40	4.73
Mooring tension (U) (kN)	2822	2883	3003
Mooring tension (D) (kN)	2644	2527	2297

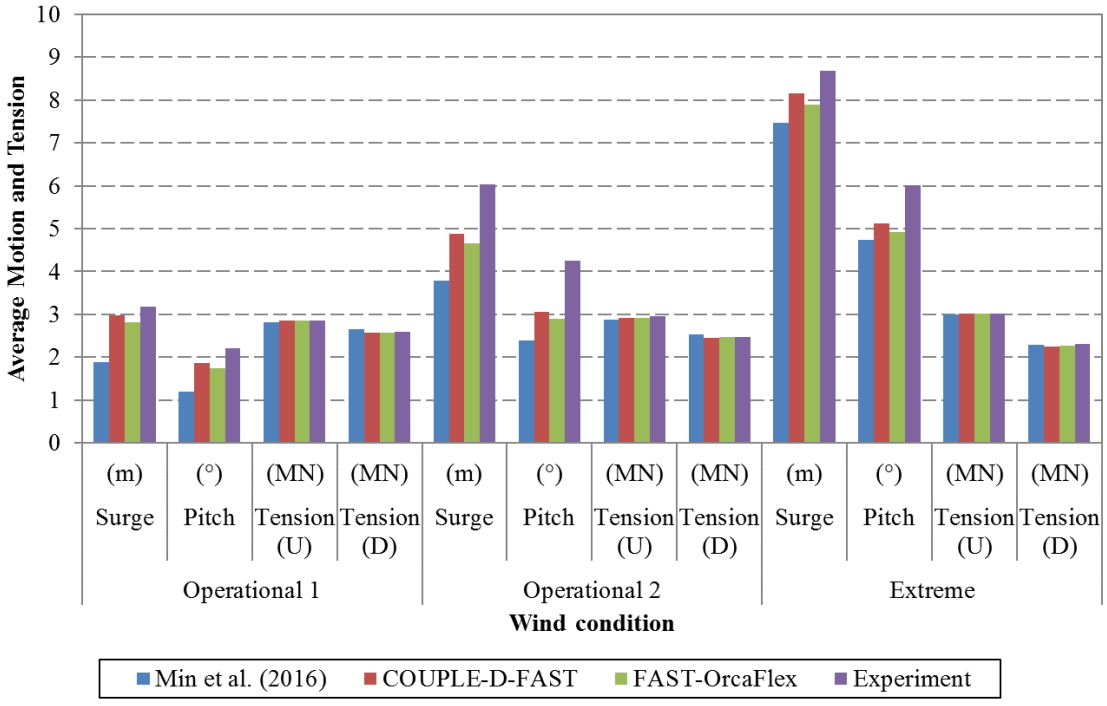

Figure 24 Average Platform Motions and Mooring Tensions

5.5. Discussion

In this section, COUPLE-D-FAST's capability for modeling the delta mooring system was examined through static offset and free-decay tests, and steady wind impact-only tests. Corrections of wind speeds were made prior to simulating the wind impact-only cases, because the tested wind speeds were initially overestimated as mentioned in Section 5.3. The delta mooring system was directly modeled in COUPLE-D-FAST and FAST-OrcaFlex, while COUPLE-FAST used a simplified model for the mooring system. The model test and all simulations were in satisfactory agreement with regards to mooring stiffness in surge and sway. In terms of yaw stiffness, COUPLE-D-FAST and FAST-OrcaFlex showed similar mooring stiffness values that were much greater than those predicted by COUPLE-FAST.

In the yaw decay tests, the motions obtained using COUPLE-D-FAST and FAST-OrcaFlex showed good agreement with the related measurements, indicating the superiority of direct modeling of the delta mooring system. In terms of roll and pitch, however, the simulated natural periods were smaller than the measured ones. This led to case-specific increases in the moments of inertia in those directions, so that the computed free-decay motions agreed well with the measurements. However, the increases (26% in roll and 14% in pitch) might not be negligible tuning but be regarded as unrealistic tuning. In addition, the simulated mean motions rendered smaller values than the measurements, even though the wind speeds were corrected in Section 5.3. The discrepancies of the free-decay tests and the mean FOWT motions are further investigated in the next section.

6. INVESTIGATION OF HYWIND RESPONSES WITH CORRECTED CENTER OF GRAVITY

Although the corrected wind speeds were used in COUPLE-D-FAST and FAST-OrcaFlex (see Section 5.4), the improvements were not enough to yield satisfactory agreement with the related measurements of the global motions. To understand the source or reasons for the discrepancies between the simulations and related measurements, we firstly focused on the comparison of the mean global motion of the FOWT. The simulated results from COUPLE-D-FAST are compared with those of the SJTU's model test under various environmental conditions.

Eleven cases were used in the comparison include wind impact-only, irregular wave impact-only, wind with regular waves, and wind with irregular waves. The comparisons involve global platform motions and mooring tensions in both time and frequency domains. Prior to applying the various met-ocean conditions, the FOWT's center of gravity was corrected through simulations using measured wind forces, and free-decay tests were then implemented to examine the effects of this correction.

6.1. Environmental Conditions

6.1.1. Turbulent Wind Conditions

While the application of steady wind conditions was described in Section 5.3, turbulent wind conditions were applied at this stage of the research to make the simulated winds more similar to those used in the model tests. Similar to the results given in Section

5.3, the redefined nominal wind speeds based on the fixed wind turbine tests but under the impact of the turbulence winds are given in Table 11. While the nominal wind speeds of Operational 1 and Extreme conditions remain the same as compared to the corresponding wind speeds in Section 5.3, the wind speeds of Operational condition 2 were lowered to keep the consistency of the model test condition that the blade pitch rotation was not allowed.

Because the time series of wind speeds from the model tests were not available, the turbulence intensities for Operational 1, Operational 2, and Extreme conditions were chosen to be 5%, 3%, and 2%, respectively, and the turbulent winds for the simulations were generated using the TurbSim program (Jonkman, 2009). The turbulence intensities were selected based on the spectral analysis for surge and pitch motions under the wind load only conditions. Figures 25 to 27 show comparisons of surge and pitch spectrum obtained using COUPLE-D-FAST under the steady and turbulent wind conditions and the model test. As shown in these figures, the simulated surge and pitch under turbulence wind conditions show good agreement with the corresponding measurements while dynamic responses are barely observable in the simulations under steady wind conditions.

Table 11 Wind Speeds

	Wind speed (m/s)		**Rotor thrust (kN)**		**Rotor speed (rpm)**		**Blade angle (°)**	
	FAST	**Model**	**FAST**	**Model**	**FAST**	**Model**	**FAST**	**Model**
I	6.55	9.4	275.6	276	8.2	7.9	0	0
II	8.62	11.1	451.3	451.1	9.9	10.9	0	0
III	11.41	12.8	770.2	770.4	12.6	14.4	0	0

I: Operational condition 1; II: Operational condition 2; III: Extreme condition

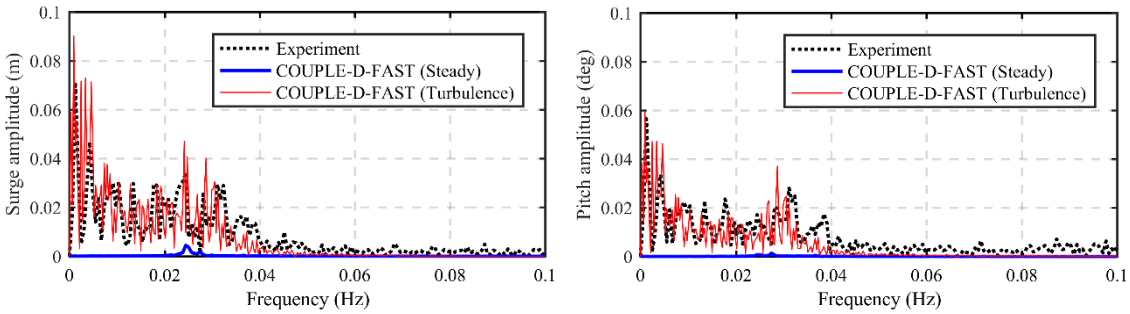

(a) Surge (b) Pitch

Figure 25 Comparison of Surge and Pitch Amplitude Spectrum (Operational 1)

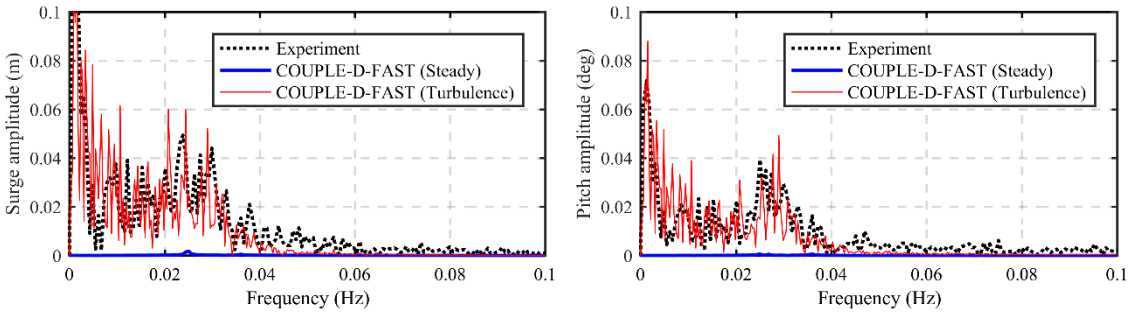

(a) Surge (b) Pitch

Figure 26 Comparison of Surge and Pitch Amplitude Spectrum (Operational 2)

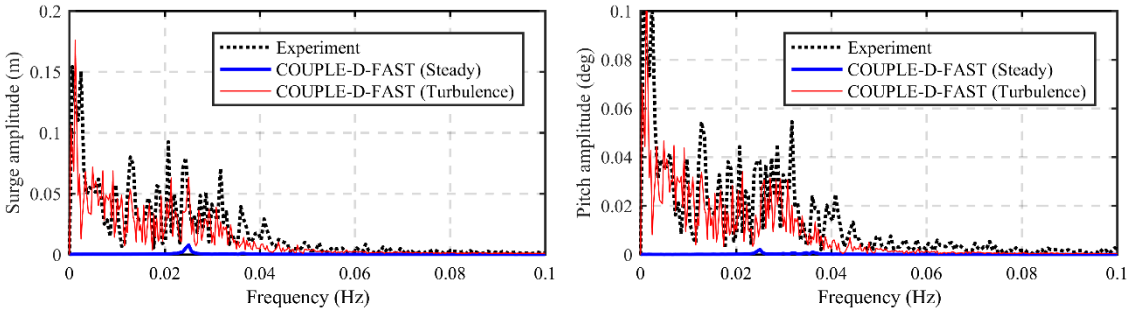

(a) Surge (b) Pitch

Figure 27 Comparison of Surge and Pitch Amplitude Spectrum (Extreme)

6.1.2. Met-ocean Conditions

Eleven different cases were simulated in this study. They can be divided into four sets: wind load-only (LC01-LC03), wave load-only (LC04 and LC05), combined wind and regular wave loads (LC06-LC08), and combined wind and irregular wave loads

(LC09-LC11). The Joint North Sea Wave Project (JONSWAP) spectrum was employed to generate irregular waves in both the model test and simulation. The wave conditions in LC05, LC10, and LC11 represented one year return period in the Gulf of Maine (Koo et al., 2012). To prevent sudden "jerk" movements of the FOWT at the beginning, a 100 seconds sine-function ramp function was applied on the simulated external forces at the beginning. The met-ocean conditions for all of the cases are summarized in Table 12.

Table 12 Environmental Conditions

CASE		Wind speeds (m/s)		Waves
		Model	Simulation	
Wind only	LC01	9.4	6.55	-
	LC02	11.1	8.62	-
	LC03	12.8	11.41	-
Irregular waves only	LC04	-	-	2 m / 8 sec (γ = 3.3)
	LC05	-	-	7.1 m / 12.1 sec (γ = 2.2)
Winds + Regular waves	LC06	9.4	6.55	2 m / 8 sec
	LC07	11.1	8.62	6 m / 11 sec
	LC08	12.8	11.41	4 m / 10 sec
Winds + Irregular waves	LC09	9.4	6.55	2 m / 8 sec (γ = 3.3)
	LC10	11.1	8.62	7.1 m / 12.1 sec (γ = 2.2)
	LC11	12.8	11.41	7.1 m / 12.1 sec (γ = 2.2)

6.2. Correction of the Center of Gravity

6.2.1. Simulation using Measured Wind Forces

After the corrections to the nominal wind speeds were made, the simulated average surge and pitch are still smaller than the corresponding measurements listed in Section 5.4. To investigate these discrepancies, we conducted simulations directly using the measured wind loads instead of using FAST's predictions.

The measurements at Load Cell #1 (see Figure 14(b)) were chosen instead of those of Load Cell #2 because the mass property of the motor in the nacelle was not specified in the model test. Considering that Load Cell #1 was moving and rotating with respect to the FOWT's movement, the loads should have been transformed to the reference frame: $\hat{o}\hat{x}\hat{y}\hat{z}$ (space-fixed) for translational directions and *oxyz* (body-fixed) for rotational directions. Since the measured wind load is directly applied in the simulation (instead of the FAST computation), the motion equation (Eq. 3.10) is written as:

$$\left[\mathbf{M}_{\mathrm{s}}+\mathbf{M}_{\mathrm{a}}\right]\ddot{x}(t)+\mathbf{C}\,x(t)=\mathbf{F}_{mean}+\mathbf{F}_{current}+\mathbf{F}_{MR}+\mathbf{F}_{HSn}+\mathbf{F}_{M}+\mathbf{F}_{EXP} \tag{4.1}$$

$$\mathbf{F}_{EXP}=\left\{\begin{array}{l}\mathbf{T}^{t}\mathbf{F}_{measured}-\hat{\mathbf{F}}_{TOP}\\ \mathbf{M}_{measured}+\mathbf{r}_{TOP}\times(\mathbf{F}_{measured}-\mathbf{T}\hat{\mathbf{F}}_{TOP})\end{array}\right\} \tag{4.2}$$

where, $\mathbf{F}_{EXP}$ is the measured wind forces at Load Cell #1 after the exclusion of inertia force and moment, $\hat{\mathbf{F}}_{TOP}$ represents the inertial forces above Load Cell #1 in $\hat{o}\hat{x}\hat{y}\hat{z}$, $\mathbf{F}_{measured}$ and $\mathbf{M}_{measured}$ are the measured forces and moments, respectively, at Load Cell #1, and $\mathbf{r}_{TOP}$ is the location of Load Cell #1 in the *oxyz* coordinates. The mass above Load Cell #1 was estimated to be 449.013 tons, which included the upper parts of the wind turbine tower. Then, the weight effects induced by the pitch motions were subtracted from the measured forces. Nine cases were simulated using this approach, and the results are listed in Table 13. Figure 28 shows the average surge and pitch motions predicted using this approach and their comparisons with the measured values. Overall, the predicted average

surge and pitch are still smaller than the corresponding measurements. The under-predictions of mean surge may be likely caused by the smaller average pitch, because the mean surge is compared at the mean water level, not at the center of gravity of the system.

Table 13 Environmental Conditions for Simulations using Measured Wind Forces

Wind condition	Mean wind forces at the load cell #1 (in model test)	Wave condition	
		Type	H // T or Hs // Tp
Operational 1	281.5 kN	-	-
	282.3 kN	Regular waves	2 m // 8 sec
	268.3 kN	Irregular waves	2 m // 8 sec
Operational 2	506.8 kN	-	-
	481.5 kN	Regular waves	6 m // 11 sec
	445.1 kN	Irregular waves	7.1 m // 12.1 sec
Extreme	757.2 kN	-	-
	685.1 kN	Regular waves	4 m // 10 sec
	698.0 kN	Irregular waves	7.1 m // 12.1 sec

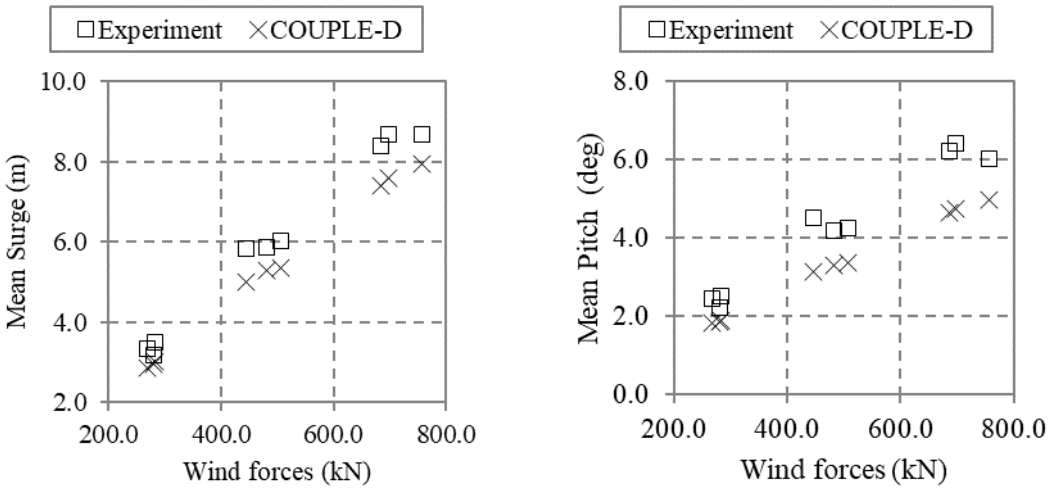

(a) Surge (b) Pitch

Figure 28 Average Platform Motions using Measured Wind Forces

6.2.2. Correction of the Center of Gravity

Wind forces are one of the dominant factors affecting the mean surge and pitch of the FOWT. After measured wind forces were used as input in the simulation, we attempted to find which other factors were responsible for the smaller predicted average pitch. The other important factors determining mean surge and pitch include the FOWT system's mooring line restoring force and hydrostatic stiffness. Because the surge stiffness from the model test and the simulation were in relatively satisfactory agreement (as shown in Figure 18(a)), the main reason for the small pitch motions is likely caused by the hydrostatic stiffness, which was dominated by the distance between the centers of buoyancy (CB) and the center of gravity (CG) of the FOWT.

In the experiment, the spar platform's CG could be inaccurate because there were uncertainties such as the location of the metal ballast in the spar and the spar's complicated inner space. This led to a reconsideration of the location of the FOWT's CG, which is closely related to the pitch stiffness of the floating system. The CG for the total system was estimated to be -76.267 m, while the CG given by the model test was -78.947 m.

The pitch moment of inertia and the FOWT system's stiffness were re-estimated based on the corrected CG, and they were then compared to the corresponding calculations based on the given CG as listed in Table 14. As shown in this table, the stiffness by hydrostatic and mooring system decreased largely (-16%) after applying the correction of CG although the change regarding the pitch moment of inertia was relatively insignificant (-4%). It should be noted that the additional tunings for the pitch moment of inertia are not included in this estimation. Figure 29 shows pitch free-decay comparisons of two

simulated results (based on the given and corrected CG, respectively) with the measurements. When the given CG was used in the simulation, the free-decay test rendered a smaller pitch natural period than the measurement, as shown in Figure 29 (blue line), so that it may require additional tunings to match the natural period. However, the corrected CG allowed the FOWT's pitch natural frequency agrees well with the corresponding measurement without tunings on the FOWT's moment of inertia, as shown in Figure 29 (red line).

Table 14 Pitch Moment of Inertia and Stiffness Comparison

Property	Item	Unit	CG Condition	
			Given	Corrected
CG	FOWT CG	m	-78.947	-76.267
Moment of Inertia	Blades	$\times 10^6$ kg-m^2	1,535	1,488
	Hub	$\times 10^6$ kg-m^2	1,649	1,597
	Nacelle	$\times 10^6$ kg-m^2	6,878	6,662
	Tower	$\times 10^6$ kg-m^2	7,017	6,741
	Spar Platform	$\times 10^6$ kg-m^2	6,347	6,350
	Added Mass	$\times 10^6$ kg-m^2	11,263	10,599
	Total (Error)	$\times 10^6$ kg-m^2	34,690	33,438 (-4%)
Stiffness	Hydrostatic	$\times 10^6$ N-m^2/rad	1,363	1,147
	Mooring	$\times 10^6$ N-m^2/rad	30	19
	Total (Error)	$\times 10^6$ N-m^2/rad	1,393	1,166 (-16%)

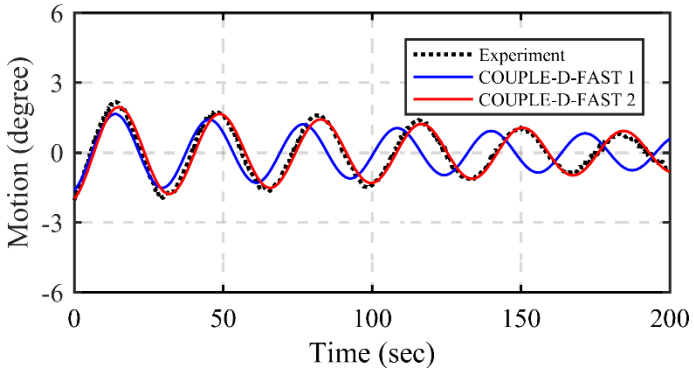

Figure 29 Pitch Decay Results with the Given (blue) and Corrected (red) CG

All cases in Table 13 were re-simulated using the corrected CG and measured wind forces. The results are compared with the corresponding measurements in Figure 30. The average surge of the measurements and simulations were in satisfactory agreement as shown in Figure 30(a). Figure 30(b) indicates that the pitch motions in the simulation were slightly different from those in the measurement, but the results are a significant improvement over those in Figure 28(b). These discrepancies may have resulted from experimental errors in that the mean pitch angles in the measurement did not continuously increase as the wind forces increased.

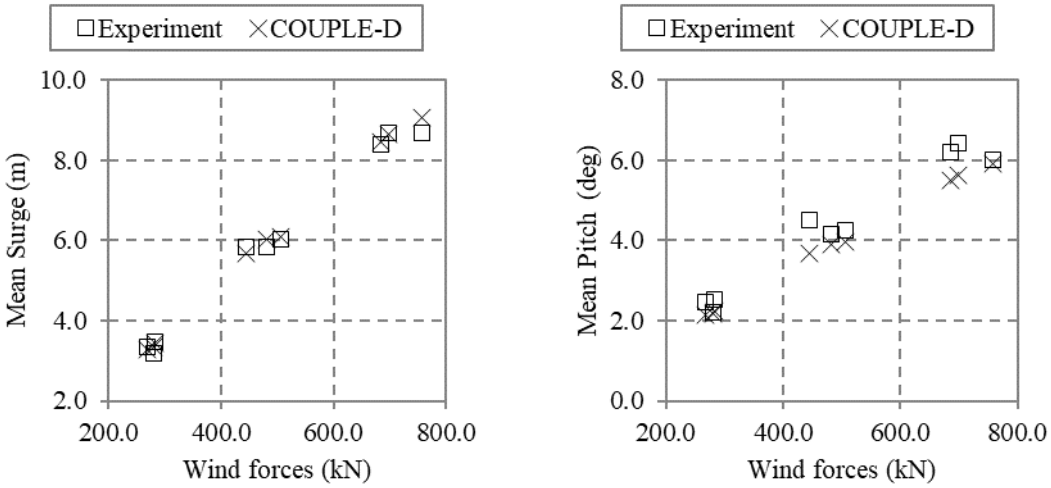

(a) Surge (b) Pitch

Figure 30 Average Platform Motions using Measured Wind Forces with the Corrected CG

6.3. Free-decay Tests

The corrected center of gravity could have changed the Hywind's natural frequency because it results in a change in the hydrostatic stiffness. With the corrected center of gravity, the Hywind's natural periods and damping were investigated again through the related free-decay tests.

Since the change to the center of gravity hardly affected the free-decay of the translational motion, the related free-decay comparisons have been omitted for brevity. Additional fine tuning was done to produce better agreement between the simulation and model tests. The tuned parameters are listed in Table 15. In the roll decay test, the roll moments of inertia were increased by 10% over the total roll moments of inertia in the simulations. A linear damper with a magnitude of 14 (kN/m/s) was considered so as to include the cables' effects at the mid-point of the wind turbine tower. Figure 31 shows the results of the free-decay tests for rotational directions. As shown in this figure, the free-decay simulations were in satisfactory agreement with the measurement although a small surge natural period in FAST-OrcaFlex was rendered. The simulated and measured natural periods are compared in Table 16.

Table 15 Additional Tuning of the FOWT System

Case	Roll	Pitch	Yaw		
	Additional Moment of Inertia kg-m^2	Additional Moment of Inertia kg-m^2	Additional Moment of Inertia kg-m^2	Additional Damping N-m/(rad/s)	Additional Stiffness N-m/rad
FAST-OrcaFlex	33×10^8	-	10×10^6	-	-
COUPLE-FAST	33×10^8	-	10×10^6	22×10^6	108×10^6
COUPLE-D-FAST	33×10^8	-	10×10^6	-	-

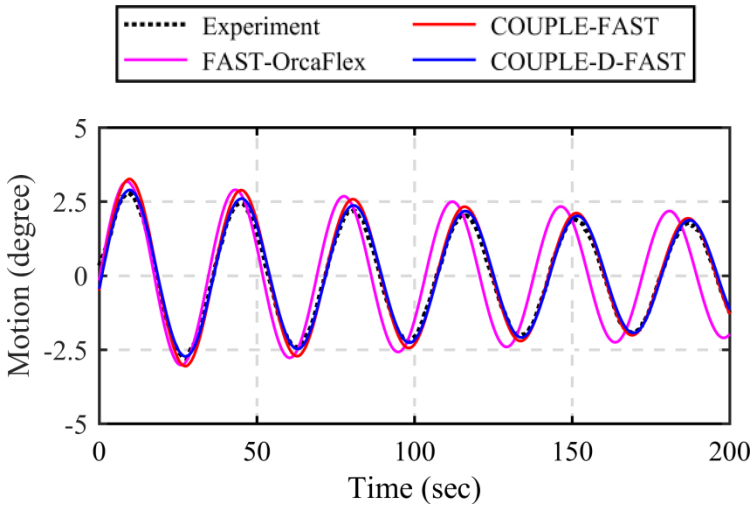

(a) Roll

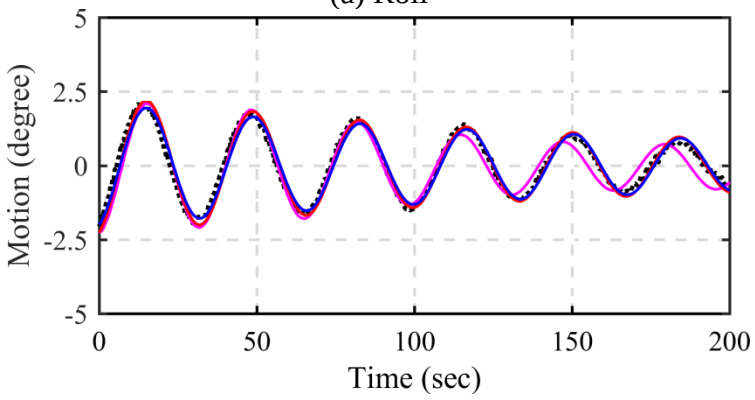

(b) Pitch

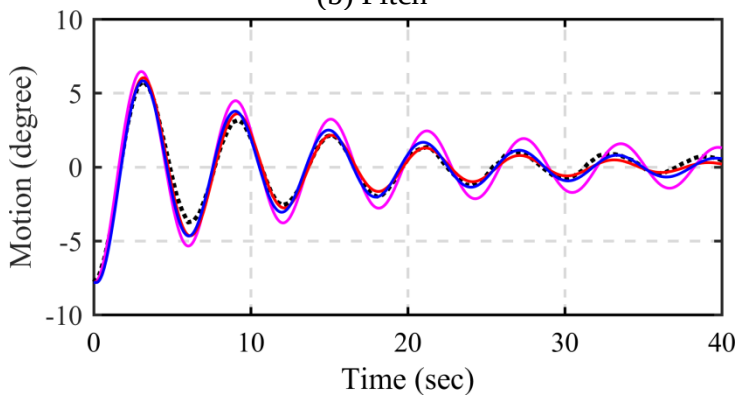

(c) Yaw

Figure 31 Free-decay Tests in Rotational Directions (Tuned)

Table 16 Natural Period of the Hywind System (Unit: sec)

Case	Surge	Sway	Heave	Roll	Pitch	Yaw
Experiment	40.46	40.94	27.60	35.60	33.94	5.95
FAST-OrcaFlex	40.73	40.85	28.12	34.40	32.98	6.12
COUPLE-FAST	40.77	40.80	27.78	35.49	33.80	6.00
COUPLE-D-FAST	40.74	40.80	27.78	35.49	33.88	6.08

The simulated and measured mooring tensions at the two fairleads and joints of each mooring line were also compared. The layout of the mooring system and mooring line index numbers are given in Figure 32. For the yaw decay test, Figure 33 and Figure 34 show comparisons of the downstream- and upstream-side mooring line tensions for COUPLE-D-FAST and FAST-OrcaFlex, respectively. Note that the mooring line tensions were not recorded in the measurements for free-decay tests. Figure 33(a) and (b) include a comparison of the mooring tensions at the fairleads on the downstream-side (Tensions 3-1 and 3-2), which could not be computed when a simplified mooring system was used such as in the COUPLE-FAST simulation. Both the COUPLE-D-FAST and FAST-OrcaFlex simulations rendered very similar responses. With regards to the tensions at the delta mooring joint, while the simulated results showed similar responses in the initial stage (0 to 10 seconds) during the yaw decay test, they rendered somewhat different oscillations after that stage. For the upstream side illustrated in Figure 34, the overall simulated results from both numerical models were in satisfactory agreement at the fairleads tensions, but some differences were observed in the case of the tensions at the delta joint (as shown in Figure 34(c)) after 10 seconds at the downstream-side mooring line.

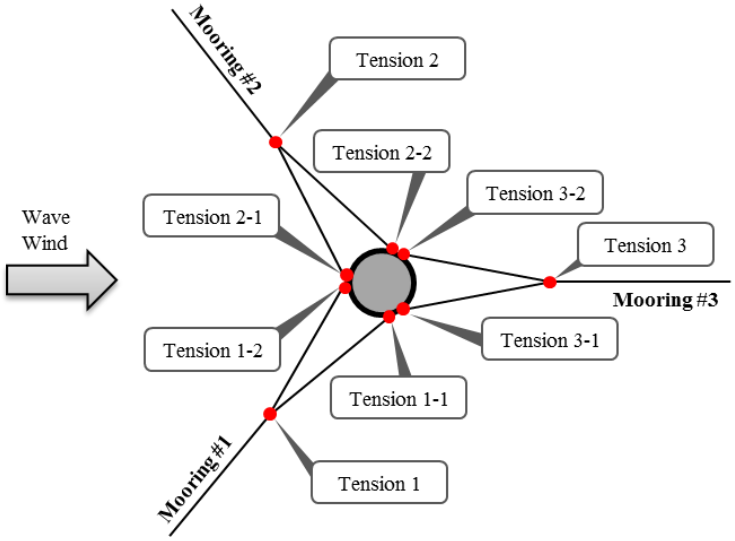

Figure 32 Mooring Layout for Indexing

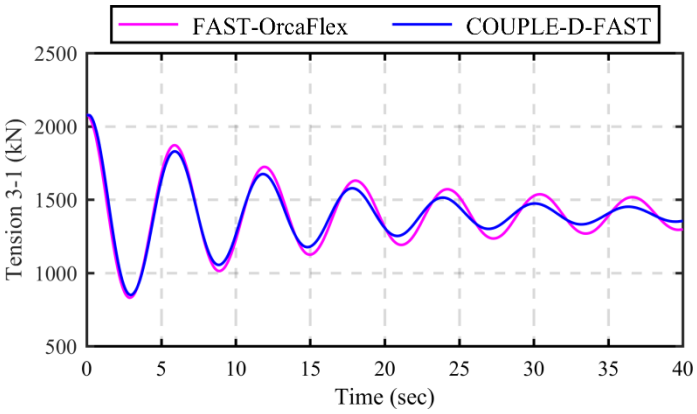

(a) Tension 3-1 (Fairlead)

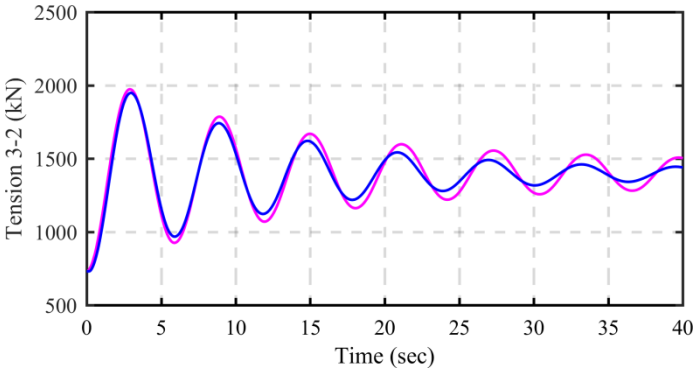

(b) Tension 3-2 (Fairlead)

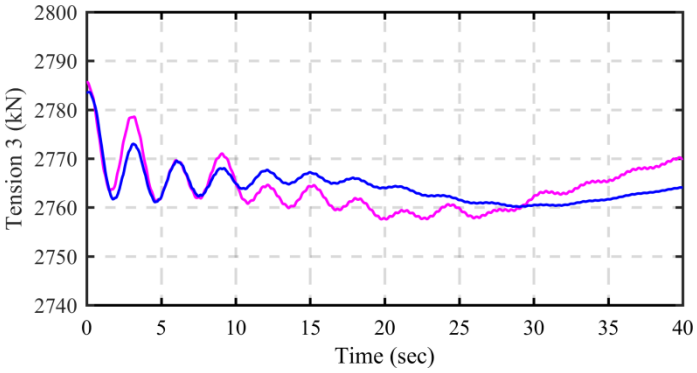

(c) Tension 3 (Delta joint)

Figure 33 Downstream-side Mooring Tension during Yaw Free-decay

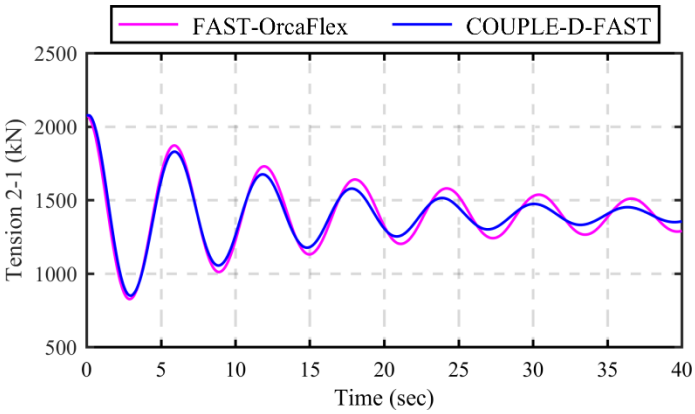

(a) Tension 2-1 (Fairlead)

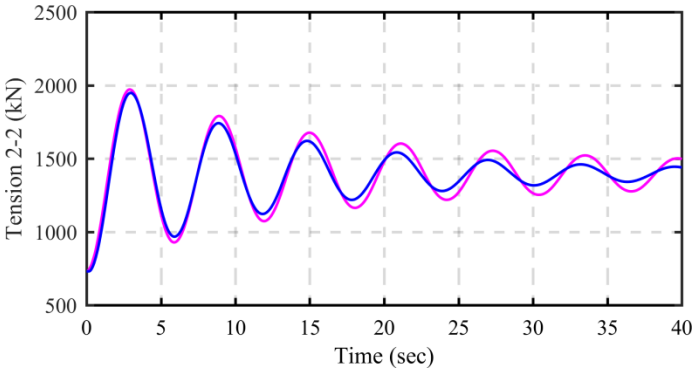

(b) Tension 2-2 (Fairlead)

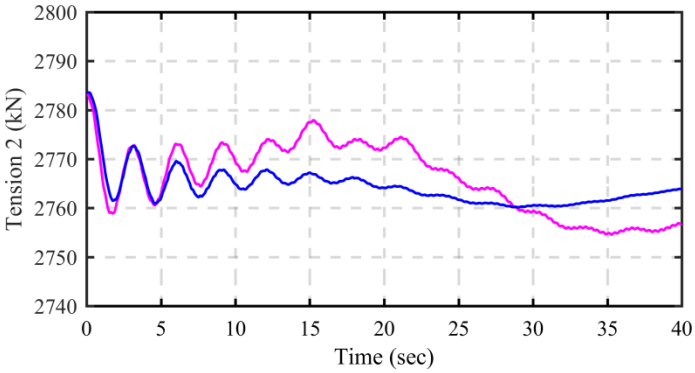

(c) Tension 2 (Delta joint)

Figure 34 Upstream-side Mooring Tension during Yaw Free-decay

6.4. CASE I: Turbulent Winds Impact-Only Cases

Three turbulent wind conditions corresponding to the cases of Operational 1 (LC01), Operational 2 (LC02), and Extreme (LC03) were simulated for a one-hour duration using COUPLE-D-FAST. Figure 35 lists the comparisons of the average platform motion and mooring line tension at joints for the measurement, previous (Min and Zhang, 2017), and current simulations. The numerical comparisons are listed in Table 17. It should be noted that the CG given by the model test was employed in the Min and Zhang (2017)'s simulations. In Figure 35, it is shown that the mean positions from the current simulations were much improved over those in Min and Zhang (2017), indicating that the CG was properly corrected. For LC01 and LC03, the simulated results were in good agreement with the measurements. However, some discrepancies in the mean surge were observed in LC01 and LC03, while the mean pitch motions in the simulations agreed well with the measurements. It should also be noted that the differences of mean surge between the simulated results of COUPLE-D-FAST and the measurements were relatively small, approximately 4 and 10 mm in the model scale for LC01 and LC03, respectively.

LC02 evidenced simulated surge and pitch motions that were smaller than the measurement. This could have been because the measured wind forces were larger than the simulated forces. Although the surge and pitch motions for the model test and simulation were somewhat different for LC02, the mooring line tensions for the simulations and model test were in excellent agreement. This is because the displacements at the fairleads (-70 m from the mean water level) were not as large as the platform displacements at the mean water level.

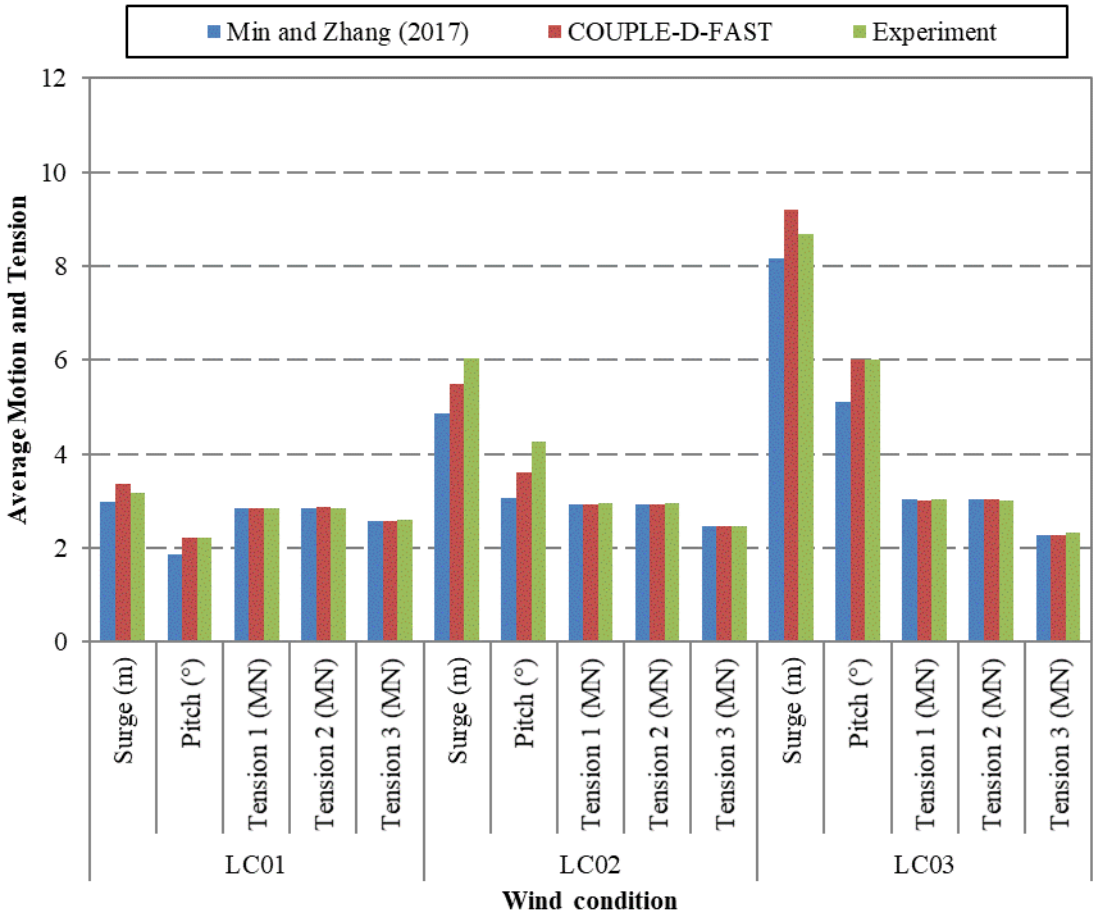

Figure 35 Average Platform Motions and Mooring Tensions (LC01-LC03)

Table 17 Averages of Platform Motions and Mooring Tensions (LC01-LC03)

CASE	Parameter	C-D-F (Old)[1]	C-D-F[2]	EXP[3]
LC01	Surge (m)	2.97	3.37	3.17
	Heave (m)	-0.03	-0.04	-0.06
	Pitch (°)	1.87	2.21	2.21
	Mooring tension 1 (kN)	2855.8	2852.4	2855.1
	Mooring tension 2 (kN)	2855.4	2856.6	2854.6
	Mooring tension 3 (kN)	2578.2	2582.3	2596.8
LC02	Surge (m)	4.87	5.50	6.03
	Heave (m)	-0.08	-0.10	0.04
	Pitch (°)	3.06	3.60	4.26
	Mooring tension 1 (kN)	2916.1	2911.5	2956
	Mooring tension 2 (kN)	2916.7	2918.2	2949.6
	Mooring tension 3 (kN)	2461.1	2468.5	2463.5
LC03	Surge (m)	8.16	9.19	8.69
	Heave (m)	-0.24	-0.29	-0.30
	Pitch (°)	5.12	6.02	6.01
	Mooring tension 1 (kN)	3025.5	3018.9	3026.6
	Mooring tension 2 (kN)	3021.1	3027.1	3010.7
	Mooring tension 3 (kN)	2256.9	2272.2	2317.5

[1] Min and Zhang (2017)'s COUPLE-D-FAST results
[2] COUPLE-D-FAST
[3] Experiment

6.5. CASE II: Waves Impact-Only Cases

6.5.1. Wave Generation

The JONSWAP spectrum was employed to generate irregular waves in both the model test and simulations. Two irregular wave conditions were generated in this study. In the first, the irregular waves had a significant wave height of 2 m and a peak period of 8 sec, with a shape factor of 3.3 (LC04); in the other, the waves had a significant wave height of 7.1 m and a peak period of 12.1 sec, with a shape factor of 2.2 (LC05). To reproduce the waves from the model tests in the simulation, we used the phase information obtained from the resultant waves of the model tests by using IFFT. However, with regards to the wave amplitudes, the values obtained using the JONSWAP spectrum were used. In the simulation, the nonlinear effects of wave-wave interactions were predicted by HWM.

Figure 36 and Figure 37 include comparisons of the measured and simulated wave elevations for LC05 in time and frequency domains, respectively. Overall, the computed wave elevations agreed with the measurements well, as shown in Figure 36. The amplitude spectra of the measurement and simulation were also in good agreement in both the wave frequency (WF) range ($0.05 < f < 0.20$ Hz) and the low frequency (LF) range ($f < 0.05$ Hz), as shown in Figure 37. This clearly indicates that the nonlinear effects of wave-wave interactions were well-predicted by the HWM. However, in the WF range, the amplitude at the peak frequency of the measurement is slightly larger than the simulated one.

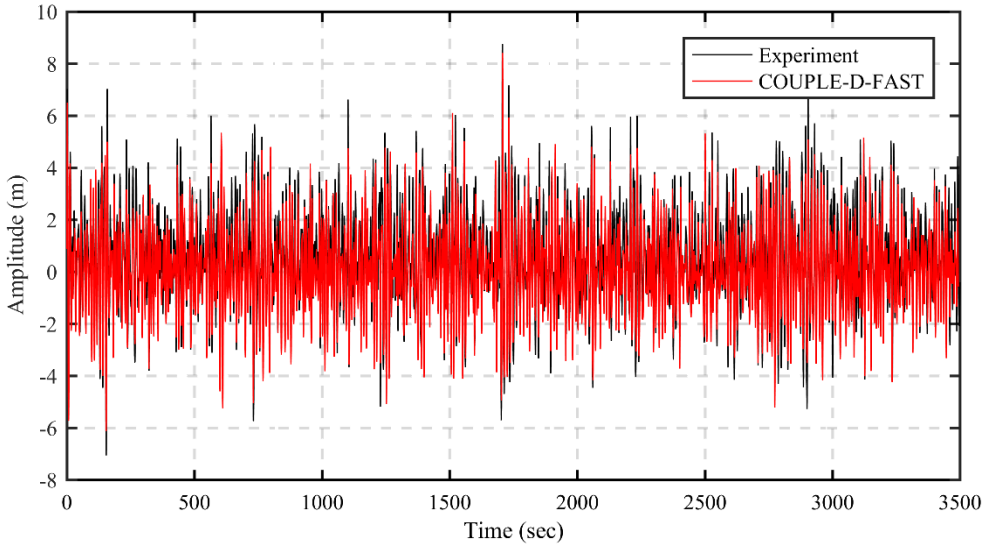

Figure 36 Wave Elevations (LC05)

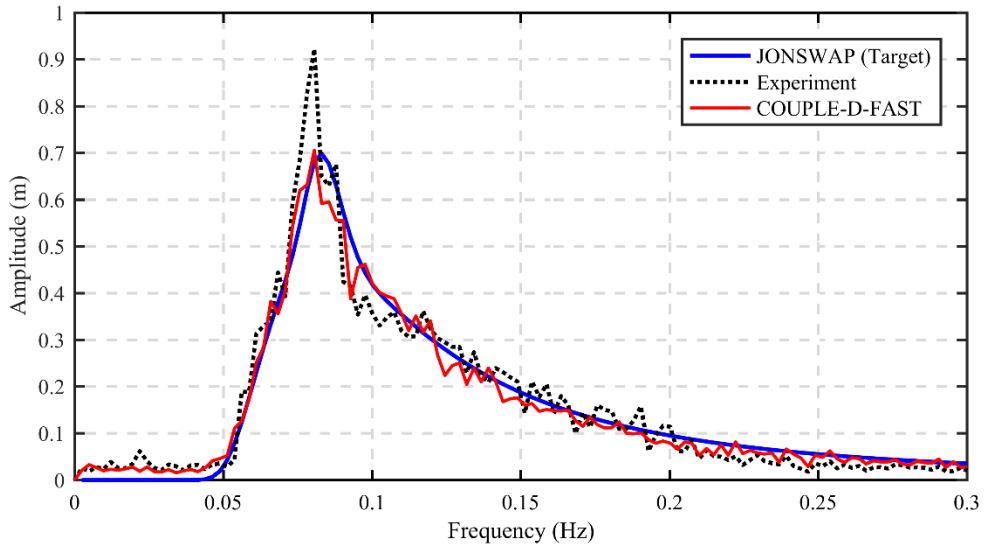

Figure 37 Spectrum of Wave Elevations (LC05)

6.5.2. Simulation Results

The case of LC04 has a significant wave height of 2 m and a peak period of 8 sec. The statistics of the FOWT's motions and mooring tensions are listed in Table 18. Figure 38 shows the comparisons between the measured time series and amplitude spectra for the surge, heave, pitch, and yaw motions and the corresponding predictions. The amplitude spectra were obtained using Fast Fourier Transform (FFT) and an 8-point average smoothing window. Figure 38(a) shows that the average heave motions in the simulation were approximately zero while the measured motions shifted to the positive z-axis direction. This may have been caused by inaccuracy in the measurements because the shifted heave was relatively small (about 3 mm in the model scale). With regard to the platform's dynamic motions within the WF range, 0.05 to 0.20 Hz, Figure 38(b) showed satisfactory agreement between the experiment and the simulation, except for the yaw dynamic motions. While the measurements showed some yaw dynamic motions, the simulated yaw motions were barely observable. Near the surge natural frequency, the surge responses predicted using COUPLE-D-FAST were slightly smaller than those of the experiment.

To examine the discrepancies in heave and yaw motions, the simulated motions from COUPLE-D-FAST were also compared with the corresponding results predicted using FAST-OrcaFlex. Figure 39 shows the platform's heave and yaw motions obtained respectively using the two different programs were in satisfactory agreement. It should be noted that the platform yaw motions were barely observable in both simulations. Imperfect

axisymmetric settings for the wave direction and/or mooring layout may have caused these yaw motions in the measurements.

Table 18 Statistics for Platform Motions and Mooring Tensions (LC04)

		Mean	SD	Max	Min
Surge (m)	Experiment	0.068	0.611	-0.454	0.167
	Simulation	0.012	0.548	-0.523	0.155
Heave (m)	Experiment	0.200	0.383	0.085	0.042
	Simulation	0.002	0.102	-0.076	0.030
Pitch (°)	Experiment	0.151	0.516	-0.224	0.097
	Simulation	0.006	0.367	-0.299	0.080
Yaw (°)	Experiment	-0.106	0.093	0.260	-0.442
	Simulation	0.000	0.000	0.000	0.000
Tension 1 (kN)	Experiment	2775.2	2830.1	2732.4	13.4
	Simulation	2763.1	2802.5	2731.5	10.7
Tension 2 (kN)	Experiment	2781.2	2873.7	2691.3	28.7
	Simulation	2763.1	2802.5	2731.5	10.7
Tension 3 (kN)	Experiment	2768.9	2868.9	2672.8	33.5
	Simulation	2761.5	2828.0	2691.2	21.0

Figure 40 offers a comparison of the mooring line tensions between the measurements and simulations. The measured and simulated mooring tensions were in good agreement, as shown in Figure 40(a). The tension spectra for the downstream side (Mooring Line 3) showed good agreement while the spectra for the upstream side (Mooring Lines 1 and 2) did not (see Figure 40(b)). Specifically, the tensions in Mooring Line 1 was much smaller than those in Mooring Line 2. Ideally, the mooring tensions in the upstream lines should show similar responses because the upstream mooring line layout were symmetric with respect to the wave propagation direction. These discrepancies are also observed in Figure 40(b). The significant differences between tension amplitude spectra of Lines 1 and 2 near the surge natural frequency may have been

caused by the imperfect axisymmetric settings of the mooring lines in the experiment and/or slightly deviated wave direction from the x-axis.

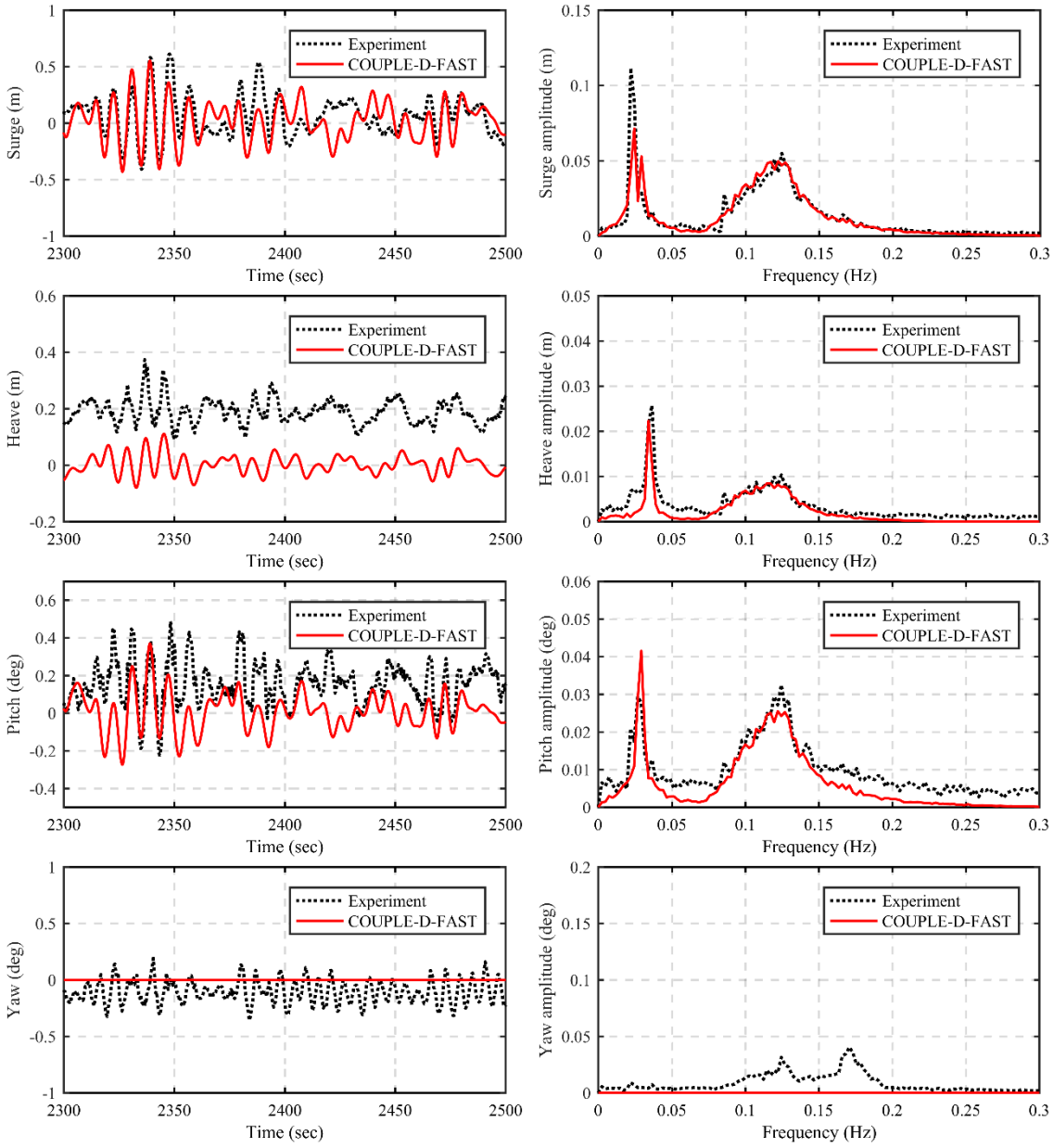

(a) Time series (b) Amplitude spectrum

Figure 38 Comparison of Platform Motions (LC04)

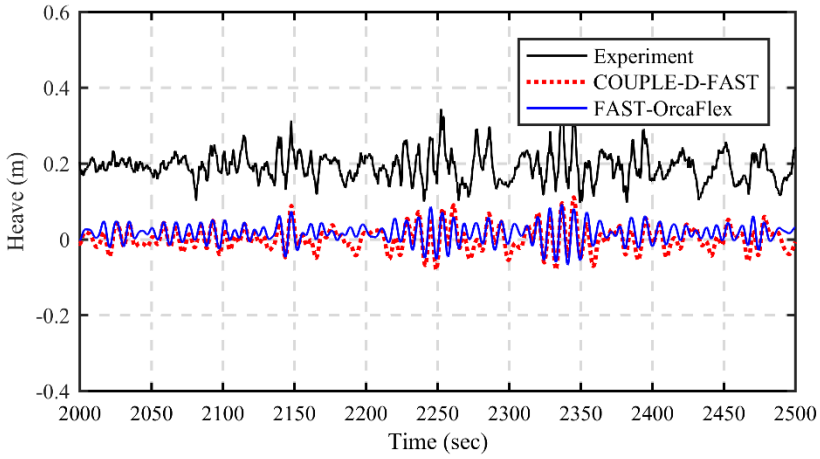

(a) Heave

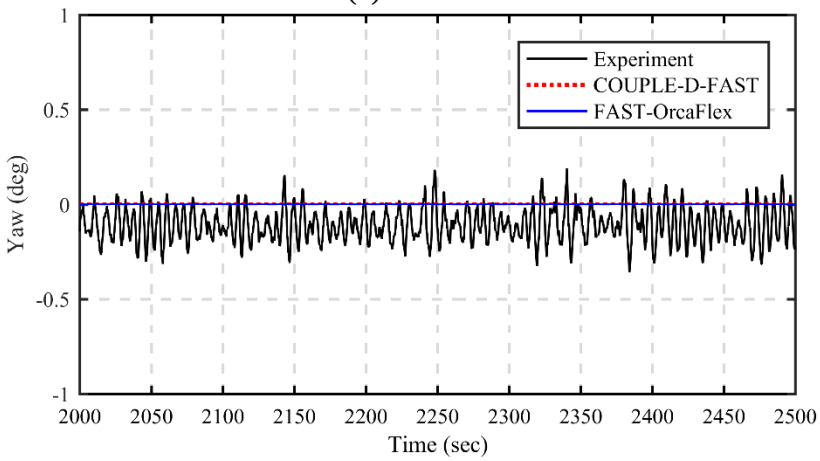

(b) Yaw

Figure 39 Comparison of Simulated Motions (LC04)

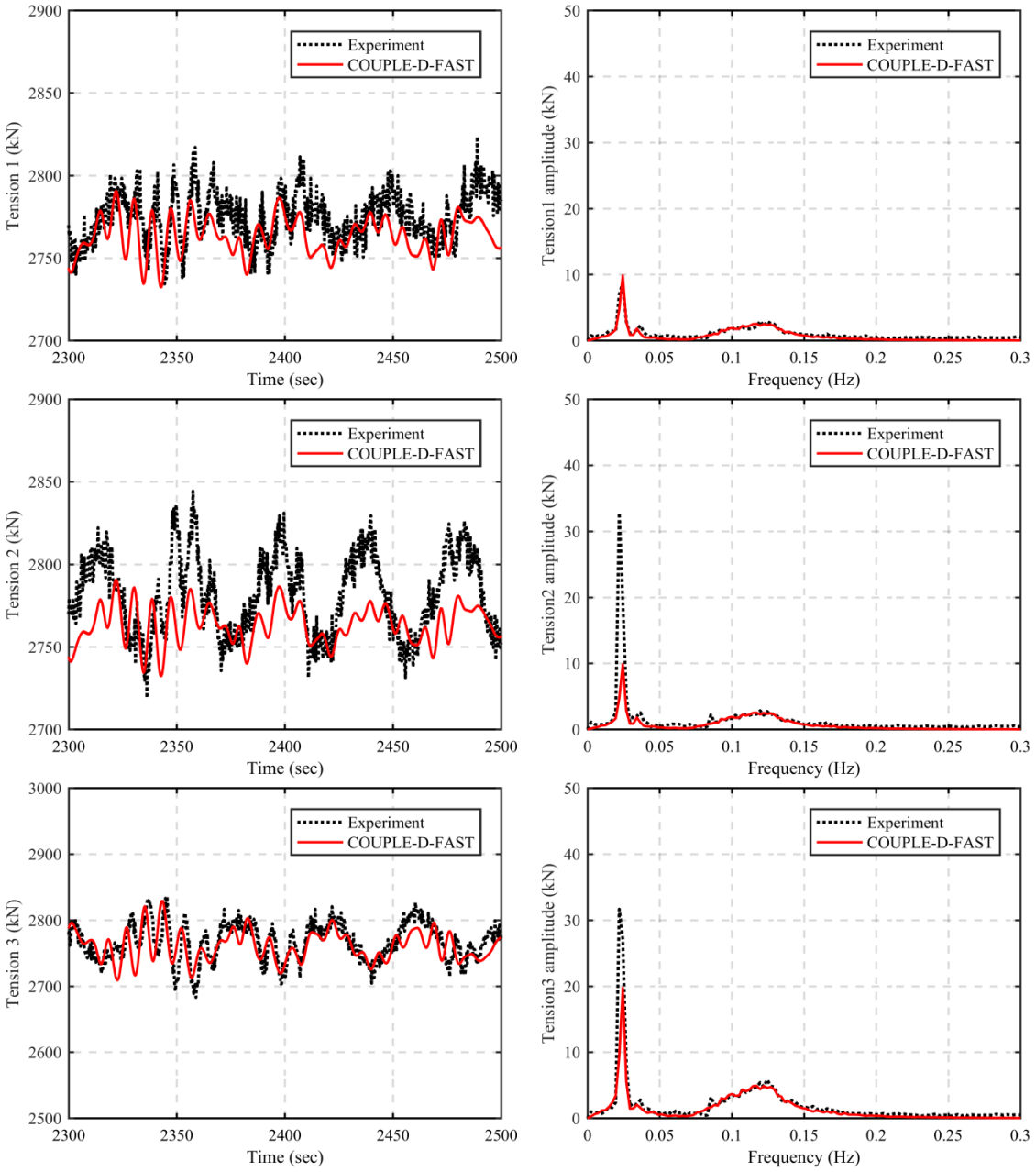

(a) Time series (b) Amplitude spectrum

Figure 40 Comparison of Mooring Tensions at Delta Joint (LC04)

The second set of irregular waves had a significant wave height of 7.1 m and a peak period of 12.1 sec (LC05). The direction of the waves was also set to propagate in the *x*-axis direction. The statistics of the simulation and related measurements are summarized in Table 19. Figure 41 gives the comparisons between the simulated surge, heave, pitch, and yaw motions and the related measurements in both time and frequency domains. In Figure 41(a), it is observed that the simulated motions in general agreed with the measurements. However, the measurements showed some yaw motions while the yaw motions were barely observable in the simulation. Similar to the case of LC04, this may be resulted from the slightly deviated wave direction from the *x*-axis and/or the imperfect symmetric setting of the mooring line layout. Figure 41(b) shows that both the simulated and measured amplitude spectra had a similar response in the WF range ($0.05 < f < 0.20$ Hz). For the LF range ($f < 0.05$ Hz), the overall resonance motions in the simulation showed also similar responses to those in the model test. The mooring tensions at the delta joints are compared in Figure 42 indicating that the computed mooring tensions agreed well with the measured tensions.

Table 19 Statistics for Platform Motions and Mooring Tensions (LC05)

		Mean	SD	Max	Min
Surge (m)	Experiment	0.082	1.042	4.667	-3.739
	Simulation	0.061	1.123	4.182	-4.293
Heave (m)	Experiment	0.172	0.354	1.371	-0.956
	Simulation	0.025	0.301	1.063	-0.982
Pitch (°)	Experiment	0.202	0.505	2.380	-1.758
	Simulation	0.032	0.511	1.693	-1.704
Yaw (°)	Experiment	-0.067	0.213	0.904	-0.969
	Simulation	0.000	0.001	0.003	-0.004
Tension 1 (kN)	Experiment	2774.3	81.7	3059.6	2514.4
	Simulation	2767.5	81.6	3080.8	2496.1
Tension 2 (kN)	Experiment	2780.9	100.8	3098.5	2458.3
	Simulation	2767.5	81.7	3080.9	2496.1
Tension 3 (kN)	Experiment	2764.4	173.8	3368.8	2148.1
	Simulation	2758.8	158.0	3373.6	2199.1

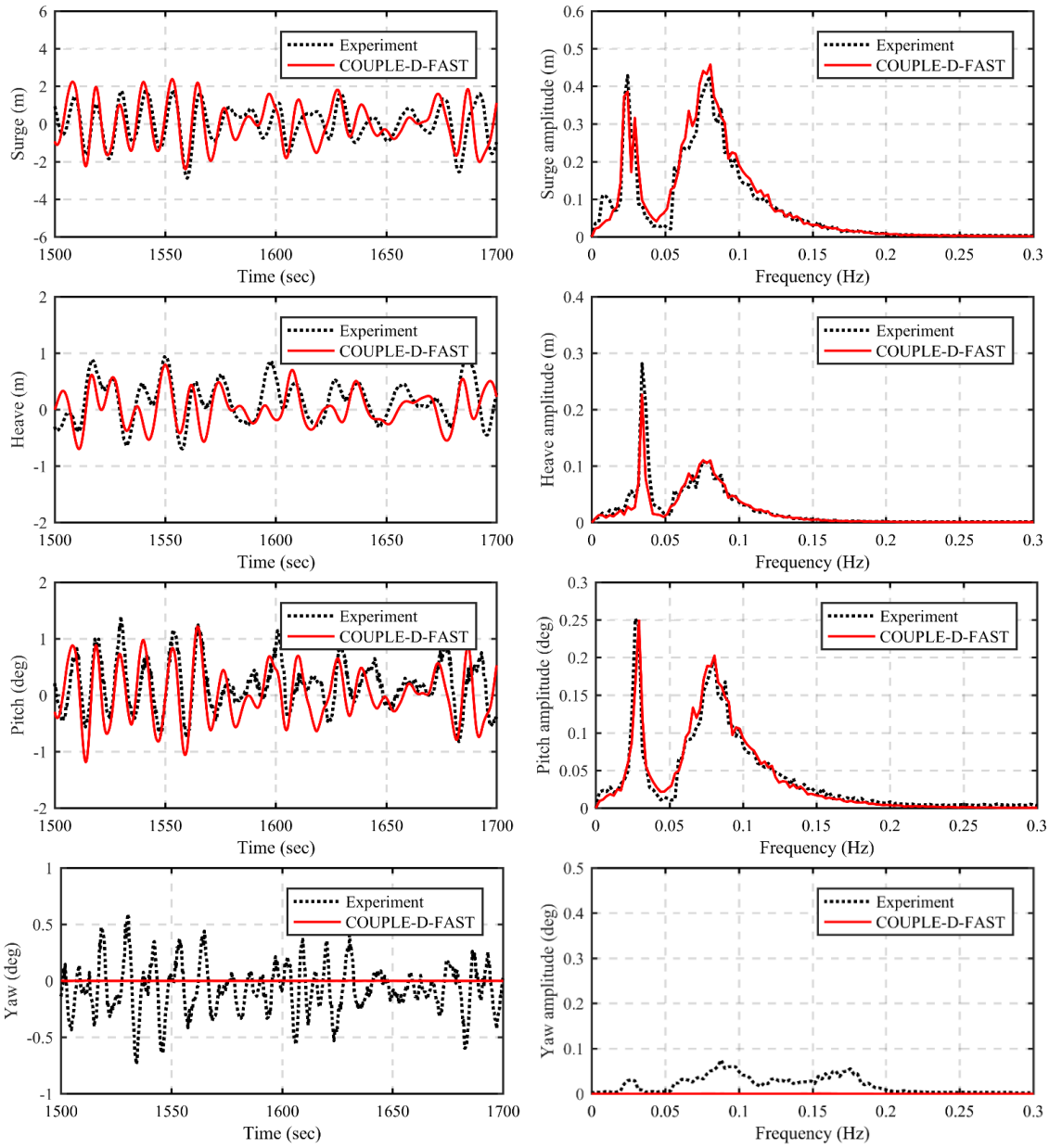

(a) Time series (b) Amplitude spectrum

Figure 41 Comparison of Platform Motions (LC05)

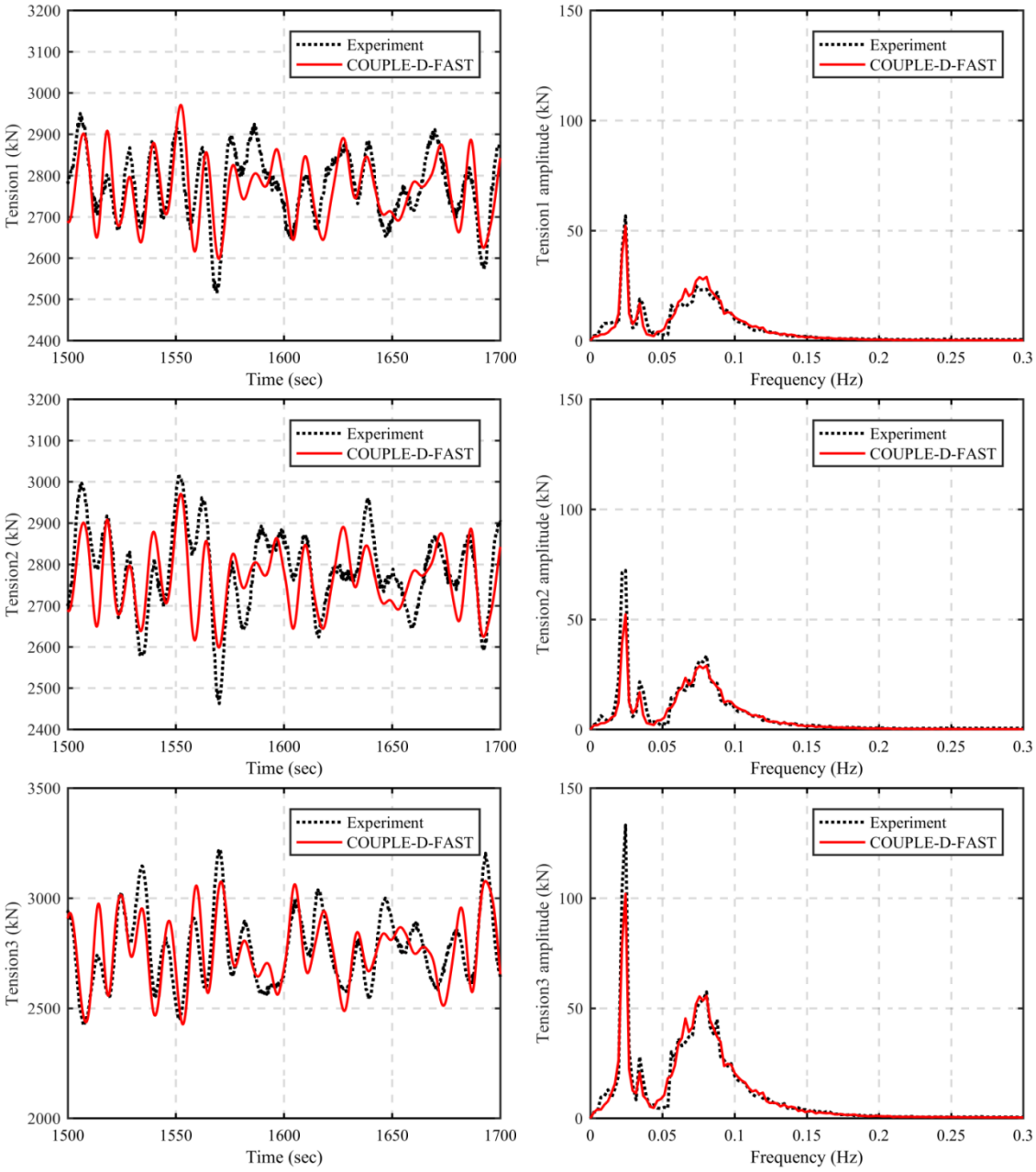

(a) Time series (b) Amplitude spectrum

Figure 42 Comparison of Mooring Tensions at Delta Joint (LC05)

6.6. CASE III: Impact of Turbulent Winds and Regular Waves

Three cases (LC06 to LC08) of regular waves combined with turbulent wind impacts were studied to analyze the platform and mooring responses under ideal wave conditions. The mean positions and tensions of the FOWT and their dynamic responses at the WF are summarized in Table 20. The visualized comparisons of the average and dynamic motions and tensions are depicted in Figure 43 and Figure 44, respectively. In general, the overall mean motions and tensions in simulations showed good agreement with the corresponding measurements as shown in Figure 43, except for the mean yaw. The mean yaw discrepancy was expected because the wind direction in the simulations was perfectly along the *x*-axis direction while that in the model tests might be slightly deviated.

The dynamic responses at the regular wave frequency are shown in Figure 44(a) for the platform motions and in Figure 44(b) for the mooring tensions. The simulated dynamic responses agree well with the related measured values. Although in the case of LC08 the differences in surge amplitude between the measurement and the simulation seemed to be large, the differences were only 3 mm on the model scale. Thus, those differences were considered acceptable in the comparison. The yaw responses at the WF were well-captured, though slight differences (0.2 degrees) were observed in the case of LC07.

Table 20 Averages and Amplitudes of Platform Motions and Mooring Tensions (LC06-LC08)

Case	Parameter	Mean		Amplitude (at WF)	
		Experiment	Simulation	Experiment	Simulation
LC06 (Operational 1)	Surge (m)	3.47	3.37	0.29	0.30
	Heave (m)	0.14	-0.03	0.06	0.05
	Pitch (°)	2.52	2.21	0.15	0.15
	Yaw (°)	0.40	0.09	0.13	0.10
	Mooring 1 (kN)	2879.6	2853.3	13.6	14.5
	Mooring 2 (kN)	2879.2	2857.4	14.5	14.8
	Mooring 3 (kN)	2594.7	2582.0	29.5	29.2
LC07 (Operational 2)	Surge (m)	5.82	5.53	1.61	1.66
	Heave (m)	0.08	-0.07	0.34	0.37
	Pitch (°)	4.16	3.61	0.79	0.78
	Yaw (°)	0.69	0.06	0.40	0.21
	Mooring 1 (kN)	2950.4	2917.4	97.8	94.7
	Mooring 2 (kN)	2947.9	2923.1	90.4	96.2
	Mooring 3 (kN)	2472.5	2467.0	198.3	189.2
LC08 (Extreme)	Surge (m)	8.44	9.24	0.78	0.93
	Heave (m)	-0.54	-0.27	0.20	0.21
	Pitch (°)	6.24	6.04	0.41	0.46
	Yaw (°)	1.30	0.15	0.20	0.19
	Mooring 1 (kN)	3031.9	3023.0	42.8	48.7
	Mooring 2 (kN)	3022.1	3030.7	41.8	50.8
	Mooring 3 (kN)	2327.6	2269.3	93.2	101.5

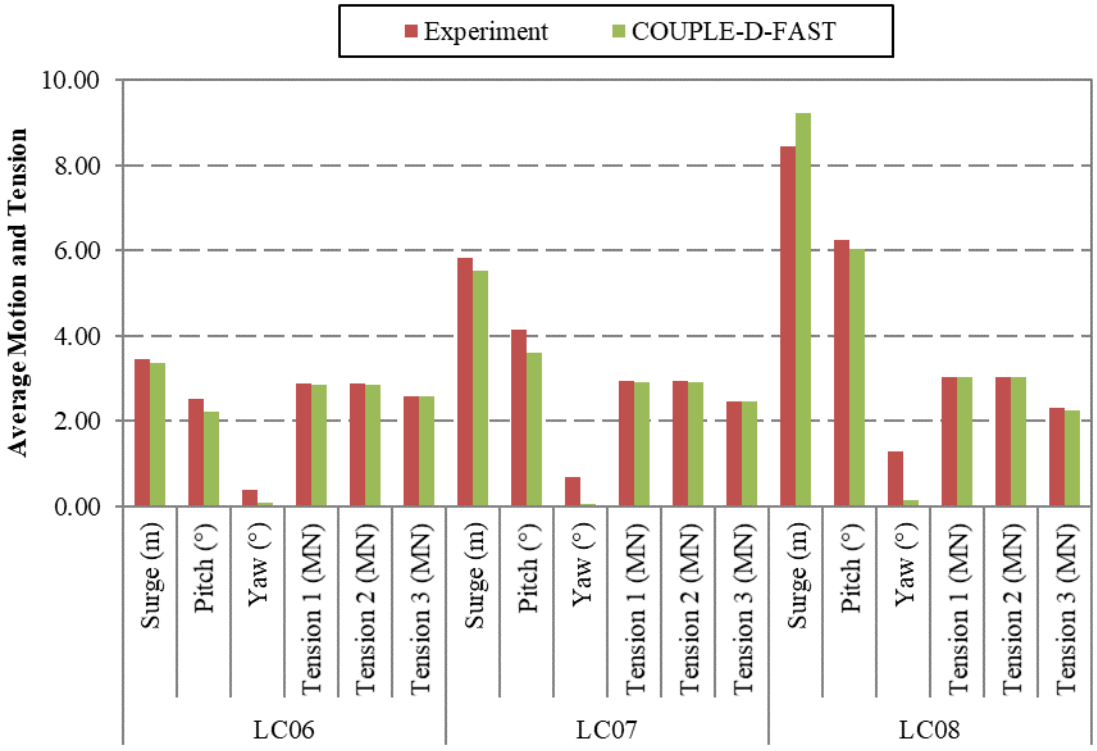

Figure 43 Average Platform Motions and Mooring Tensions (LC06-LC08)

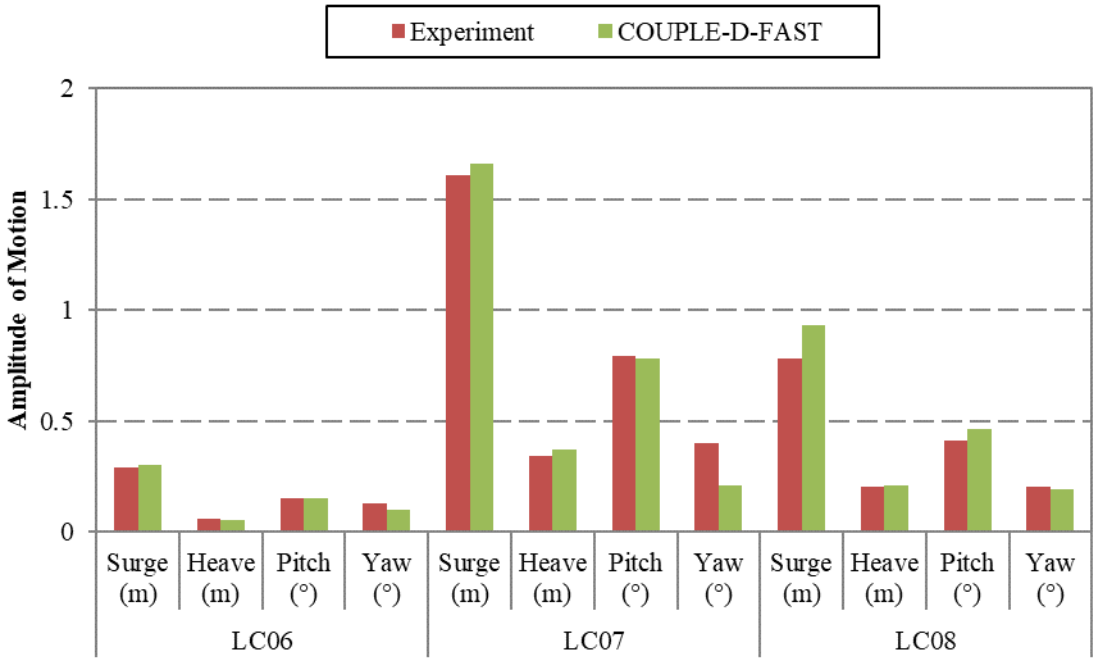

(a) Platform Motions

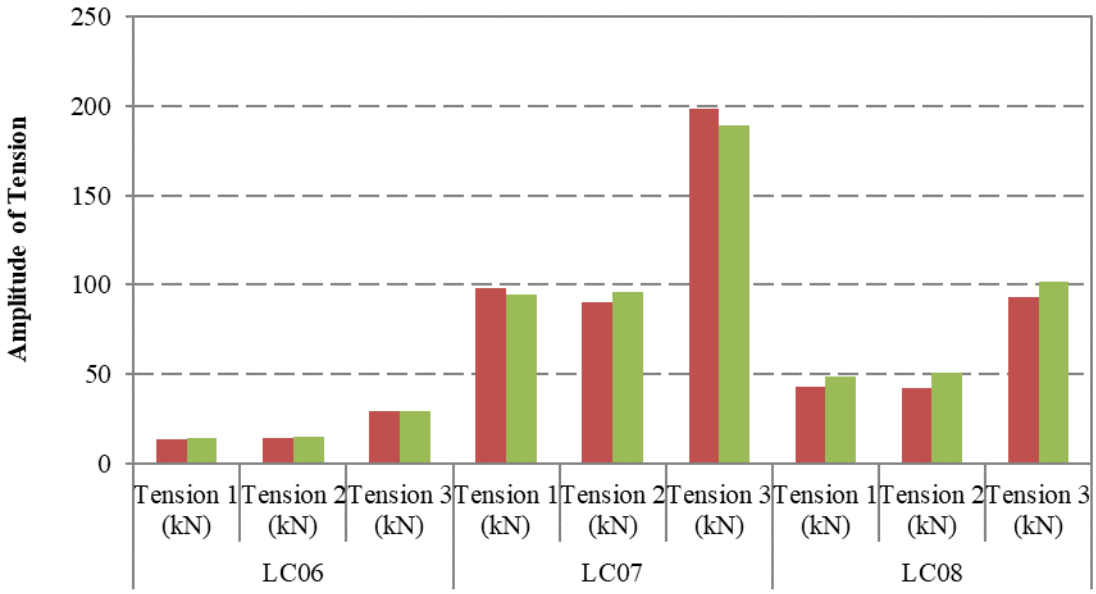

(b) Mooring Line Tensions

Figure 44 Amplitudes of Platform Motion and Mooring Tension at WF (LC06-LC08)

In Figure 45 and Figure 46, the platform motions and mooring system responses of the case of LC08 for the model test and simulations are compared in both time and frequency domains, respectively. In addition to the results obtained using COUPLE-D-FAST, the FAST-OrcaFlex's simulation results are also plotted in these figures. Overall, the simulations obtained using COUPLE-D-FAST and FAST-OrcaFlex, respectively, are in satisfactory agreement.

In Figure 45(a), the surge and pitch time series comparison shows relatively good agreement between COUPLE-D-FAST's prediction and the measurement, but some discrepancies in heave and yaw motions were observed. The mooring tensions in the simulations agreed well with the measured tensions, as shown in Figure 46(a). As can be seen in Figure 45(b) and Figure 46(b), the platform motions and mooring system behaviors in the LF ($f < 0.05$ Hz) were well-captured in the simulations.

The simulated yaw amplitudes at the WF (0.1 Hz) were in excellent agreement with the measurement, but noticeable differences were observed in the frequency range of 0.2 to 0.25. The frequency range corresponded to the measured rotor speed, which in this case was 14.4 rpm (or 0.24 Hz). It should be noted that the platform's yaw motions at this frequency were not excited by the aerodynamic or hydrodynamic load, but the rotor's rotation is able to generate the yaw motions at this frequency, which is known as the gyroscopic effect. However, these motions were not appeared in the simulations (obtained using either COUPLE-D-FAST or FAST-OrcaFlex) at the simulated rotor speed of 12.6 rpm (or 0.21 Hz). This is likely caused by relatively large gyroscopic effect in the model test. This can be expected because of the following two aspects. First, the gyroscopic

frequency and the related moments induced by the rotor rotation were dominated by the Reynolds number not by the Froude number. Secondly, likely uneven mass distributions over the rotor's plane with respect to its center may cause those large gyroscopic motions. Figure 47 show a comparison of the yaw moments (or gyroscopic moments) at the tower top in the COUPLE-D-FAST and FAST-OrcaFlex simulations, with the corresponding measurements. As expected, the measured gyroscopic moments were much larger than the simulated ones.

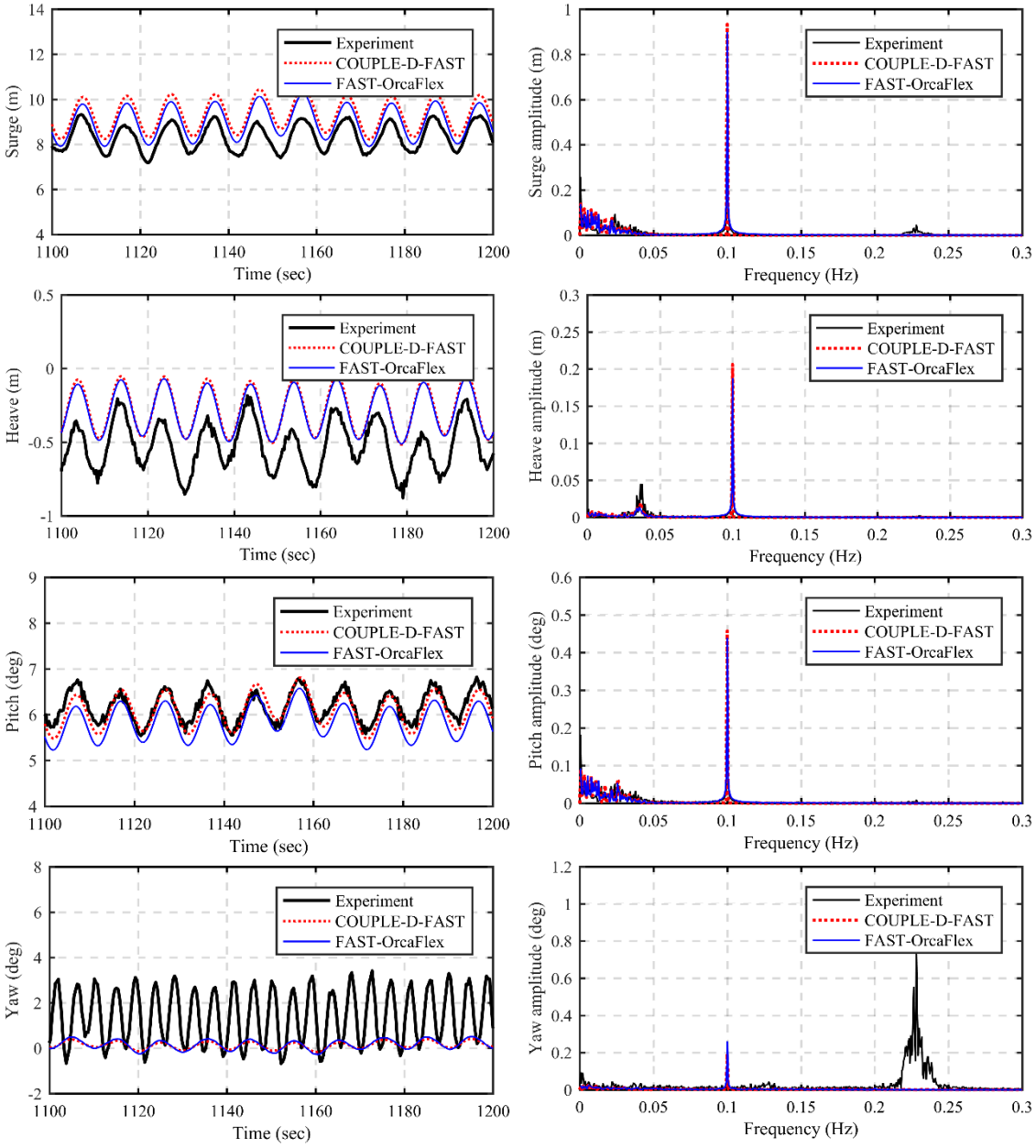

(a) Time series (b) Amplitude spectrum

Figure 45 Comparison of Platform Motions (LC08)

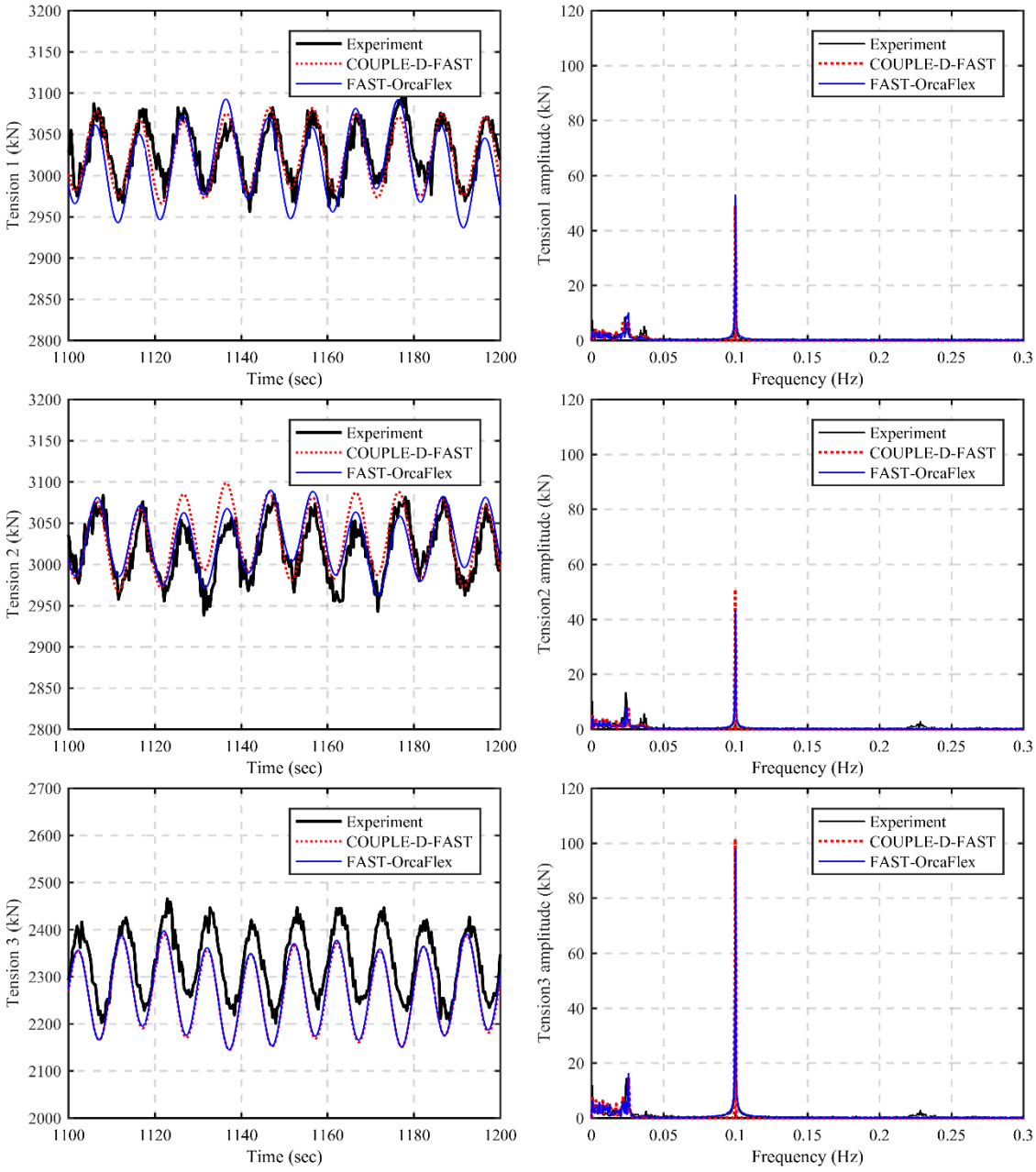

(a) Time series (b) Amplitude spectrum

Figure 46 Comparison of Mooring Tensions at Delta Joint (LC08)

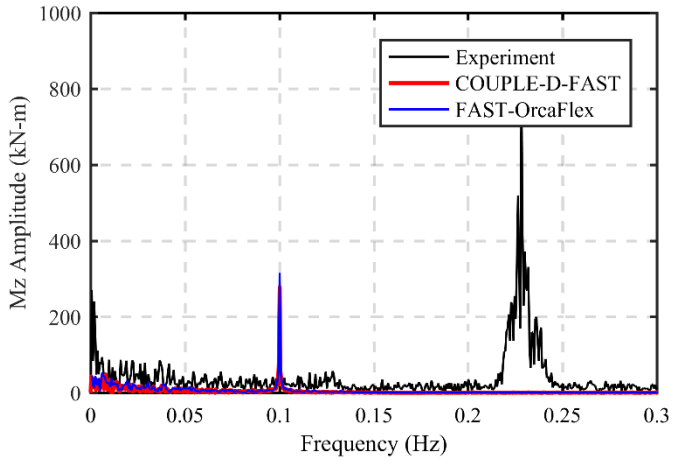

Figure 47 Comparison of Tower-top Yaw Moments (LC08)

6.7. CASE IV: Impact of Turbulent Winds and Irregular Waves

Three cases (LC09 to LC11) of the Hywind FOWT's dynamic behavior were investigated under the impact of turbulent winds and irregular waves. The main parameters of the three cases were listed in Table 12. The statistics of the FOWT's responses and mooring lines' tensions for the Operational 1 (LC09), Operational 2 (LC10), and Extreme (LC11) cases are summarized in Table 21. Most of the simulated results are agree with the measurements. However, relatively large differences were observed in the yaw motions. The discrepancies in average yaw may have been the result of the tested wind conditions not being directly used in the simulations. The standard deviations in yaw also rendered some discrepancies. It is mainly because the simulated yaw motions excited by the rotor-rotations were not as large as the measurements.

Figure 48 and Figure 49 show the time series and amplitude spectra of the case of LC11 for the platform motions and the mooring tensions at the joints for the measurements and COUPLE-D-FAST and FAST-OrcaFlex predictions. In this case, irregular waves

were characterized by a significant wave height of 7.1 m/s and a peak period of 12.1 sec, with a shape factor of 2.2, and the extreme wind conditions with wind speed at 11.41 m/s. The simulated surge and pitch motions obtained using both simulations are in good agreement with the related measurements in the time domain comparisons. However, both simulated heave motions were slightly different from the measured motions in the time domain comparison (see Figure 48(a)). On the other hand, the computed heave spectrum is satisfactory agreement with the measured spectrum, but they also showed slight discrepancy near the heave natural frequency. The surge spectrum between the measurements and simulations was in excellent agreement for both LF ($f < 0.05$ Hz) and WF ($0.05 < f < 0.20$ Hz) ranges. However, a small peak in the frequency range between 0.20 Hz and 0.25 Hz was found only in the experimental results, where the frequency range corresponds to the rotor's rotational speed of 14.4 rpm (or 0.24 Hz). The yaw spectrum in the WF range also showed that both simulated motions were in good agreement with the measurements. A large peak was observed near the rotor-rotation frequency in the measurements, which is consistent with the case of extreme winds with regular waves (LC08) depicted in Figure 45. This is because the measured gyroscopic moments excited by the rotor's rotation were much larger than the simulated moments, as shown in Figure 50.

In the WF range, the simulated pitch motions agreed well with the measurements. Compared to the case of LC05 (wave impact-only; see Figure 41), a reduction in pitch resonance was found for both measurements and simulations. The resonance reduction was induced by an interaction between the wind and platform motions, which is known as

aerodynamic damping. One interesting phenomenon was that the degree of reduction in pitch was different between the measurements and simulations. It is also observed that the surge resonance motions between the measurements and simulations are in good agreement. This indicates that the aerodynamic damping forces among the model test and simulations were different. The damping difference may have been caused by the scale effect from the Froude similitude because the aerodynamic damping follows the Reynolds number scaling.

All computed tensions at the delta mooring joints were in satisfactory agreement with the measurement in both time and frequency domain comparisons (see Figure 49). However, some tension discrepancies were found in the LF range, which may be caused by the differences in pitch resonance motions.

Table 21 Statistics for Platform Motions and Mooring Tensions (LC09-LC11)

			Mean	SD	Max	Min
LC09	Surge (m)	Experiment	3.316	0.221	4.068	2.659
		Simulation	3.377	0.242	4.316	2.538
	Heave (m)	Experiment	0.153	0.051	0.349	-0.014
		Simulation	-0.037	0.034	0.084	-0.129
	Pitch (°)	Experiment	2.445	0.151	3.014	1.886
		Simulation	2.211	0.149	2.698	1.764
	Yaw (°)	Experiment	0.344	0.753	1.928	-1.215
		Simulation	0.036	0.081	0.325	-0.247
	Tension 1 (kN)	Experiment	2870.3	16.5	2926.5	2810.5
		Simulation	2853.1	12.4	2900.8	2807.1
	Tension 2 (kN)	Experiment	2873.0	26.2	2961.2	2786.2
		Simulation	2857.4	12.3	2905.1	2814.9
	Tension 3 (kN)	Experiment	2599.0	31.0	2701.4	2492.3
		Simulation	2581.4	24.0	2663.5	2481.1
LC10	Surge (m)	Experiment	5.841	0.981	9.656	2.556
		Simulation	5.557	1.103	9.443	1.526
	Heave (m)	Experiment	-0.469	0.313	0.676	-1.581
		Simulation	-0.080	0.303	0.999	-1.094
	Pitch (°)	Experiment	4.520	0.484	6.267	2.818
		Simulation	3.628	0.495	5.358	2.081
	Yaw (°)	Experiment	0.987	1.216	3.329	-1.551
		Simulation	0.063	0.155	0.607	-0.536
	Tension 1 (kN)	Experiment	2947.2	80.2	3224.8	2684.6
		Simulation	2917.3	76.2	3228.2	2674.8
	Tension 2 (kN)	Experiment	2941.7	99.9	3279.1	2599.7
		Simulation	2923.3	78.3	3235.7	2673.0
	Tension 3 (kN)	Experiment	2448.1	177.5	3027.2	1799.8
		Simulation	2464.3	152.8	3072.6	1940.5
LC11	Surge (m)	Experiment	8.679	1.039	13.540	5.252
		Simulation	9.303	1.105	13.172	4.765
	Heave (m)	Experiment	-0.595	0.318	0.481	-1.794
		Simulation	-0.268	0.299	0.890	-1.182
	Pitch (°)	Experiment	6.420	0.524	8.696	4.857
		Simulation	6.075	0.509	7.668	4.218
	Yaw (°)	Experiment	1.256	1.135	3.733	-1.270
		Simulation	0.133	0.178	0.771	-0.579
	Tension 1 (kN)	Experiment	3037.1	81.2	3333.5	2747.1
		Simulation	3026.8	74.8	3324.2	2787.5
	Tension 2 (kN)	Experiment	3028.0	96.7	3415.0	2692.3
		Simulation	3034.0	78.0	3335.4	2753.6
	Tension 3 (kN)	Experiment	2306.3	179.5	2878.8	1681.2
		Simulation	2264.7	154.7	2914.8	1732.1

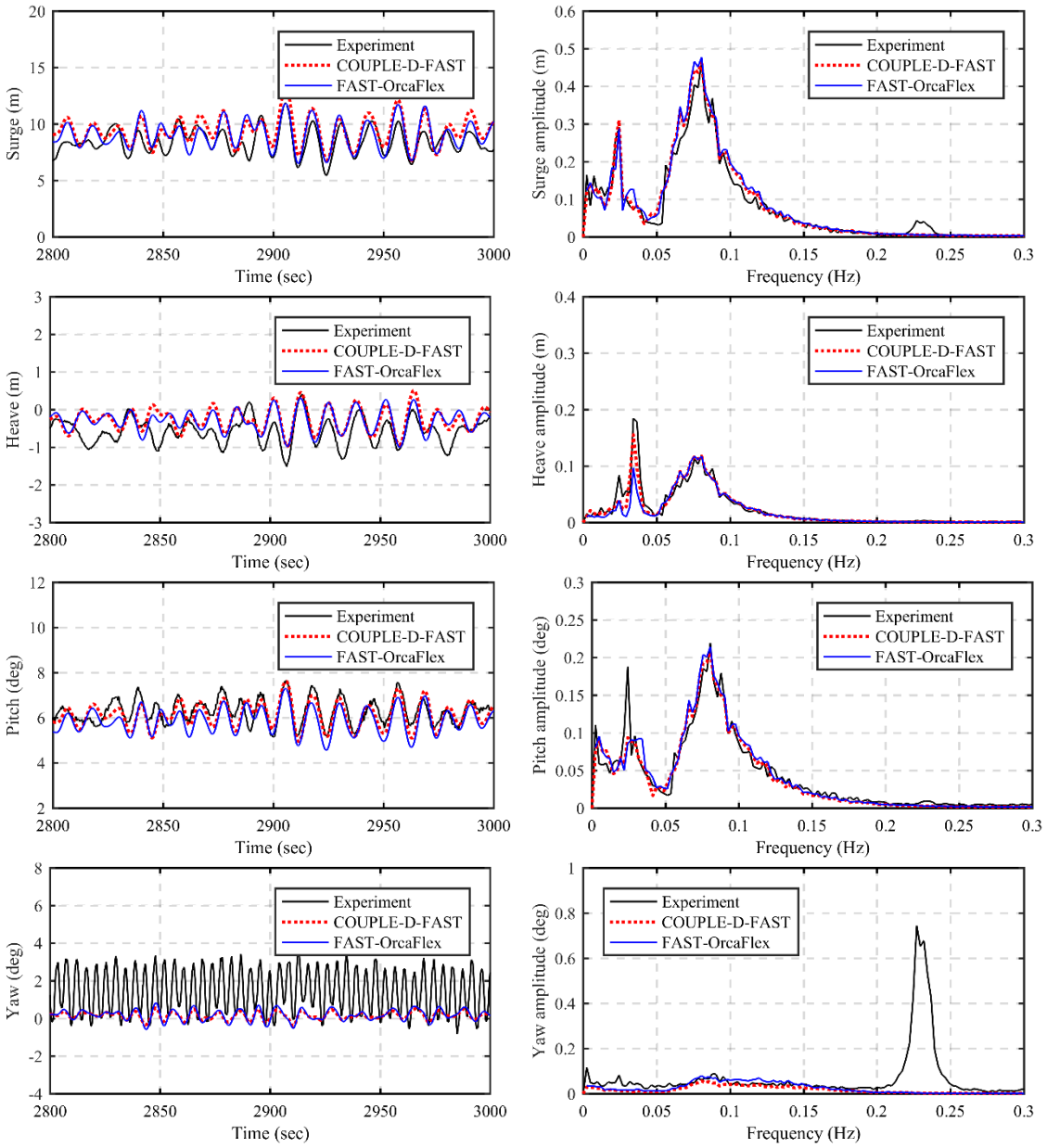

(a) Time series (b) Amplitude spectrum

Figure 48 Comparison of Platform Motions (LC11)

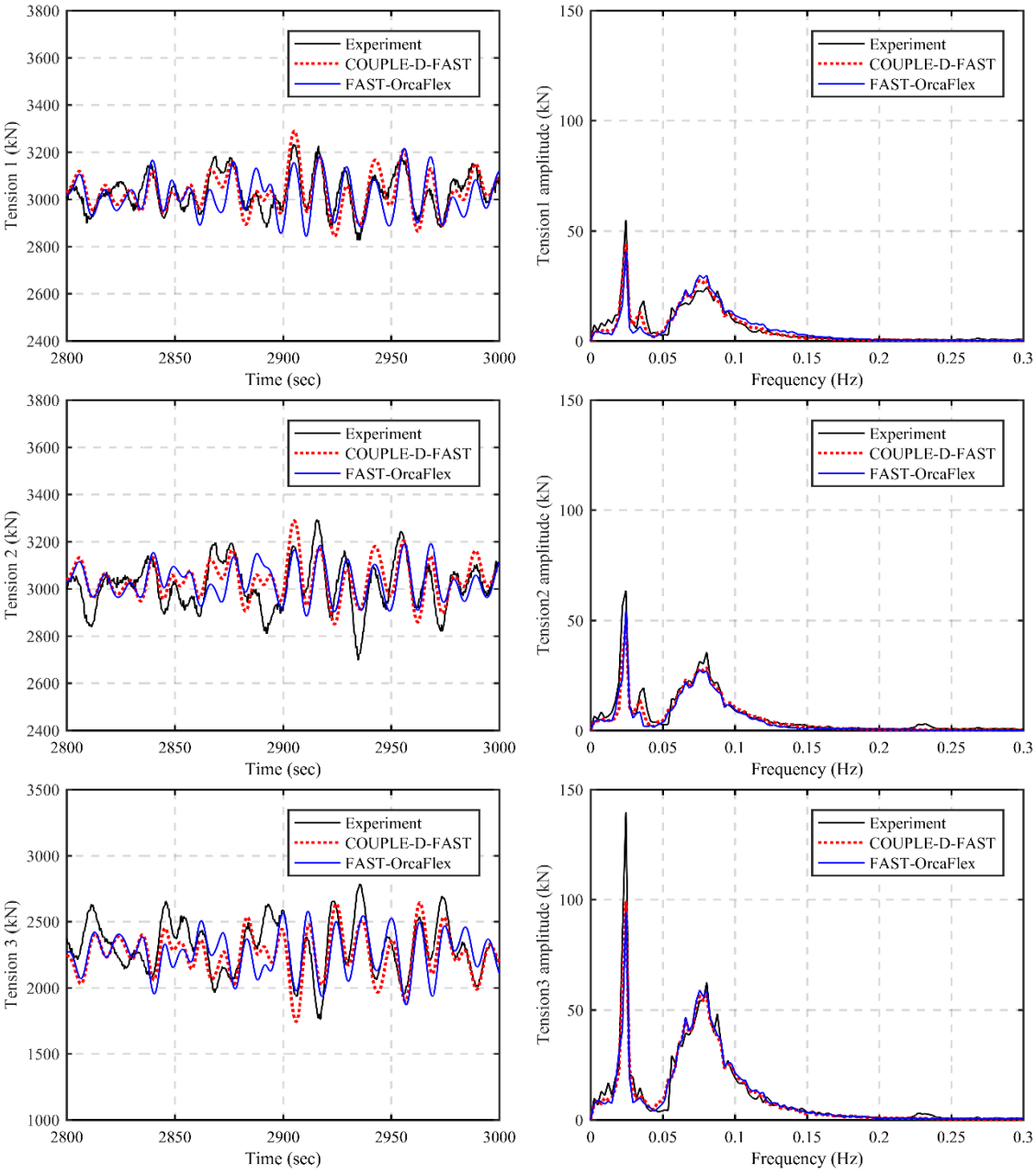

(a) Time series (b) Amplitude spectrum

Figure 49 Comparison of Mooring Tensions at Delta Joint (LC11)

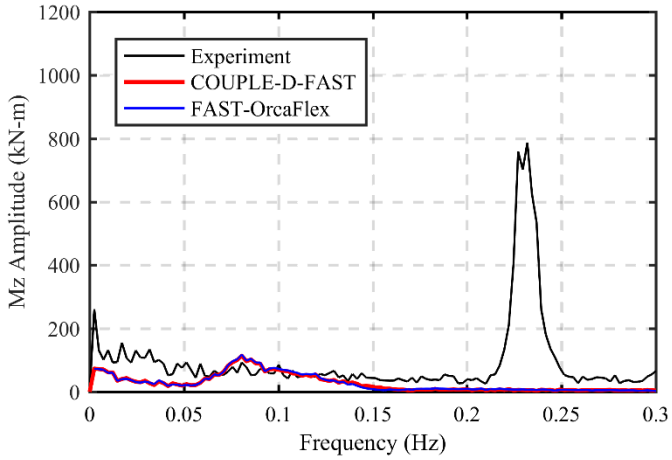

Figure 50 Comparison of Tower-top Yaw Moments (LC11)

6.8. Discussion

In this section, COUPLE-D-FAST was verified through the comparisons of its simulations with the related results of model tests. FAST-OrcaFlex was also used for the simulation to examine the validity of COUPLE-D-FAST in certain cases where the comparison between the measurements and simulations showed significant and/or qualitative differences. The simulations using measured wind forces were implemented using COUPLE-D only, mainly to investigate the sources causing the discrepancies in mean motions (as described in Section 5.4) among the model test and simulations. The simulations led to a correction of the center of gravity for the Hywind, which was changed by approximately 3% closer to the water surface. The pitch free-decay test demonstrated the validity of the CG correction, in that the case-specific increases in the moments of inertia were no longer needed which were applied in our previous works (Min et al., 2016; Min and Zhang, 2017). The CG correction led to the results that the simulated average platform motions obtained in this research are in much better agreement with the measured motions than that in our previous studies.

Eleven cases of various wind and wave conditions were simulated. The simulated results were then compared to the corresponding measurements. The overall simulated platform responses and mooring tensions agreed well with the measurements. In cases of winds with irregular waves, the pitch resonances in the simulations were smaller than the measured pitch resonances. This may have been caused by the different aerodynamic damping which may result from the fact that the Froude similitude does not comply to the scaling of aerodynamic forces. While the yaw resonances were barely visible in the

simulated results, the measurements showed large yaw resonances in the range of the rotor-rotational frequency. This implies that the gyroscopic effects induced by the rotor's rotation in the model tests were larger than those in the simulation.

7. CONCLUSIONS

In this study, the CABLE3D module in COUPLE-FAST was extended to enable the simulation of a delta mooring system. The extended COUPLE-FAST was named as COUPLE-D-FAST. It was then used to investigate the dynamics of Hywind, a spar-type FOWT with a delta mooring system. In most numerical simulations conducted in the previous studies of Hywind, its delta mooring system was simplified to be a single mooring system for the sake of simplicity, which needs empirical tuning and calibration of its yaw stiffness and damping. The focus of this dissertation was to validate COUPLE-D-FAST through comparisons with the related model tests and simulations using other software, such as COUPLE-FAST and FAST-OrcaFlex.

The input to the numerical simulation carefully followed the major conditions and settings of the model tests conducted in the wave basin. However, some features were adjusted for the simplification of the computation. For example, the taper section of the Hywind platform was approximated by a step cylinder. The following aspects of the numerical model were carefully calibrated: mooring line stiffness, tower bending stiffness, added-mass and drag coefficients of the platform.

The delta mooring system was modeled in the COUPLE-D-FAST and FAST-OrcaFlex simulations without the simplification. For COUPLE-FAST, the empirically calibrated yaw stiffness and damping were added, as has been done in the previous research (Browning et al., 2012; Jonkman and Musial, 2010; Min et al., 2016). The mooring surge and sway stiffness curves of all simulations and the related measurements were in satisfactory agreement. The yaw stiffness curves calculated using COUPEL-D-

FAST and FAST-OrcaFlex, respectively, were in satisfactory agreement. The curves also showed that the delta mooring system rendered a significantly large yaw stiffness compared to the simplified mooring systems (without tuning the yaw stiffness) in COUPLE-FAST.

COUPLE-D-FAST was initially calibrated by comparing its predictions with the related free-decay tests. For translational motion, the simulated free-decay responses were in good agreement with the corresponding measurements. In the yaw decay tests, the effects of the yaw damping and stiffness related to the delta mooring system were captured by COUPLE-D-FAST, and there was no need for additional case-specific tuning. In terms of yaw damping effects, COUPLE-D-FAST was able to capture the damping effects better than FAST-OrcaFlex.

Although Min and Zhang (2017) corrected the nominal wind speeds identified in the model tests, the average motions of the Hywind FOWT was still smaller than those recorded in the model tests. When the measured wind forces were directly input to the simulations instead of those predicted by FAST, the predicted mean surge and pitch motions rendered still smaller values compared to the mean motions in the model tests. The smaller mean motions were likely caused by the hydrostatic pitch stiffness, which is the dominant factor determining the mean pitch and surge of a spar-buoy platform at the mean water level. To examine the effects of hydrostatic stiffness, we changed the Hywind's center of gravity by 3% closer to the calm water surface. The simulations using the changed center of gravity showed that the average surge at the mean water level and pitch motions were in satisfactory agreement with the related measurements. In addition,

there was no need to have an adjusted increase in the pitch moment of inertia to match the pitch natural frequency, as did in our previous work (Min et al., 2016; Min and Zhang, 2017).

Eleven different cases were simulated and compared with the corresponding model tests in order to validate COUPLE-D-FAST. These cases can be divided into four different-load categories: wind load-only, irregular wave load-only, combined wind and regular wave loads, and combined wind and irregular wave loads.

For the wind impact-only cases, the average platform motions predicted using COUPLE-D-FAST showed satisfactory agreement with the corresponding measurements, which is better than the results of our previous study (Min and Zhang, 2017). For the irregular wave load-only cases, the phase of wave components obtained from for the measured wave elevations was used for the simulation of the incident waves following the corresponding JONSWAP spectrum. As expected, the simulated wave amplitude spectra were similar to the related measured ones. The simulated FOWT's global motion and mooring tension at the delta joints showed satisfactory agreement with the corresponding measurements in both time and frequency domains. In cases of regular waves combined with wind, the mean position and dynamic response predicted using COUPLE-D-FAST showed good agreement with the related model tests. Although some differences in the surge amplitude at the wave frequency were observed, the magnitude of those differences were very small (3 mm) in the model scale. For cases of irregular waves with wind, the simulated FOWT's behaviors, including motions and tensions, agreed very well with the measurements in both time and frequency domain comparisons. The computed pitch

resonance in the LF range (near the natural frequencies of the surge and pitch) rendered a relatively small response in comparison to those of the measurements. It is probably caused by the different aerodynamic damping effects between the model tests and simulations, because the aerodynamic damping effects follow the Reynolds number instead of the Froude number.

The simulated yaw motion in the WF range showed satisfactory agreement with the corresponding measurements. However, the simulated mean yaw motion showed unsatisfactory agreement with the related measurements. Therefore, in addition to the COUPLE-D-FAST simulations, FAST-OrcaFlex simulations were conducted to investigate those discrepancies in the COUPLE-D-FAST simulations. It was shown that the two numerical simulations were in good agreement in both time and frequency domains. Yaw motions, other than the wave frequency, showed large discrepancies between the simulations and the model tests. That is, the yaw motion induced by a gyroscopic effect was barely observable in the simulations, while the model tests showed relatively large yaw motions near the rotor-rotation frequency. The large yaw discrepancies at the rotor-rotation frequency were expected. First, it is known that the gyroscopic frequency and the related moments resulting from the blade rotation of the wind turbine does not follow the Froude number scaling of the model tests to the prototype. Secondly, likely uneven mass distribution over the rotor's plane with respect to its center in the model test may result in larger gyroscopic moments than those in the simulations

Our research has shown that COUPLE-D-FAST can reliably and accurately simulate the Hywind's behaviors including its delta mooring system. The accurate prediction of mooring tensions for all mooring segments of the delta mooring system will contribute to FOWT design by providing key information such as fatigue life estimations for mooring lines.

REFERENCES

Andersen, M. T., Wendt, F. F., Robertson, A. N., Jonkman, J. M., and Hall, M. 2016. "Verification and Validation of Multisegmented Mooring Capabilities in Fast V8." The 26th International Ocean and Polar Engineering Conference, Rhodes, Greece.

Aranha, J. 1994. "A Formula for 'Wave Damping'in the Drift of a Floating Body." *Journal of Fluid Mechanics* 275:147-155.

Bae, Y. H., Kim, M. H., Im, S. W., and Chang, I. H. 2011. "Aero-Elastic-Control-Floater-Mooring Coupled Dynamic Analysis of Floating Offshore Wind Turbines." The 21st International Offshore and Polar Engineering Conference, Maui, Hawaii, USA.

Browning, J., Jonkman, J., Robertson, A., and Goupee, A. 2012. "Calibration and Validation of a Spar-Type Floating Offshore Wind Turbine Model Using the Fast Dynamic Simulation Tool." Proceedings of the Science of Making Torque From Wind, Oldenburg, Germany.

Cao, P., and Zhang, J. 1997. "Slow Motion Responses of Compliant Offshore Structures." *International Journal of Offshore and Polar Engineering* 7 (02):119-126.

Chen, X. 2002. "Studies on Dynamic Interaction between Deep-Water Floating Structures and Their Mooring/Tendon Systems." Doctor of Philosophy Thesis, Ocean Engineering Program, Civil Engineering Department, Texas A&M University.

Clark, P., Malenica, Š., and Molin, B. 1993. "An Heuristic Approach to Wave Drift Damping." *Applied Ocean Research* 15 (1):53-55.

Duan, F., Hu, Z., and Wang, J. 2015. "Model Tests of a Spar-Type Floating Wind Turbine under Wind/Wave Loads." ASME 2015 34th International Conference on Ocean, Offshore and Arctic Engineering, St. John's, Newfoundland, Canada.

Garrett, D. 1982. "Dynamic Analysis of Slender Rods." *Journal of Energy Resources Technology* 104 (4):302-306.

Goupee, A. J., Koo, B. J., Kimball, R. W., Lambrakos, K. F., and Dagher, H. J. 2014. "Experimental Comparison of Three Floating Wind Turbine Concepts." *Journal of Offshore Mechanics and Arctic Engineering* 136 (2):020906-020906.

Hall, M., and Goupee, A. 2015. "Validation of a Lumped-Mass Mooring Line Model with Deepcwind Semisubmersible Model Test Data." *Ocean Engineering* 104:590-603.

Jonkman, B. J. 2009. Turbsim User's Guide: Version 1.50. National Renewable Energy Laboratory, Golden, CO, USA.

Jonkman, J. M. 2007. Dynamics Modeling and Loads Analysis of an Offshore Floating Wind Turbine. National Renewable Energy Laboratory, Golden, CO, USA.

Jonkman, J. M. 2010. Definition of the Floating System for Phase IV of OC3. National Renewable Energy Laboratory, Golden, CO, USA.

Jonkman, J. M., Butterfield, S., Musial, W., and Scott, G. 2009. Definition of a 5-Mw Reference Wind Turbine for Offshore System Development. National Renewable Energy Laboratory, Golden, CO, USA.

Jonkman, J. M., and Musial, W. 2010. Offshore Code Comparison Collaboration (OC3) for Iea Task 23 Offshore Wind Technology and Deployment. National Renewable Energy Laboratory, Golden, CO, USA.

Kallesøe, B. S., and Hansen, A. M. 2011. "Dynamic Mooring Line Modeling in Hydro-Aero-Elasticwind Turbine Simulations." The 21st International Offshore and Polar Engineering Conference, Maui, Hawaii, USA.

Koo, B. J., Goupee, A. J., Kimball, R. W., and Lambrakos, K. F. 2012. "Model Tests for a Floating Wind Turbine on Three Different Floaters." ASME 2012 31st International Conference on Ocean, Offshore and Arctic Engineering, Rio de Janeiro, Brazil.

Lindahl, J., and Sjoberg, A. 1983. "Dynamic Analysis of Mooring Cables." The Second International Symposium on Ocean Engineering and Ship and Handling, Gothenburg, Sweden.

Ma, W., and Webster, W. 1994. *An Analytical Approach to Cable Dynamics: Theory and User Manual. Sea Grant Project R/Oe-26.* Department of Naval Architecture and Offshore Engineering, University of California at Berkeley, CA, USA.

Martin, H. R., Kimball, R. W., Viselli, A. M., and Goupee, A. J. 2012. "Methodology for Wind/Wave Basin Testing of Floating Offshore Wind Turbines." ASME 2012 31st International Conference on Ocean, Offshore and Arctic Engineering, Rio de Janeiro, Brazil.

Min, H., Peng, C., Duan, F., Hu, Z., and Zhang, J. 2016. "Numerical Simulation of Dynamics of a Spar Type Floating Wind Turbine and Comparison with Laboratory

Measurements." ASME 2016 35rd International Conference on Ocean, Offshore and Arctic Engineering, Busan, Korea.

Min, H., and Zhang, J. 2017. "Numerical Simulation of a Floating Offshore Wind Turbine Constrained by Delta Mooring System." The 27th International Ocean and Polar Engineering Conference, San Francisco, CA, USA.

Moriarty, P. J., and Hansen, A. C. 2005. Aerodyn Theory Manual. National Renewable Energy Laboratory, Golden, CO, USA.

Musial, W., and Ram, B. 2010. Large-Scale Offshore Wind Power in the United States: Assessment of Opportunities and Barriers. National Renewable Energy Laboratory, Golden, CO, USA.

Nielsen, F. G., Hanson, T. D., and Skaare, B. r. 2006. "Integrated Dynamic Analysis of Floating Offshore Wind Turbines." ASME 2006 25th International Conference on Ocean, Offshore and Arctic Engineering, Hamburg, Germany.

Paulling, J., and Webster, W. C. 1986. "A Consistent, Large-Amplitude Analysis of the Coupled Response of a Tlp and Tendon System." Proceedings Fifth International Mechanics and Arctic Engineering Symposium, Tokyo, Japan.

Peng, C. 2015. "Numerical Study on a Spar Type Floating Offshore Wind Turbine Using Couple-Fast Code." Doctor of Philosophy Thesis, Ocean Engineering Program, Civil Engineering Department, Texas A&M University.

Peng, C., Yan, F., and Zhang, J. 2014. "Coupled Dynamic Response of a Spar Type Floating Offshore Wind Turbine." ASME 2014 33rd International Conference on Ocean, Offshore and Arctic Engineering, San Francisco, California, USA.

Quallen, S., Xing, T., Carrica, P., Li, Y., and Xu, J. 2013. "Cfd Simulation of a Floating Offshore Wind Turbine System Using a Quasi-Static Crowfoot Mooring-Line Model." The 23rd International Offshore and Polar Engineering Conference, Anchorage, Alaska, USA.

Sarpkaya, T., and Isaacson, M. 1981. *Mechanics of Wave Forces on Offshore Structures*: Van Nostrand Reinhold Company, NY, USA.

U.S.DOE. 2008. 20% Wind Energy by 2030: Increasing Wind Energy's Contribution to U.S. Electricity Supply. Execute Summary. Springfield, VA, USA.

U.S.DOE. 2017a. 2016 Offshore Wind Technologies Market Report. Alexandria, VA, USA.

U.S.DOE. 2017b. 2016 Wind Technologies Market Report. Alexandria, VA, USA.

Utsunomiya, T., Sato, I., Kobayashi, O., Shiraishi, T., and Harada, T. 2015. "Design and Installation of a Hybrid-Spar Floating Wind Turbine Platform." ASME 2015 34th International Conference on Ocean, Offshore and Arctic Engineering, St. John's, Newfoundland, Canada.

Wendt, F. F., Andersen, M. T., Robertson, A. N., and Jonkman, J. M. 2016. "Verification and Validation of the New Dynamic Mooring Modules Available in Fast V8." The 26th International Ocean and Polar Engineering Conference, Rhodes, Greece.

Zhang, J., Chen, L., Ye, M., and Randall, R. E. 1996. "Hybrid Wave Model for Unidirectional Irregular Waves—Part I. Theory and Numerical Scheme." *Applied Ocean Research* 18 (2–3):77-92.

APPENDIX A

SIMULATION RESULTS

1. LC01 (6.55 m/s Wind Only; Operational Condition 1)

1.1 Platform motions

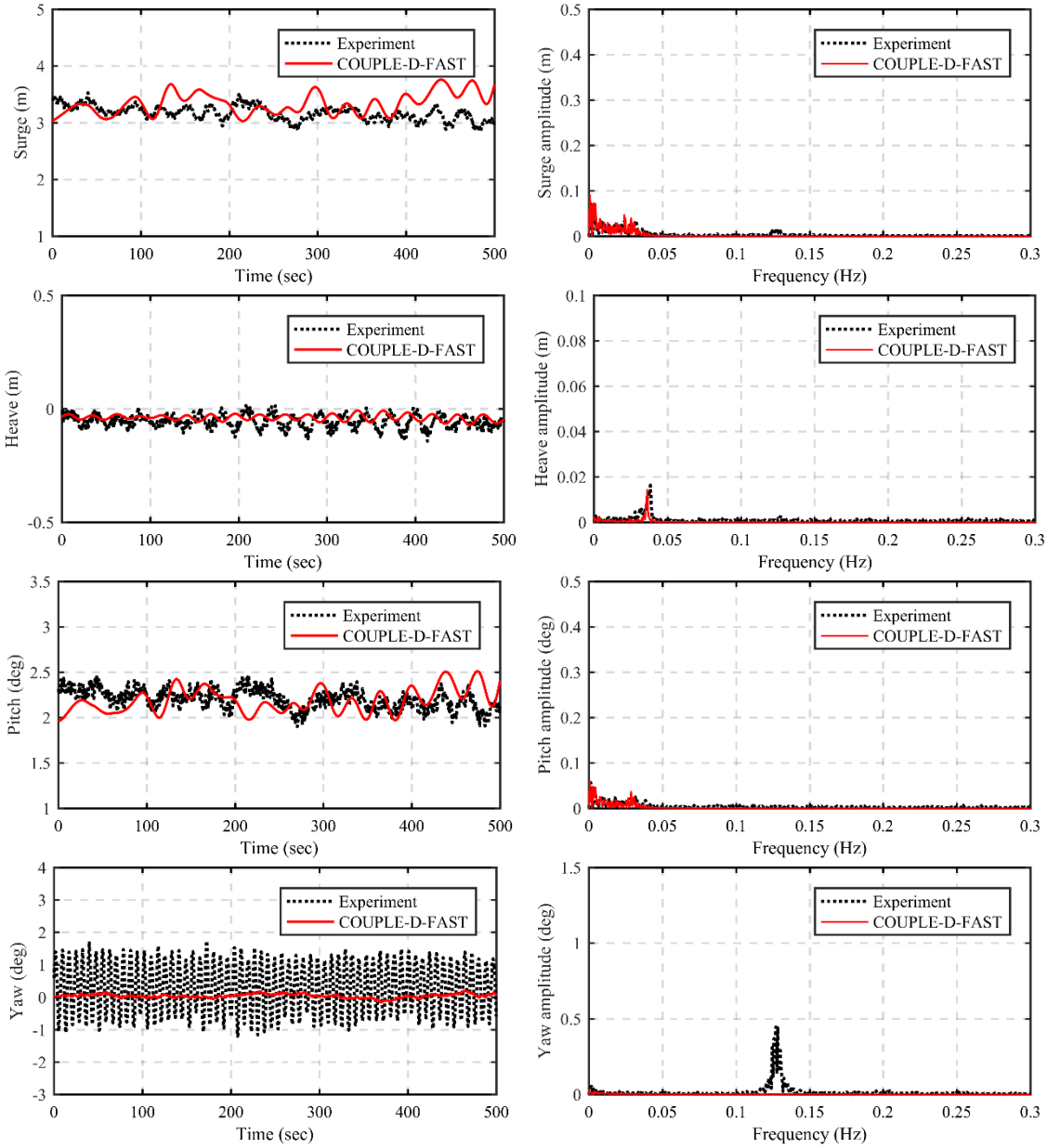

1.2 Mooring tensions

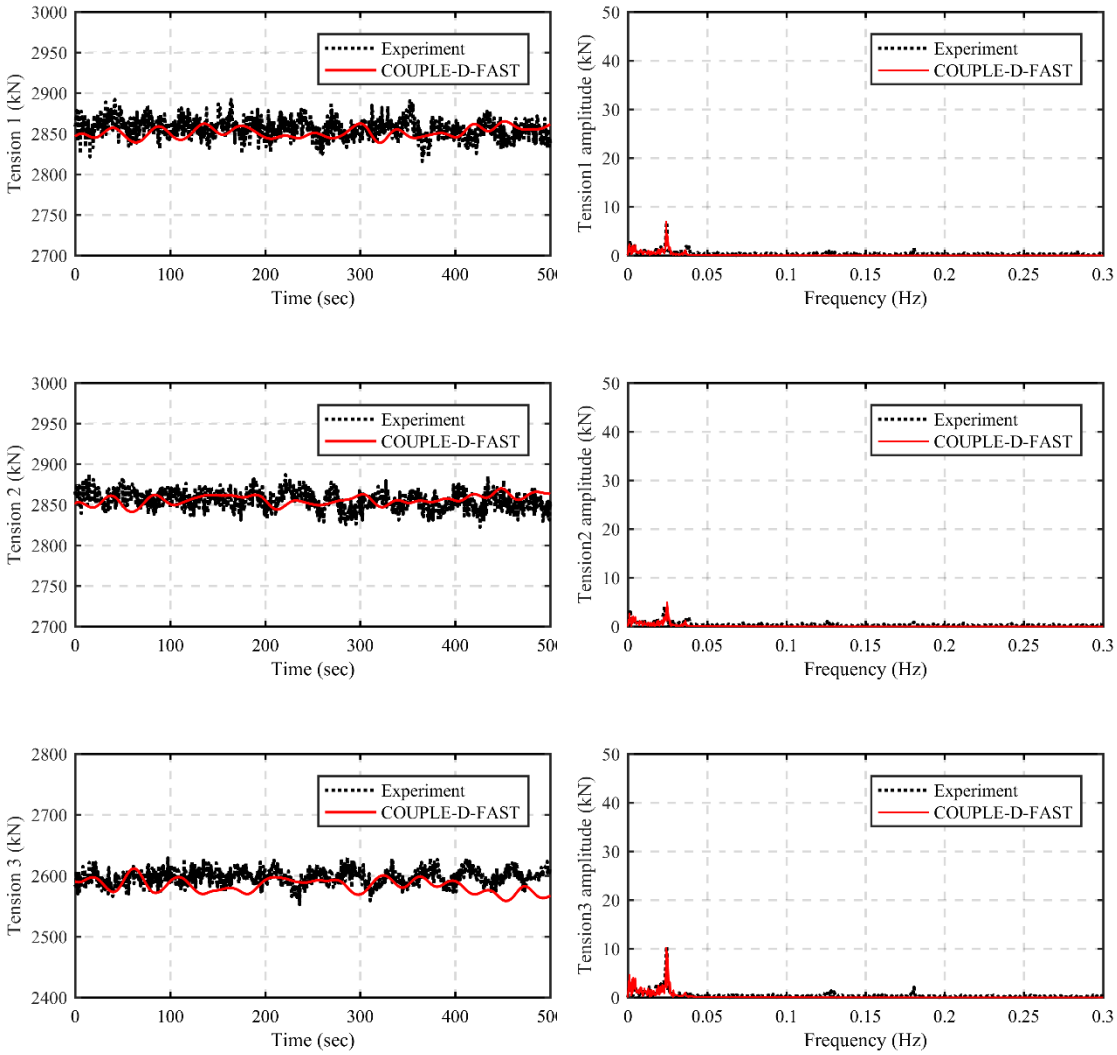

2. LC02 (8.62 m/s Wind Only; Operational Condition 2)

2.1 Platform motions

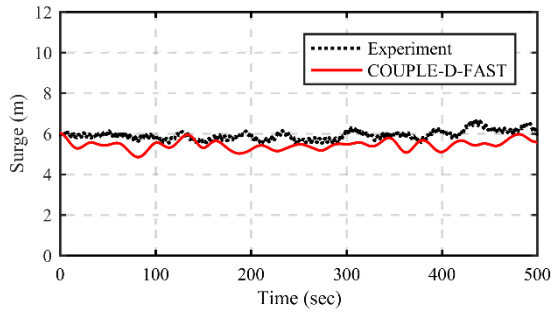

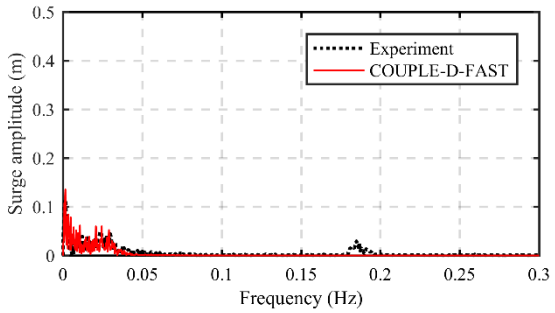

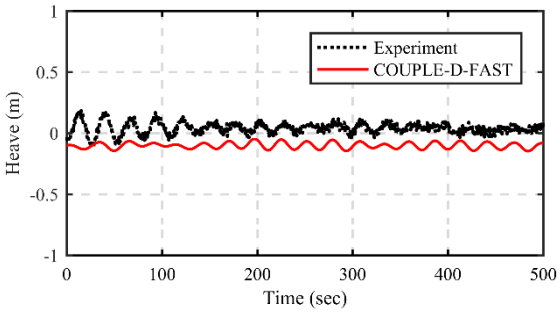

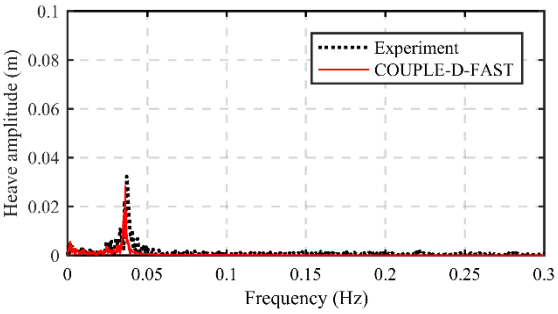

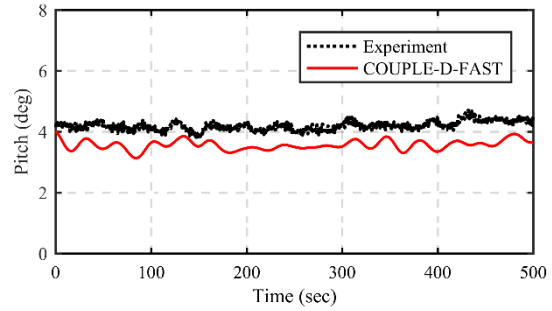

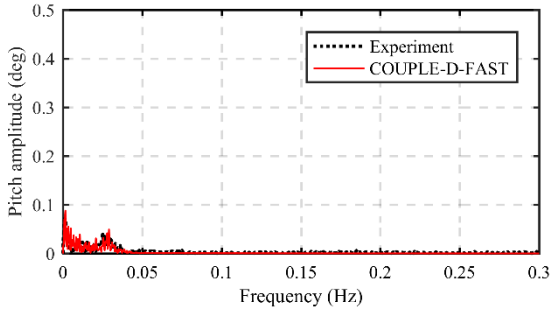

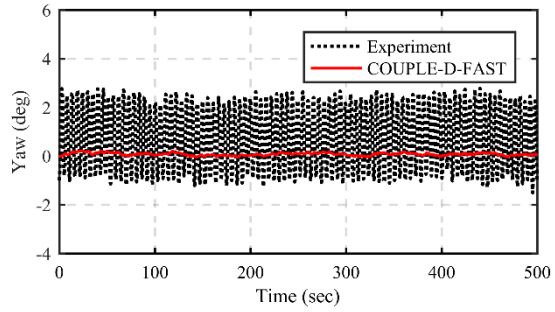

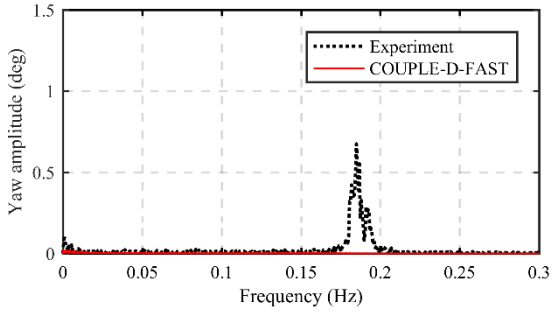

2.2 Mooring tensions

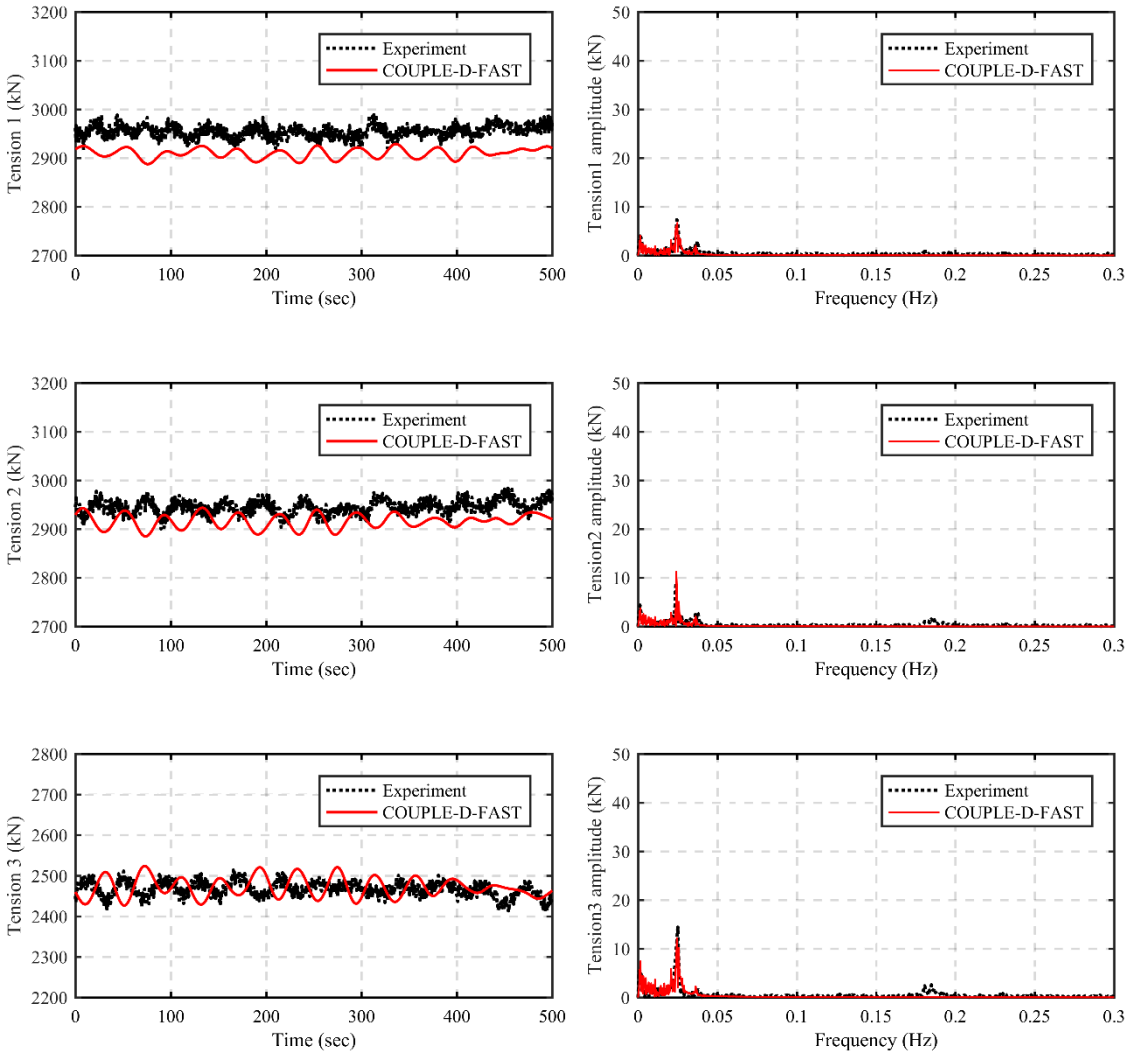

3. LC03 (11.41 m/s Wind Only; Extreme Condition)

3.1 Platform motions

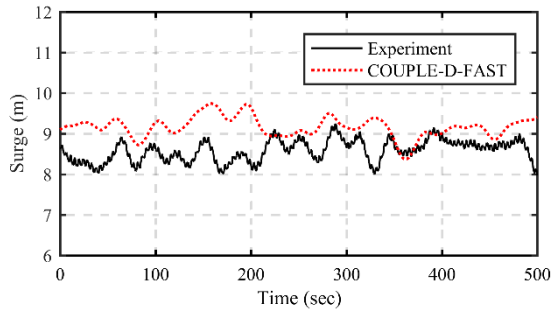

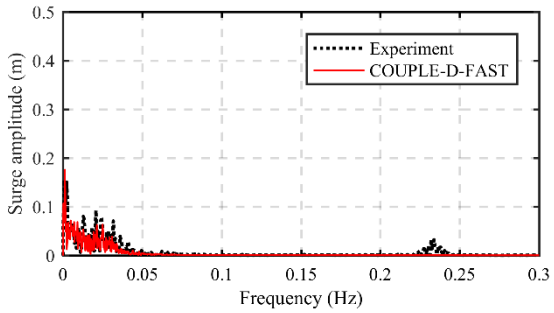

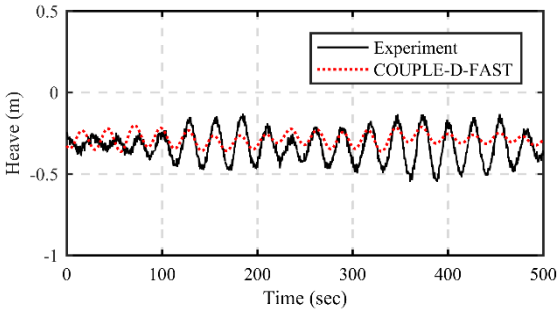

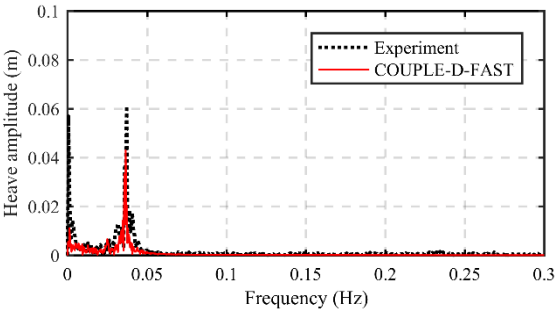

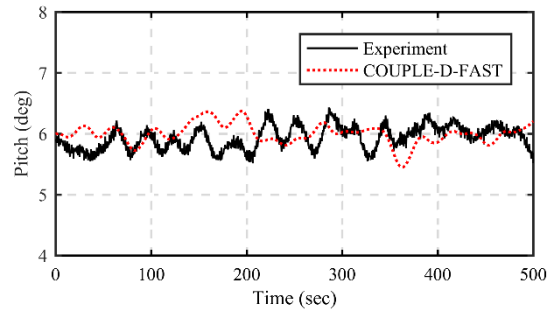

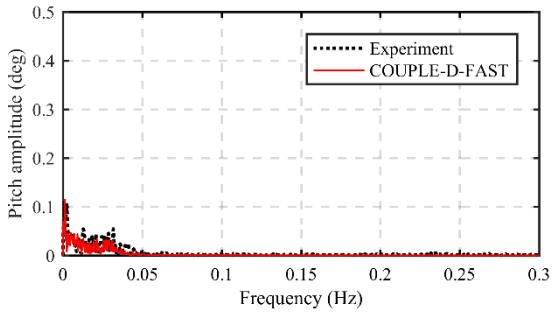

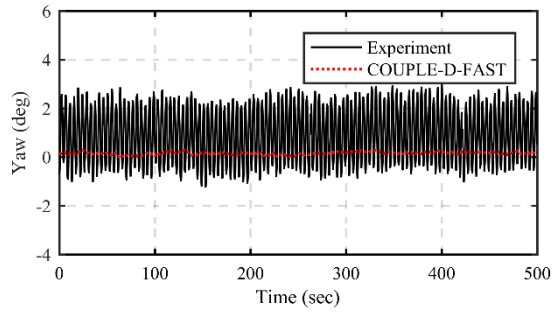

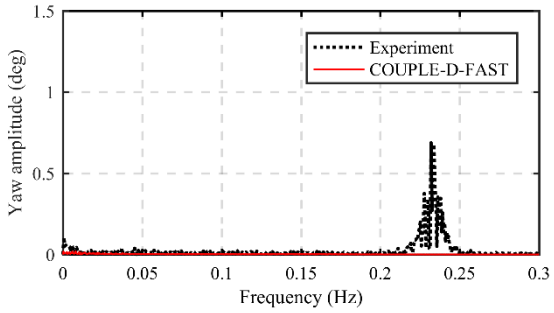

3.2 Mooring tensions

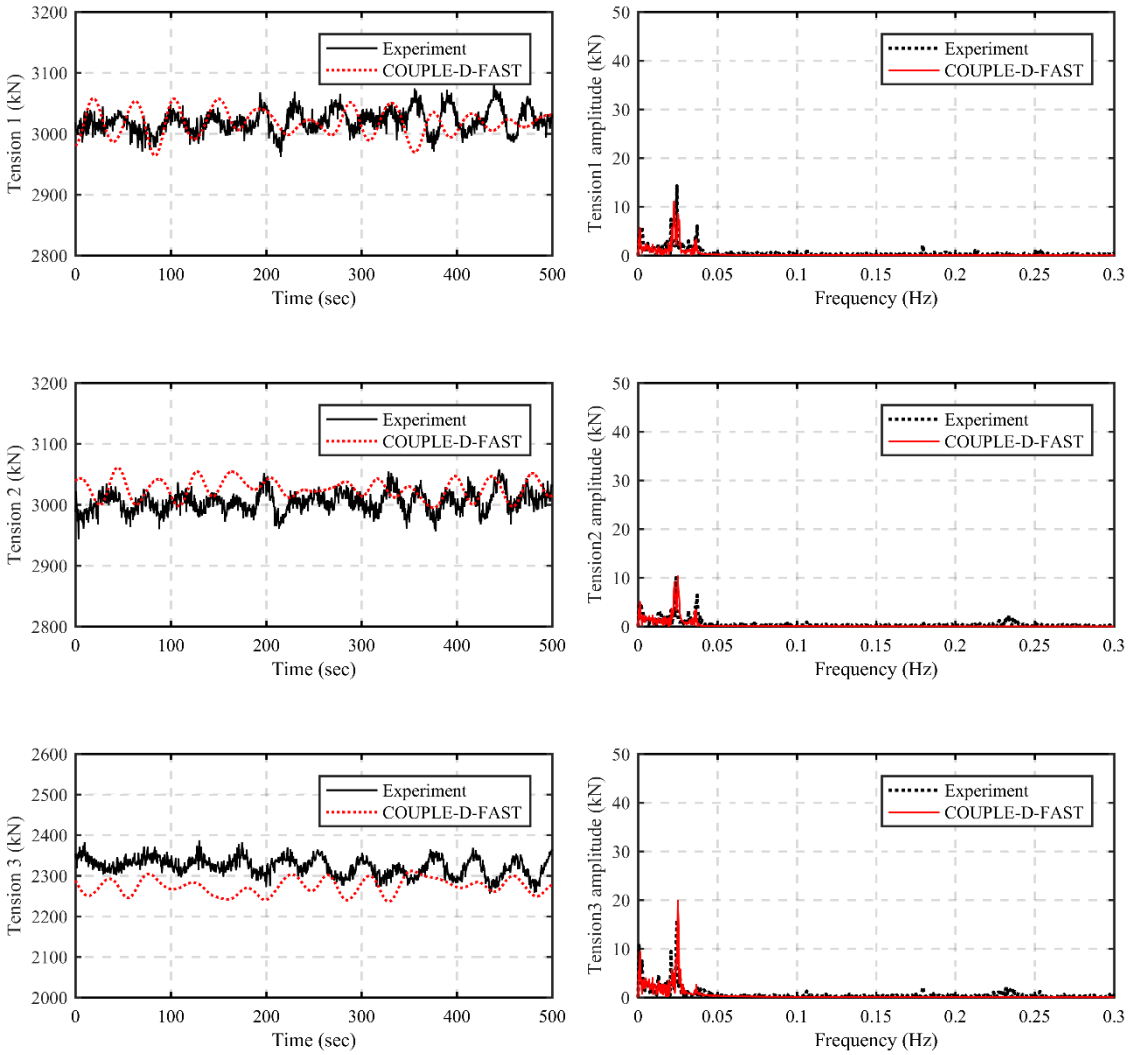

4. LC06 (6.55 m/s Wind + H = 2 m / T = 8 sec Regular Waves; Operational Condition 1)

4.1 Platform motions

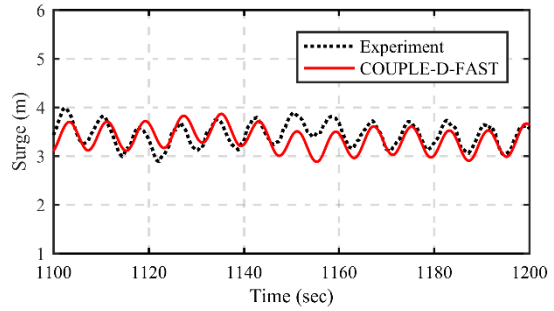

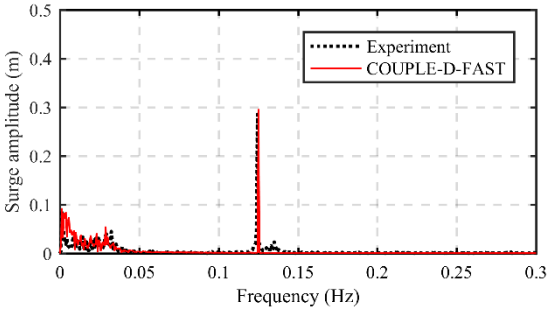

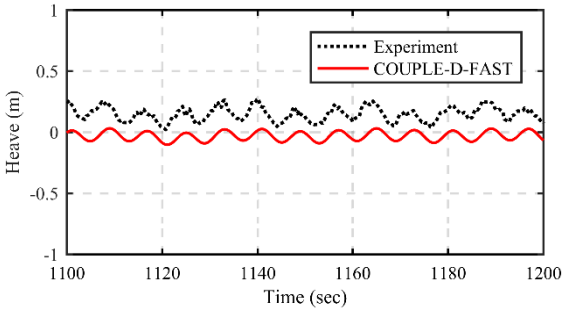

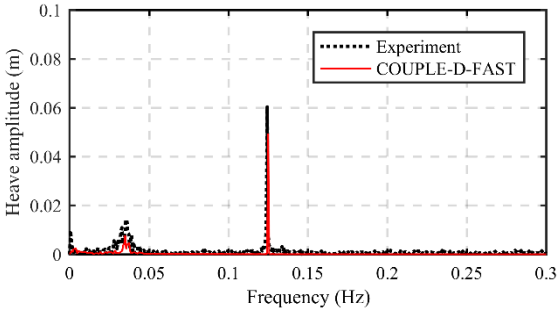

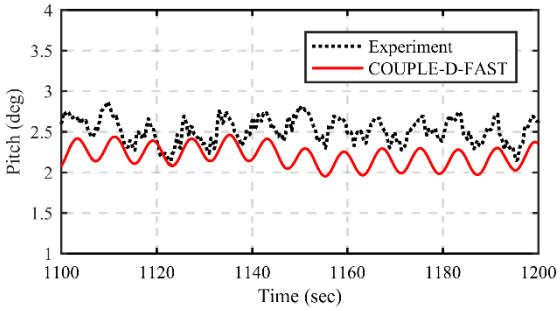

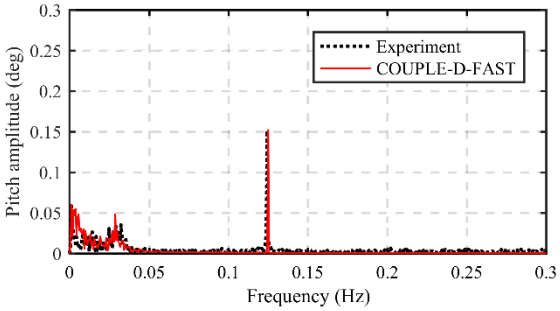

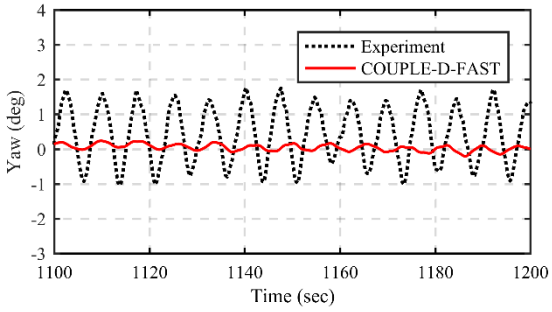

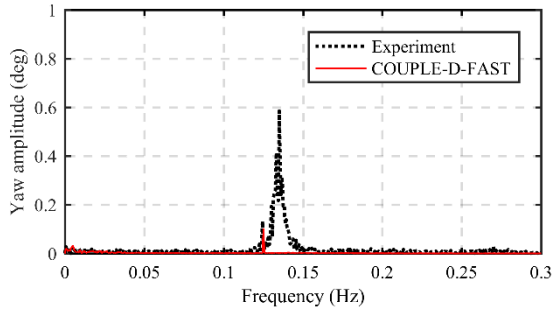

4.2 Mooring tensions

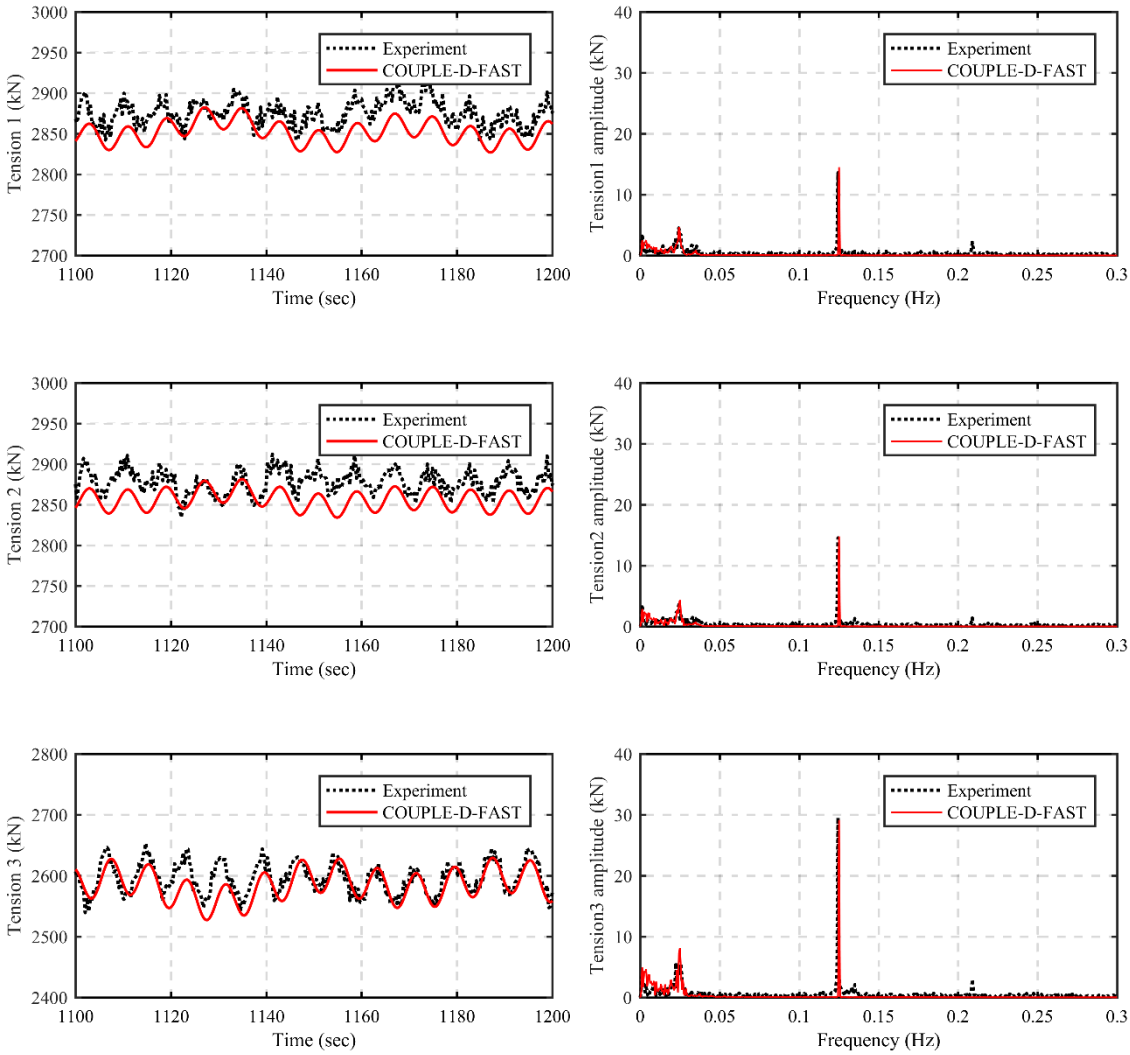

5. LC07 (8.62 m/s Wind + H = 6 m / T = 11 sec Regular Waves; Operational Condition 2)

5.1 Platform motions

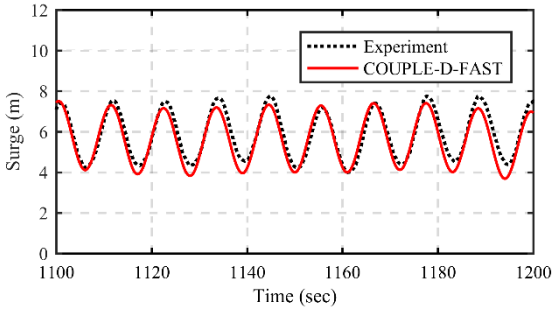

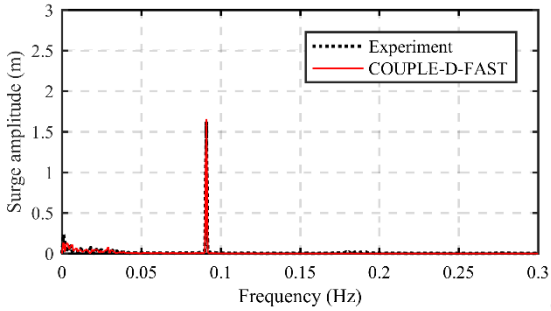

3

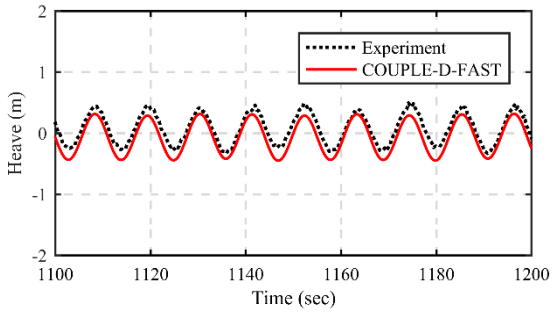

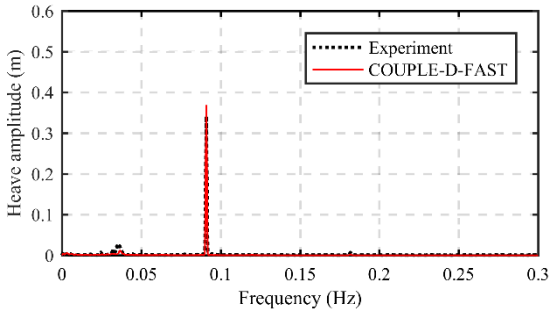

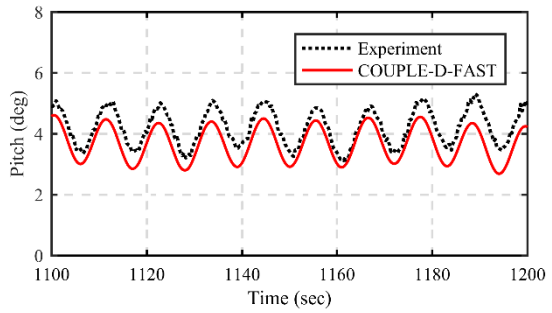

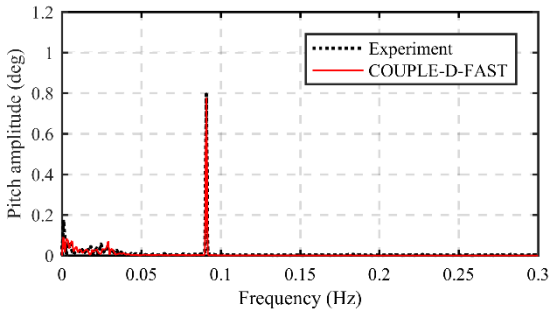

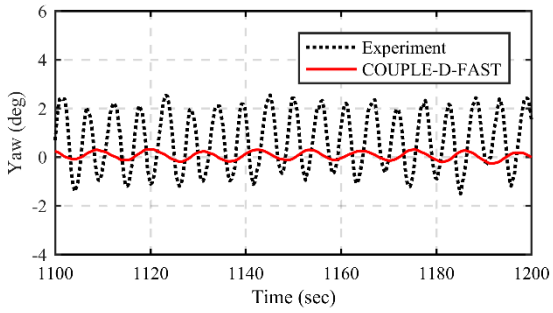

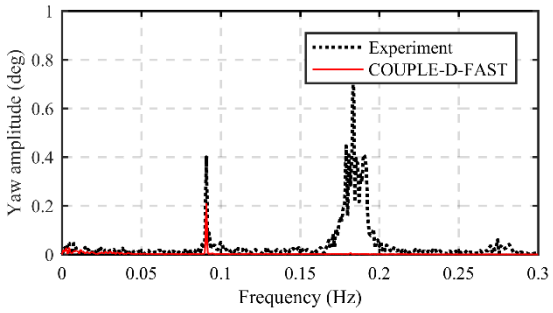

5.2 Mooring tensions

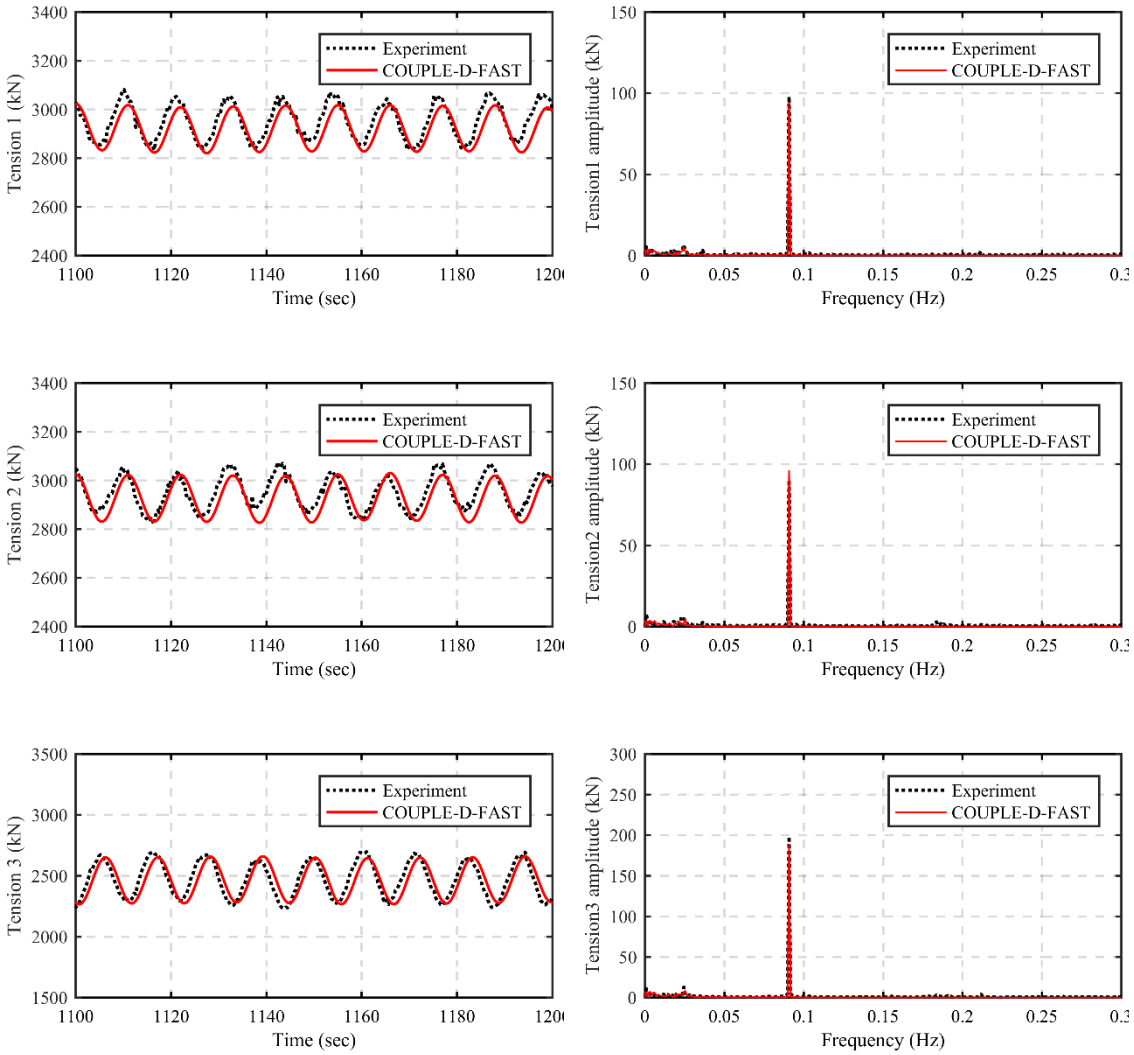

6. LC09

(6.55 m/s Wind + Hs = 2 m / Tp = 8 sec Irregular Waves; Operational Condition 1)

6.1 Platform motions

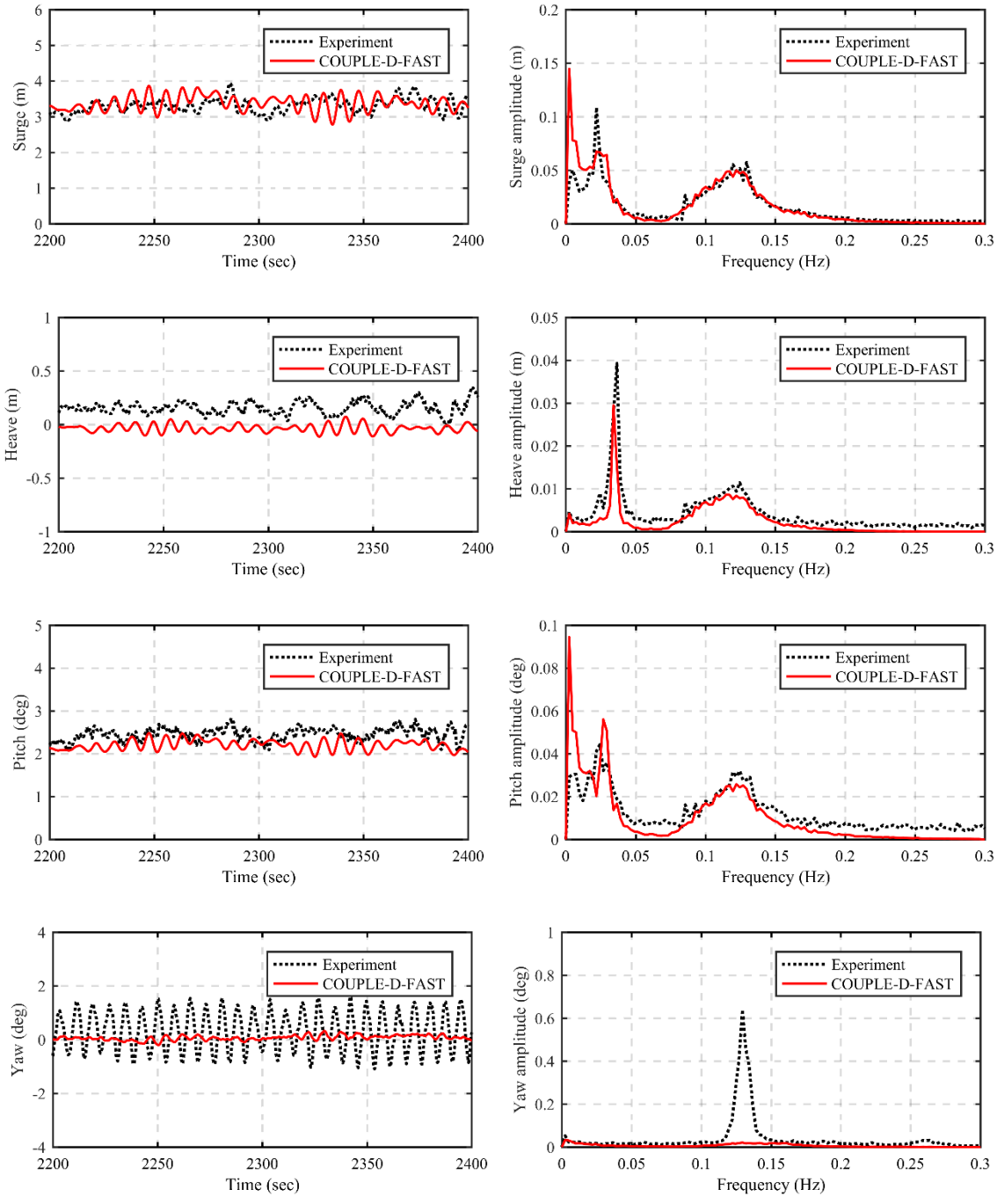

6.2 Mooring tensions

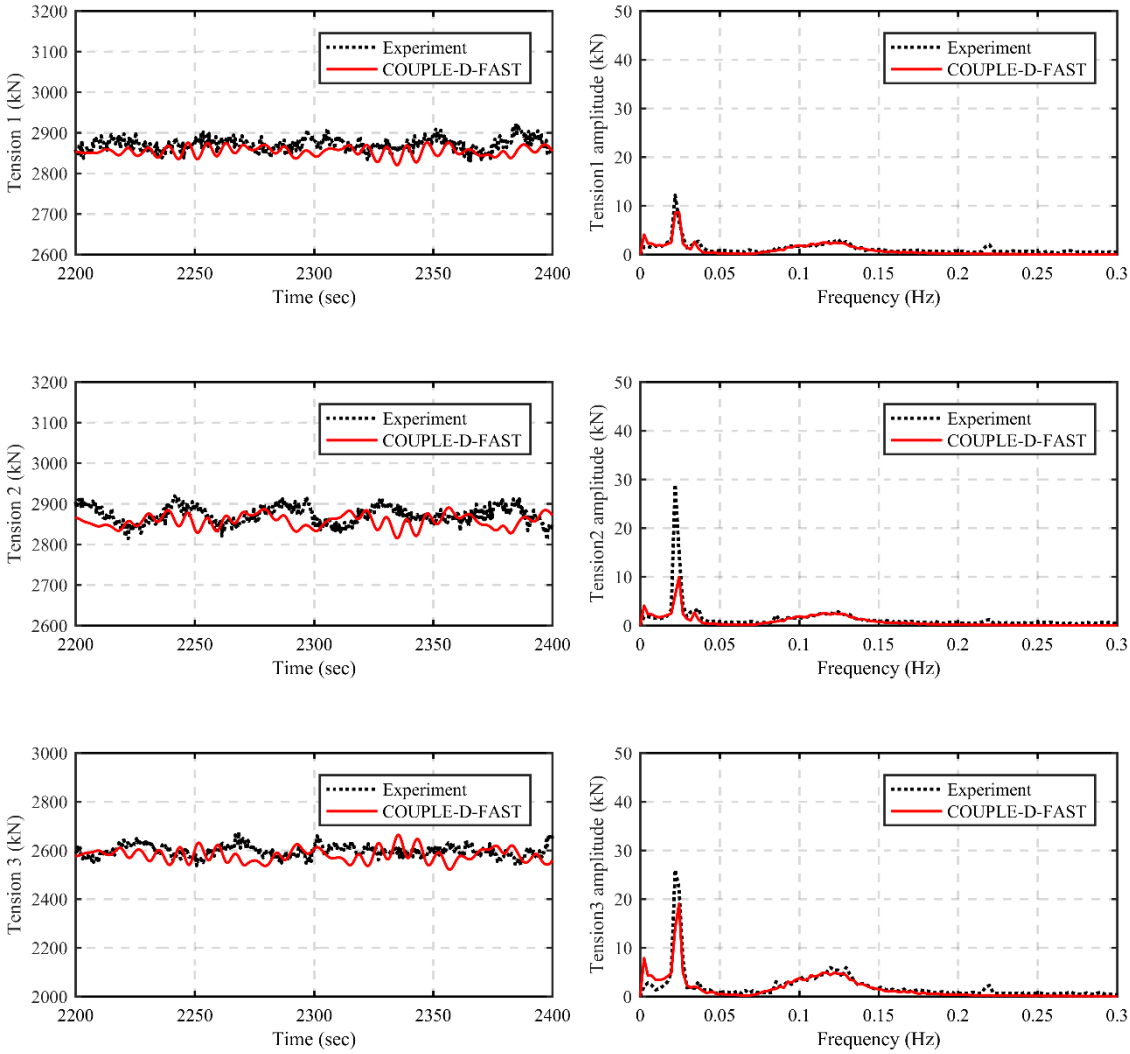

7. LC10

(8.62 m/s Wind+ Hs = 7.1 m / Tp = 12.1 sec Irregular Waves; Operational Condition 2)

7.1 Platform motions

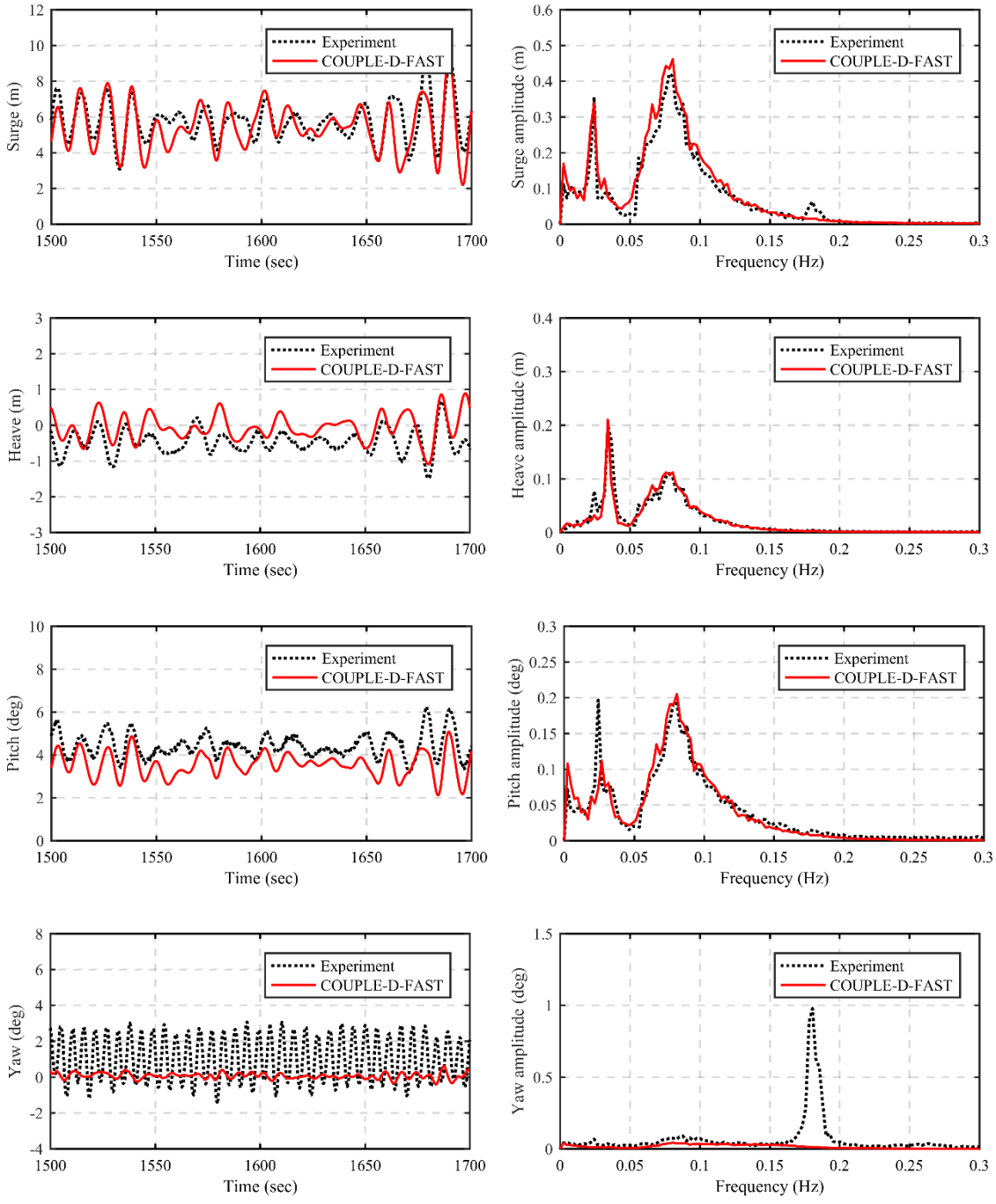

7.2 Mooring tensions